IntechOpen

Nuclear Material Performance

Edited by Rehab O. Abdel Rahman
and Hosam El-Din Mostafa Saleh

NUCLEAR MATERIAL PERFORMANCE

Edited by **Rehab O. Abdel Rahman**
and **Hosam El-Din Mostafa Saleh**

Nuclear Material Performance
http://dx.doi.org/10.5772/61411
Edited by Rehab O. Abdel Rahman and Hosam El-Din Mostafa Saleh

Contributors

Owais Ahmed Waseem, Ho Jin Ryu, Daniela Gurau, Enrique E. Pasqualini, Charles Solbrig, Shaon Ray Chaudhuri, Hongbo Du, Ziaul Huque, Fiifi Asah-Opoku, Raghava R Kommalapati, Rehab O. Abdel Rahman

© The Editor(s) and the Author(s) 2016
The moral rights of the and the author(s) have been asserted.
All rights to the book as a whole are reserved by INTECH. The book as a whole (compilation) cannot be reproduced, distributed or used for commercial or non-commercial purposes without INTECH's written permission.
Enquiries concerning the use of the book should be directed to INTECH rights and permissions department (permissions@intechopen.com).
Violations are liable to prosecution under the governing Copyright Law.

Individual chapters of this publication are distributed under the terms of the Creative Commons Attribution 3.0 Unported License which permits commercial use, distribution and reproduction of the individual chapters, provided the original author(s) and source publication are appropriately acknowledged. If so indicated, certain images may not be included under the Creative Commons license. In such cases users will need to obtain permission from the license holder to reproduce the material. More details and guidelines concerning content reuse and adaptation can be foundat http://www.intechopen.com/copyright-policy.html.

Notice

Statements and opinions expressed in the chapters are these of the individual contributors and not necessarily those of the editors or publisher. No responsibility is accepted for the accuracy of information contained in the published chapters. The publisher assumes no responsibility for any damage or injury to persons or property arising out of the use of any materials, instructions, methods or ideas contained in the book.

First published in Croatia, 2016 by INTECH d.o.o.
eBook (PDF) Published by IN TECH d.o.o.
Place and year of publication of eBook (PDF): Rijeka, 2019.
IntechOpen is the global imprint of IN TECH d.o.o.
Printed in Croatia

Legal deposit, Croatia: National and University Library in Zagreb

Additional hard and PDF copies can be obtained from orders@intechopen.com

Nuclear Material Performance
Edited by Rehab O. Abdel Rahman and Hosam El-Din Mostafa Saleh
p. cm.
Print ISBN 978-953-51-2447-4
Online ISBN 978-953-51-2448-1
eBook (PDF) ISBN 978-953-51-6658-0

Meet the editors

Rehab O. Abdel Rahman is Associate Professor of chemical nuclear engineering at Atomic Energy Authority of Egypt. She has been awarded Ph.D. degree in nuclear engineering. She has authored more than 30 peer-reviewed scientific papers, 5 book chapters, and 1 monograph. She is an honored scientist of the ASRT and serves as verified reviewer in several journals and managing editor for IJEWM and IJEE.

Hosam El-Din Mostafa Saleh is a Professor of radioactive waste management in the Radioisotope Department, Atomic Energy Authority, Egypt. He was awarded MSc and PhD degrees in physical chemistry from the Cairo University. He is interested in studying innovative economic and environment-friendly techniques for management of hazardous and radioactive wastes. He has authored many peer-reviewed scientific papers and monographs and he is book editor of different books related to valuable international publishers.

Contents

Preface

More than a century ago, the extensive study of natural nuclear materials led to development of our modern understanding of radiation properties and their effects on humans and the environment. This knowledge was further employed to serve the industrial civilization and improve modern life over several decades. Nowadays, nuclear science and technology are applied to produce energy, control diverse industrial processes, for medical diagnosis and treatment, and for environmental monitoring. This book aims at presenting research efforts used to identify nuclear materials performances in different areas. The authors cooperated to summarize their experience and present advances in different fields related to assessing the performance of these materials.

The book consists of seven chapters, organized in three sections that cover important research aspects in fission and fusion technologies and naturally occurring radioactive materials management. The introductory chapter aims to introduce technical efforts to improve nuclear fuel cycle operations, trends toward commercial fusion energy, challenges that face development in radioisotope production, and advances in management of naturally occurring radioactive materials. It identifies the impacts of current practices, determining anticipated trends toward better performances and mitigating challenges for commercial application of innovative technologies.

The second section presents developments in fission technology; it comprises five chapters that deal with biological remediation of mine effluents, nuclear fuel performance, and gamma ray spectrometer calibration. Biological remediation of uranium effluents containing sulfate using bioreactor is proposed by Prof. Chaudhuri et al. This chapter presents information on the optimization of inoculum and investigates the factors that can affect the bioreactor performance. Assessing materials performance in fission reactors is addressed in three chapters. The application of Monte Carlo N-Particle eXtended code to predict uranium burnup and fission product buildup for nine fuel elements types is presented by Prof. Kommalapati et al. The studied fuel elements are mixed oxide, uranium oxide, and commercially enriched uranium fuels clad with stainless steel, zirconium, and Zircaloy. A detailed study on the performance of Zircaloy clad under different operating conditions is presented by Dr. Solbrig et al. The chapter provides a comprehensive study on oxidation of Zircaloy 3 clad that is used in graphite-moderated thermal reactor, where empirical equations that predict oxidation and growth rates were deduced and validated. The feasibility of utilizing γ-Uranium–Molybdenum alloy to substitute highly enriched uranium fuel in research reactors is reviewed by Dr. Pasqualini. This chapter presents information on the fuel preparation using hydration, milling, dehydration process and then the manufacture of monolithic fuel with Zircaloy 4 clad and its performance after irradiation is described. The last chapter in this section is presented by Dr. Gurau, where Monte Carlo procedure is used to calibrate gamma spectrometry system and applied to measure radiation from large waste containers. Geant 3.21 was used to measure gamma rays released from 152Eu source and the detection efficiency was calculated.

Section 3 presents advances in fusion technology, where Drs. Waseem and Ryu present recent advances in understanding the performance of tungsten composite in fusion reactor environment. The preparation of different composites is reviewed and the performance of these materials in terms of their mechanical behavior, thermal properties, and oxidation resistance is presented

Rehab O. Abdel Rahman
Atomic Energy Authority of Egypt, Cairo, Egypt

Hosam El-Din Mostafa Saleh
Atomic Energy Authority of Egypt, Cairo, Egypt

Section 1

Introduction

Chapter 1

Introductory Chapter: Introduction to Current Trends in Nuclear material Research and Technology

Rehab O. Abdel Rahman

Additional information is available at the end of the chapter

http://dx.doi.org/10.5772/62856

1. Introduction

Peaceful applications of nuclear science and technology in medical, industrial, and agricultural fields have served human civilization over several decades. These applications lead to the spread uses of nuclear and radioactive materials in hospitals, clinics, factories, different research centers and universities, and other workplaces. Workers in nuclear fields recognized the importance of keeping their technologies reliable, clean, and improving its sustainability and safety. Major obstacles that face them are lack in some legalizations and technical expertise in some countries, shortage in international recourses, and the growing concerns about nuclear security and safeguards. To combat these obstacles, the International Atomic Energy Authority (IAEA) identified requirements to establish national infrastructure that can support nuclear energy program [1]. The following issues and their associated conditions could be used to judge the program.

1. National position, governmental support is a pivot element to develop a successful program and the maintenance of long-term political, social, and financial stability is a must.
2. Nuclear safety, stakeholders should be committed to achieve safety throughout the program lifecycle.
3. Management, highly competent management is key issue to attain safe and secure program.
4. Funding and financing, initial governmental funding and initial activities aim to develop human expertise to mange and regulate the facilities.
5. Legislative framework, national legal framework and international instruments, that is, conventions, agreements, and protocols signed by the country, should be integrated and implemented.

6. Safeguards, governmental commitment to nonproliferation obligations should be ensured.
7. Regulatory framework, effective independent competent national regulatory body can enhance public and international confidence in a specific program. Key aspect in this area is the development of competent human and physical resources.
8. Radiation protection, existing national infrastructure for nonnuclear energy program, that is, radiation, waste, and transport safety should be updated in compliance with international measures for nuclear energy program.
9. Electrical grid, nuclear energy is most efficient to run as base load generator and a general accepted principal that a single power plant should not exceed 10% of the total installed capacity.
10. Human resources development, development of educational and training capabilities especially in nuclear physics, nuclear material sciences for reactor operation, and fuel cycle among other specialties are needed to ensure crucial human resources sustainability.
11. Stakeholder involvement, reasonable involvement is a requisition of positive stable political and the proficiency of both regulatory body and operator is a key aspect in supporting public confidence.
12. Site and supporting facilities, stepwise selection process should be adopted that aims to identify safe, secure, and economically and socially accepted site.
13. Environmental protection, program impacts on the environment should be assessed with special consideration to regular discharge and adopted fuel cycle strategy.
14. Emergency planning, operating experiences indicated that emergency planning for operation and for workers and public outside the site boundary should be addressed as it complement facility safety and add to the defense in depth.
15. Security and physical protection, security should be supported by national legalization and multi-preventive security levels are needed and should be coordinated with nuclear safety requirements.
16. Nuclear fuel cycle (NFC), having clear nuclear fuel management strategy, is essential during the planning for a nuclear program; this should cover front- and backend fuel cycle. For front-end, international supplier can reduce the need to develop infrastructure in this field, whereas for back-end there should be national storage and the disposal development is governmental responsibility.
17. Radioactive waste, some countries that produce and use radioisotopes had developed low and intermediate level radioactive waste (LILW) predisposal and disposal infrastructure, which can support a nuclear energy program. But it should be noted that for spent fuel (SF) and high level waste (HLW), the only available technology is storage.
18. Industrial involvement, having nuclear energy program requires the enhancement of industrial capabilities, that is, supplying spare parts, consumable, instrument repair, and calibration services, according to the codes and standards under strict management system.

19. Procurement should be subjected to a strict management system.

It could be seen that these requirements are essential for any other nuclear activity and that the enhancement of waste and NFC capabilities has received considerable attention, as it is considered in six issues. In 2008, 3S concept was introduced for new users, but old users started also to consider these issues [2]. This concept aims to strengthen the relationship between safety, security, and safeguard to attain successful peaceful utilization of nuclear technology. Now, great efforts are directed to enhance safety, security, and safeguard aspects. This is achieved by identifying the impacts of current practices, determining anticipated trends toward better performances, and mitigating challenges for commercial application of innovative technologies. This chapter aims to introduce the technical efforts to improve NFC for fission technologies, trends in fusion research toward commercial utilization of its energy, challenges that face development in radioisotope production, and advances in the management of naturally occurring radioactive materials (NORMs) and technically enhance NORM (TENORM).

2. Nuclear fuel cycle technology for fission energy

Nuclear fuel cycle includes several integrated industries that produce and manage the fuel and its associated wastes before and after irradiation. As any industry, the development and operation of NFC facilities have different effects on the host society and the environment. The compensation between the added value of these facilities and its associated environmental impacts is an important challenge for the sustainability of these industries, epically with strengthen regulatory requirements that emerged recently [3, 4]. **Table 1** lists NFC processes, its associated wastes, and impacts [3, 5]. Research and development efforts in NFC could be divided into two classes: the first is directed to enhance current commercial technology's performance, in terms of operational safety improvements and cost and environmental impact reductions. The second class is concerned with getting innovative technologies into industrial scale applications. Nuclear Energy Agency (NEA) developed reports that summarize current and anticipated trends in NFC development within 20 years [5, 6]. **Tables 2** and **3** list these trends for front- and back-end NFC processes, respectively [3, 5–15].

Process		**Generated wastes**	**Associated hazard in the facility**	**Impacts**
Front end NFC	Mining	Large Liquid effluent volumes, Large amounts of NORM/ TENORM solid residues.	Radioactivity, Chemical toxicity.	Extraction of raw material, Generation of mining and milling tailings.
	Milling	Low and intermediate level (L&ILW) in form of: Liquid effluent, sludge, insoluble and filter aid.	Radioactivity, Chemical toxicity, Flammability.	
	Conversion			
	Enrichment	L&ILW, calcium fluoride, calcium		Waste generation.

Process		Generated wastes	Associated hazard in the facility	Impacts
		hydroxide, contaminated water, gaseous wastes, i.e. UF_6, F_2 and HF, and depleted U_3O_8		
Back end NFC	Fabrication	The amount and types of waste is dependent on the reactor type and if open or close nuclear fuel cycle is applied, but generally L&ILW, and High Level Waste (HLW)	Criticality, Radioactivity, Chemical toxicity, Flammability.	
	Irradiation and storage			Operational & accidental release, Waste generation.
	Fuel reprocessing and/or disposal			Operational releases and unanticipated radionuclide migration.

Table 1. Nuclear fuel cycle and their associated nuclear waste [3, 8–11, 13].

Process	Commercial technologies	Anticipated trends	Strengthen requirement
Mining	Localized deposits are used via • Open pit, • Underground mining, • In situ leaching (ISL), • Phosphate by-product recovery, • Heap leaching.	To ensure the sustainability • New deposits will be used, that is, high-grade unconformity-deposits, multi-mineral deposits and sandstone type, • Re-enrichment of depleted uranium, • Using closed NFC and former weapon-grade materials, • Increase application of ISL and underground mining.	Increased concern to develop environmental impact assessment and environmental restoration plan.
Conversion	• Ammonium Diuranate, • Ammonium Uranyl Carbonate.	Re-conversion of depleted uranium hexafluoride to U_3O_8.	Increased measure due to the application of 3S concept.
Enrichment	• Gaseous diffusion process, • Gas centrifuge process.	Improvements in centrifuge technology.	
Fabrication	Oxide fuel by pellet pressing and vibro-packing.	Clad and fuel material improvements.	Increased concern with reactor safety and application of 3S concept.
Irradiation	Different reactor types are commercially available, that is, LWR, PHWR, AGR, FR.	• Improve fuel/moderator distribution, • Reduce parasitic absorption and	

Process	Commercial technologies	Anticipated trends	Strengthen requirement
		radial and axial neutron leakage, • Improve core reload design, • Change reactor reload patterns.	

Table 2. Current and anticipated trends in front-end NFC [2, 3, 5–7].

Process	Objective	Commercial technologies	Anticipated trends
Storage	Provide safe and secure custody for the waste Protect operators and public from the radiological hazards of the waste.	Power plant pools, wet and dry storage.	
Reprocessing	Extraction of isotope from SF.	Purex	Development in Pyro-processing
Transmutation	Converting long-lived radionuclides into stable- or shorter-lived nuclides.	NA	R&D to reach industrial-scale applications,
Waste treatment	Volume reduction, Radionuclide removal, Changing waste composition.	Different technologies are available to treat aqueous, organic, and solid wastes.	Investigating new materials, and innovative techniques, that is, utilization of composite materials, nano-sized magnetic material.
Waste conditioning	Immobilize radio-contaminant in suitable matrix, Waste emplacement in suitable package.	L&ILW Immobilization in cement-based, polymer, and glass, HLW immobilization in glass, Cement-based or stainless steel containers.	Development of SF container, Improving host matrix performance and application, that is, improving glass-melting technology, improving cementitious material performance.
Waste disposal	Isolate conditioned waste under controlled conditions.	Different facilities of variable designs are available for I&LLW.	Improvement in design of disposal facilities, Licensing SF& HLW disposal.
Decommissioning	Facility or material is removed partially or totally from regulatory control.	Different chemical and mechanical technologies.	R&D to reduce amounts of secondary waste.

Table 3. Current and anticipated trends in backend NFC [3, 8–15].

3. Fusion technology

Fusion technology is expected to be an environmental favorable energy source that affects future energy market [16, 17]. This technology faced different challenges, that is, understand plasma physics, find suitable materials that can perform efficiently in plasma environment, and find technology that can efficiently and environmentally friendly produce electricity. In 2012, the European Fusion Development Agreement (EFDA) published a road map toward fusion energy. This publication identified the challenges, missions to tackle these challenges, and anticipated milestones till 2050 [18]. **Table 4** summarizes these issues and the anticipated actions till 2020.

Challenges	Objective	Missions	Anticipated milestones
Plasma regime operation	Minimize energy losses due to small-scale turbulence, Restrain plasma instabilities, Integrated performance with the divertor.	Maintain inductive and steady-state regime, Study compatibility at maximum power between high radiation and confinement.	Use JET to explore operational regimes Demonstrate JT60SA reliability, Define preliminary confinement scaling law in medium-sized tokamak.
Heat Exhaust	Establish exhaust system and plasma-facing materials that withstand large heat loads.	Demonstrate the control of detached conditions, Optimize radiated power, Study core contamination in case of impurity injection.	Test snowflake and super X configurations, Evaluate liquid metal targets in tokamaks.
Neutron-resistant materials	Identify baseline materials that maintain their structural and thermal performance under operational conditions.	Characterization, irradiation, and modeling the material's performance.	Use IFMIF and EVEDA to generate baseline material list, Identify risk reduction options, Demonstrate welding and joining processes performance.
Tritium self-sufficiency	Achieve efficient breeding and reliable extraction systems.	Demonstrate efficient and reliable H^3 extraction, Test the performance of blanket/first wall.	Determine the blanket, divertor, and coolant reliability, Evaluate alternate designs.
Intrinsic safety	Demonstrate inherent safety. Reduce waste management activity and define end point for the management strategy.	Safety rely on defense in depth and passive safety concepts with emphasis on vacuum vessel integrity, existence of expansion volumes, Efficient detritiation techniques and selection of disposal routes.	Safety of waste management and waste recycling.

Challenges	Objective	Missions	Anticipated milestones
Integrated DEMO design	Integrate all fusion technology into DEMO design.	Develop a magnet to reduce performance degradation in cyclic operation, Increase electron cyclotron frequency.	Capitalize ITER experience, Modest targeted investments in DEMO design, Cost minimization analysis.
Competitive electricity cost		Life cycle cost analysis, Extend the operational times, increase the power conversion cycle efficiency, Decrease re-circulating power.	
Bringing stellarator to maturity	Develop stellarator.	Validate energy and particle confinement of optimized divertor.	Investigate the performance of plasma confinement and cooling components.

Table 4. Milestones toward fusion technology application till 2020 [18].

4. Radioisotope production

There are more than 160 different radioisotopes that are used regularly in different fields; these isotopes are produced either in a medium- or in a high-flux research reactors or particle accelerators (low or medium energy) [19, 20]. In 2014, IAEA published the results of a meeting on current status and future trends on radioisotope application in industry. The meetings produced a prioritized list that identifies area of interests in this field, which includes the application of small-sized neutron generators, development and application of nano-tracers, radiotracer application in mineral industry, tracer technology for sediment transport, development of radiotracer generators, tomography, hybrid instrumentation, process modeling, application in petroleum industry, high-resolution detectors, and process industry [21].

The sustainability of radioisotope production is one of the critical areas that receive great attention. ^{99}Mo is the greatest produced isotope that decays to ^{99m}Tc, which is used in 85% of the nuclear medicine diagnostic imaging procedure worldwide [22, 23]. Currently, the world production relies on using highly enriched uranium targets (HEU). IAEA activity in this field focuses on the conversion of this technology to using low enriched uranium (LEU) targets [23]. **Table 5** summarizes available and innovative technologies in the production of ^{99}Mo.

Current methods	Application	Feature	Challenges
Nuclear reactors			
Heterogeneous reactor using HEU target	Belgium, Canada, Netherlands.	Produce 93% of the world production.	Nonproliferation concerns, Consume ≅50 kg HEU, Low production yield [20].

Current methods	Application	Feature	Challenges
Heterogeneous LEU targets	South Africa, Argentina, South Korea, and Australia [24].	No nonproliferation threat.	Improvements in target materials, Improvement in separation technology [26].
Heterogeneous reactor –Neutron activation	USA, India, Japan, Kazakhstan, Peru, Russia, and Uzbekistan.	Use natural uranium.	Less productive, Low specific activity.
Homogeneous reactor LEU target	USA and Russia.	High production yield, Flexible process optimization, Reduce waste generation, Efficiently produce isotopes, Better economics [25].	Low separation efficiency [23].
Accelerator production			
Proton based	Tested experimentally, (Molybdenum target).	Direct production of ^{99m}Tc, Yield depends on the cyclotron energy, Very low radioactive waste [26,27],	Attainment of high energy, and intensity, Optimize targets to maximize secondary neutron production and thermalization [26].
Electron	Tested experimentally, (Molybdenum target).	Theoretical High yield,	High energy electron with high power, Pure Mo target [27].
	Tested experimentally, (Uranium target).	Yield similar to reactor yield, No ficile material used.	Waste arising similar to that of LEU reactor route, High-energy electron with high-power attainment [27].

Table 5. Conventional and innovative technologies for ^{99}Mo production [20–27].

5. NORM/TENORM management

NORM and TENORM residue generation accompanies industrial activities to exploit natural resources, namely mining, physical, wet chemical, and thermal processes that aim to separate, extract, and process these resources. The problems of managing these materials are related to their huge volume, very low specific radioactivity content, their presence in non-radiological industries, and the variability of their chemical, physical, and radiological properties that differ from industry to another and from site to site [4, 28]. Historical poor management practice led to different contamination problems that vary in their extent and properties. Dealing with these problems is affected by ethical, technical, and economical considerations [3, 4, 10, 29–30]. IAEA defined six radiological bands that could be used to support the decision-making process for remediation project [31]. Research and development in this area is directed to enhance the performance of remediation technologies and their economics [4, 10].

Finding a safe management route for NORM and TENORM motivated governments to announce their policy and strategy in this area [4]. In this context, these residues were divided into two categories: the first one is characterized by its moderate-activity concentration and huge volume, whereas the second contains higher-activity concentration and small volume. Recycling/reuse option has attracted attention on the international and national scale for the first category, where this option is considered after evaluating the chemical and radiological properties of the residues and updating the regulatory and legal framework. For the second category, disposal as waste is the only option [28]. Researches in this field is concerned with NORM/TENORM hazard characterization and evaluating their environmental impacts.

6. Conclusion

This chapter introduces advances in areas where nuclear material is produced and used. It aims to highlight the gaps that need further elaboration toward sustainable, safe, and reliable utilization of these materials. It could be concluded that

1. Researches and development efforts are needed in different areas to enhance current system safety and performance and to support the commercial application for innovative technologies.
2. 3S integration is a must, and international, regional, and national organizations started to implement this concept by issuing guidelines to adjust the legal framework, and support operation of non-HEU in radioisotope production.
3. Huge efforts are needed to address the challenges that face the application of anticipated trends on the governmental, operational, and regulatory levels and to coordinate these efforts.

Author details

Rehab O. Abdel Rahman

Address all correspondence to: alaarehab@yahoo.com

Hot Lab. Center, Atomic Energy Authority of Egypt, Cairo, Egypt

References

[1] IAEA, Milestones in the development of a national infrastructure for Nuclear power, IAEA- nuclear energy sires, Vienna. NG-G- 3.1, 2007.

[2] M. Suzuki, Y. Izumi, T. Kimoto, Y. Naoi, T. Inoue, B. Hoffheins, Investigating 3S synergies to support infrastructure development and risk-informed methodologies for 3S by design, IAEA, Vienna, 11-5 Nov 2010, IAEA-CN- 84/64.

[3] R. O. Abdel Rahman, R. Z. Rakhimov, N. R. Rakhimova, M. I. Ojovan, Cementitious materials for nuclear waste immobilisation, Wiley, West Sussex. 2014. ISBN 9781118512005.

[4] R. O. Abdel Rahman, M. Elmesawy, I. Ashour, Y.-T. Hung, Remediation of NORM and TENORM contaminated sites – review article, *Env. Prog. Sustain. Energ.*, 33(2) (2014), 588–596.

[5] NEA, Trends in the nuclear fuel cycle, economic, environmental and social aspects, NEA, Paris, 2001.

[6] NEA, Trends towards sustainability in the nuclear fuel cycle, NEA, Paris, 2011.

[7] Current Trends in Nuclear Fuel for Power Reactors, https://www.iaea.org/About/Policy/GC/GC51/GC51InfDocuments/English/gc51inf-3-att5_en.pdf, last accessed in April 2016.

[8] R. O. Abdel Rahman, Planning and implementation of radioactive waste management system, In, Radioactive waste, R.O. Abdel Rahman (ed), 2012, Intech, Croatia. 04/2012, ISBN: 978-953-51-0551-0. http://www.intechopen.com/books/radioactive-waste/planning-and-implementation-of-radioactive-waste-management-system

[9] R. O. Abdel Rahman, A.M. El Kamash, H. F. Ali, Y.-T. Hung, Overview on recent trends and developments in radioactive liquid waste treatment part 1: sorption/ion exchange technique, *Int. J. Environ. Eng. Sci.*, 2(1) (2011), 1–16.

[10] R.O. Abdel Rahman, M. W. Kozak, Y.-T. Hung, L.K.Wang, N.K. Shammas, Radioactive pollution and control, In Handbook of environment and waste management, World Scientific Publishing Co, Singapore, Feb 2014, 949–1027. http://dx.doi.org/10.1142/9789814449175_0016

[11] R. O. Abdel Rahman, H. A. Ibrahium, Y.-T. Hung, Liquid radioactive wastes treatment: areview, *Water*, 3 (2011), 551–565. http://www.mdpi.com/2073-4441/3/2/551/pdf

[12] IAEA, Radioactive waste management glossary, IAEA Vienna, 2003.

[13] R.O. Abdel Rahman, M. I. Ojovan, Leaching tests and modelling of cementitious wasteforms corrosion, *Innov. Corros. Mater. Sci.*, 4(2) (2014), 90–95.

[14] Z. Drace, I. Mele, M.I. Ojovan, R.O. Abdel Rahman, An overview of research activities on cementitious materials for radioactive waste management. *Mater. Res. Soc. Symp. Proc.* 1475(2012), 253–264.

[15] R. O. Abdel Rahman, Radioactive waste, 2012, Intech, Croatia. ISBN 978-953-51-0551-0. http://www.intechopen.com/books/radioactive-waste

[16] Department of energy and climate change, Nuclear energy research and development roadmap future pathway, 26 March 2013, Ref: BIS/13/632, https://www.gov.uk/government/uploads/system/uploads/attachment_data/file/168043/bis-13-632-nuclear-energy-research-and-development-roadmap-future-pathway.pdf, Last accessed in April 2016.

[17] Y. Asaoka, R. Hiwatari, K. Okano, Y. Ogawa, H. Ise, Y. Nomoto, T. Kuroda, S. Mori, K. Shinya, Conceptual design of a demonstration reactor for electric power generation, 20th IAEA Fusion Energy Conference, 1–6 November 2004, IAEA, Vilamoura, Portugal FT/P7-4.

[18] Fusion electricity EFDA, 2012, https://www.euro-fusion.org/wpcms/wp-content/uploads/2013/01/JG12.356-web.pdf, Last accessed in April 2016.

[19] IAEA, Radiopharmaceuticals: production and availability, ttps://www.iaea.org/About/Policy/GC/GC51/GC51InfDocuments/English/gc51inf-3-att2_en.pdf, last accessed in April 2016.

[20] Yu. Chuvilin, V. E. Khvostionov, D. V. Markovskij, V. A. Pavshouk,V. A. Zagryadsky, Low-waste and proliferation-free production of medical radioisotopes in solution and molten-salt reactors, In Radioactive waste, R.O. Abdel Rahman (ed), Intech, 2012.

[21] IAEA, the current status and future trends on radioisotope applications in industry, Report of the Consultants' Meeting 10–14 December 2012 on, IAEA 2014.

[22] NEA, Beneficial uses and production of isotopes, OECD, Paris. 2005.

[23] IAEA, Non-HEU production technology for Molebdenium-99 and Techncium-99m, IAEA nuclear energy series No, NF-T-5.4, IAEA, 2013.

[24] B.L. Zhuikov, Production of medical radionuclides in Russia: status and future—a review, *Appl.Radiat. Isot.*, 84(2014), 48–56.

[25] IAEA, Homogeneous aqueous solution nuclear reactors for the production of mo-99 and other short lived radioisotopes, IAEA, Vienna, 2008, IAEA-TECDOC-1601.

[26] IAEA, Production technologies for Molebdeium-99 and Technethium-99, IAEA, Vienna, 1999, IAEA-TECDOC-1065.

[27] Nea, The supply of medical isotopes, Review of Potential Molybdenum-99/Technetium-99m Production Technologies, OCED, Paris. 2010.

[28] IAEA, Management of NORM resources, IAE- TECDOC 1712, IAEA, Vienna. 2013.

[29] R. O. Abdel Rahman, O.A. Abdel Moamen, M. Hanafy, N. M. Abdel Monem, Preliminary investigation of zinc transport through zeolite-X barrier: linear isotherm assumption, *Chem. Eng. J.*, 185–186 (2012), 61–70.

[30] M. Ghaly, F. M. S. E. El-Dars, M. M. Hegazy, R. O. Abdel Rahman, Evaluation of synthetic Birnessite utilization as a sorbent for cobalt and strontium removal from aqueous solution, *Chem. Eng. J.*, 284(2016), 1373–1385.

[31] IAEA, Technologies for remediation of radioactively contaminated sites, IAEATEC-DOC- 1086, International Atomic Energy Agency, Vienna, 1999.

Section 2

Fission Technology

Chapter 2

Developing Tailor-Made Microbial Consortium for Effluent Remediation

Shaon Ray Chaudhuri, Indranil Mukherjee,
Debabrata Datta, Chaitali Chanda,
Ganesh Prasath Krishnan, Swati Bhatt,
Paulami Datta, Shashi Bhushan, Sourav Ghosh,
Pinaki Bhattacharya, Ashoke Ranjan Thakur,
Debanik Roy and Parthasarathi Barat

Additional information is available at the end of the chapter

http://dx.doi.org/10.5772/62594

Abstract

The work describes a biofilm-based soluble sulphate reduction system, which can treat up to 1600 ppm of soluble sulphate within 3.5 hours of incubation to discharge level under ambient condition using a well-characterized sulphate-reducing bacterial (SRB) consortium. This system ensures the treatment of 1509 litres of sulphate solution in 24 hours using a 220-litre bioreactor. Performance of the system during series operation was compromised, indicating the presence of inhibitor in solution at a toxic level. A single unit bioreactor would be the ideal configuration for this consortium. Modified designs of bioreactors were tested for optimization of the process using response surface methodology (RSM), where the system could function optimally at an initial sulphate concentration of 1250 ppm with a flow rate of 1.8 litre/hour. The time course of sulphate reduction yielded a parabolic profile (with coefficient of determination $r^2 = 0.99$ and p value < 0.05). The rate of sulphate reduction was found to be independent of seasonal variation as well as the specific design characteristic.

Keywords: Sulphate, packed bed reactor, time series analysis, bacterial consortium, Nitrate, radioactive effluent

1. Introduction

Extraction of nuclear materials like Uranium from ores generates effluents containing sulphate. Sulphate mostly comes from the sulphuric acid used for extraction of uranium from its ore. Sulphate is also released as a by-product of different anthropogenic activities such as metal smelting, fuel gas scrubbing, molasses fermentation, tanneries, food processing, coal burning, pulp and paper processing and mining activities [1, 2]. Increase in sulphate concentration in ground water causes various adverse effects such as laxative effect, dehydration, and skin problem, and it also imparts an unpleasant taste to water [3]. It is an eye irritant, causing redness upon exposure. It has also been reported that sulphate pollution results in eutrophication of both surface and ground water. It indirectly enhances phosphate-based eutrophication that can inhibit the growth of different plant species. Na_2SO_4 contamination in the soil can lead to change in freezing temperature by 0.28 °C [4, 5]. The standard level for the presence of sulphate is 250 ppm in drinking water while it is 1000 ppm for waste water. There are different techniques for sulphate demineralization such as reverse osmosis, distillation, ion exchange for drinking water, while methods involving chemical precipitation using chemicals like barium chloride exist for environmental waste disposal. The chemical method of reduction of sulphate using barium chloride also ensures substantial reduction of heavy metals in the form of precipitates. But for the chemical process to function optimally, it is essential that the concentration of the chemical is high and that it is thoroughly mixed with the effluent discharged. The mechanical stirring in case of large volumes may not be a feasible option at the industrial scale. Hence, physicochemical techniques have many drawbacks when their efficiency is compared with the cost of implementation of the technology [6].

Bioremediation happens to be an alternative method of treatment. Biological sulphate reduction is a state-of-the-art technology, which has definite advantages over conventional treatments. Sulphate-reducing bacteria (SRB) play an important role in several biochemical processes. Sulphate is taken up by these microbes as a nutrient and reduced to sulphide, which is then incorporated into sulphur-containing amino acids. Thus, they are significant in sulphur transformation [7]. SRB is heterogeneous, morphologically diverse, physiologically unique anaerobic microorganisms that are widespread in anoxic habitats [8, 9], where they use sulphate as a terminal electron acceptor for the degradation of organic compounds, resulting in the production of sulphide. Both oxidation and reduction reactions for the generation of metabolic energy are important. The sulphide thus produced can be oxidized in the presence of high levels of oxygen by chemolithotrophic sulphur bacteria or under anoxic conditions by phototrophic sulphur bacteria, whereas SRB perform the dissimilatory sulphate reduction [10–12]. In marine sediments, above 50% organic carbon mineralization is carried out by sulphate reduction making the sulphate reducers extremely important for both the sulphur and carbon cycles. However, the use of SRB for bioremediation of waste water has some bottle necks. These include (a) the continuous supply of microbes for sulphate reduction within reasonable time and (b) the survival of the microbes in the environment while maintaining the efficiency of reduction. The literature reported a retention time of 15 days [13], 14 days [14], 10 days [7], 6 days [15], and 1 day [16] while working at laboratory scale with associated problems of clogging, back pressure and need for repeated maintenance. These facts made them non-viable for large-scale applications. Hence, the need of the hour was to develop a microbial solution through which rapid removal of soluble sulphate could be carried out in a sustainable manner. To address this issue, the following points had to be considered: (1) appropriate site selection for enrichment of SRB; (2) appropriate medium selection for the same; and (3) consortium optimization and development of packed bed reactor with optimal design for sustained performance of the system.

As an outcome of this study, a consortium was developed using which a packed bed bioreactor–based process has been drawn up, which is by far the fastest and the most stable sulphate removal system. This invention has been filed as an Indian patent and a PCT [17] to protect the intellectual property associated with this invention. It has immense application for industrial effluent treatment. Although biofilm-based bioreactors have been the point of investigation and application for a long period of time [18–21], little progress has been made in terms of real-life industrial application.

2. Selection of inoculum and medium for consortium development

The authors of this chapter have developed a consortium from waste water–fed fish pond at East Kolkata Wetland (EKW), India (22° 27′ N 88° 27′ E) [1] in synthetic medium (DSMZ 641) specific for growing SRB under anaerobic condition, which could reduce soluble sulphate from 1600 ppm to discharge level within three and half hours of incubation at room temperature in a packed bed reactor with stable biofilm for sustained treatment of soluble sulphate. The geographical orientation in terms of slope is such that the entire city's (Kolkata's) run off (which includes contribution of acid rain) drains at EKW. However, there is no toxicity reported in these water bodies. Hence, there is high possibility of these water bodies harbouring efficient SRB. The selection of medium for growth, the inoculum for development of the consortium and the subsequent selection pressures were carefully monitored keeping in mind the need to specifically enrich the SRB with minimal non-SRB so as to ensure insignificant dead mass during bioreactor operation, hence developing a tailor-made consortium for this purpose. Its performance was tested for sulphate reduction from modified synthetic medium (DSMZ 641) prepared using tap water and mining effluent.

Synthetic medium for growing the consortium

For 1 litre of medium **DSMZ 641**, following is the composition:

Solution A

NH_4Cl	1.0 g
Na_2SO_4	2.0 g
$Na_2S_2O_3 \times 5\ H_2O$	1.0 g
$MgSO_4 \times 7\ H_2O$	1.0 g
$CaCl_2 \times 2\ H_2O$	0.1 g

KH_2PO_4	0.5 g
Yeast extract	1.0 g

Then, a pinch of Resazurin is added, which is used as a redox indicator.

Solution B

$Na_2S_2O_4$	0.1 g
$NaHCO_3$	1.68 g
Lactic acid	12 ml
NaOH	4.4 g

Solution C: Trace element solution 1.0 ml (SL10)

HCl (25%; 7.7 M)	10.0 ml
$FeCl_2 \times 4\ H_2O$	1.5 g
$ZnCl_2$	70.0 mg
$MnCl_2 \times 4\ H_2O$	0.1 g
H_3BO_3	6.0 mg
$CoCl_2 \times 6\ H_2O$	190.0 mg
$CuCl_2 \times 2\ H_2O$	2.0 mg
$NiCl_2 \times 6\ H_2O$	24.0 mg
$Na_2MoO_4 \times 2\ H_2O$	36.0 mg
Distilled water	990.0 ml

Solution D: Vitamin solution 10 ml

Biotin	2.0 mg
Folic acid	2.0 mg
Pyridoxine	10.0 mg
Thiamine HCl ×	$2H_2O$ 5.0 mg
Riboflavin	5.0 mg
Nicotinic acid	5.0 mg
D-Ca-pantothenate	5.0 mg
Vitamin B_{12}	0.10 mg
P-amino benzoic acid	5.0 mg
Lipoic acid	5.0 mg
Distilled water	1000.0 ml

Sodium azide is also added to prevent the fungal formation.

The following are the modified medium components, which were effective for SRB in terms of nutrient consumption. This medium is far more advantageous in terms of cost and amount of consumption. It is similar to the aforementioned media composition with a minor change in components such as ammonium chloride—50% of previously mentioned medium, KH_2PO_4—25% and yeast extract—50%.

Composition of the mining effluent

Sodium (17.5 ppm), potassium (37.3 ppm), manganese (0.03 ppm), nickel (0.026 ppm), magnesium (17.6 ppm), calcium (540 ppm), total carbon (5.893), inorganic carbon (4.477) and total organic carbon (1.419).

Microorganism preferentially gets attached to the surfaces in favourable conditions like moist surface along with the nutrients as a layer called biofilm. Earlier reports indicated the presence of surfaces to stimulate attached bacterial growth under conditions, which are otherwise too dilute to sustain the microbes [22]. The operation was scaled up to 220 litres. The system involved three columns in series of 78, 71 and 71 litres (**Figure 1**). It showed an efficiency of above 50% soluble sulphate (starting from 1600 ppm) reduction within three and half hours under ambient temperature during both batch and continuous modes. The sulphate reduction varied from 65% to 100% within 24 hours. The biofilm could be well sustained in both polypropylene and steel matrix (**Figure 2**) without any maintenance for more than 18 months.

Figure 1. 220-litre packed bed bioreactor for soluble sulphate removal with steel and polypropylene immobilization substrate with defined surface area for bacterial biofilm formation.

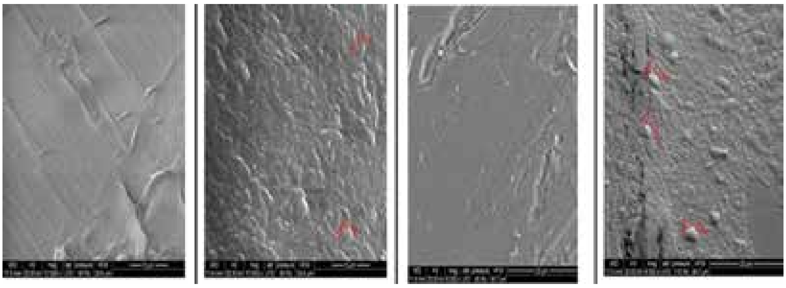

Figure 2. Scanning electron microscopic image of different matrix with and without SRB biofilm. From extreme left, polypropylene matrix (without biofilm), polypropylene matrix (with biofilm), steel matrix (without biofilm), and steel matrix (with biofilm).

3. Optimization of inoculum percentage and immobilization matrix

Inoculum optimization was done based on the extent of sulphate reduction following immobilization of the consortium onto a matrix as per the method of Nasipuri et al. [1]. The inoculum percentage was varied from 2% to 50% (2%, 5%, 10%, 20%, 30%, 40% and 50%) to maximize the sulphate reduction by the system. Optimum sulphate reduction of 70% was obtained with 10% primary inoculum. It implied that with 10% bacterial inoculum maximum metabolic rate was reached, which eventually resulted in a significant sulphate reduction under optimum condition. But further increase in inoculum percentage resulted in no further increase in efficiency in terms of sulphate reduction.

Two types of matrices (polypropylene and steel) with uniform surface areas were tested for the purpose as per the method of Nasipuri et al. [2]. The stainless steel and polypropylene raschig rings showed an overall sulphate reduction of 72.05% and 69.59%, respectively. They were equally efficient as immobilization matrix in terms of sulphate reduction under the same set of conditions. The comparable range of efficiency between stainless steel and polypropylene raschig ring in terms of sulphate reduction might be due to equal lower pressure drop at effective surface areas and same gas velocity. Our data were also supported by the study of Kolev et al. [23]. In this regard, the scanning electron microscopic images were further used to visualize the dense biofilm formation on both types of matrices (**Figure 2**).

4. Biofilm formation and sulphate reduction

Biofilm, a thick layer of microbial cells embedded into secreted extracellular material on inert matrix such as polypropylene or metals, acts as a constant source of inoculum for the system. The method was adopted from Nasipuri et al. [1]. Two millilitre of sample was centrifuged at 10,000 rcf for 10 minutes to pellet down the cells. The supernatant was mixed with 98 ml of distilled water in a 250-ml conical flask. A 5 ml of conditioning mixture containing hydrochloric acid (6%), isopropanol (20%), water (64%) and glycerol (10%) was added to it for proper mixing. The mixture was then put onto a magnetic stirrer at the maximum speed for 1 minute with a pinch of barium chloride. The solution was then allowed to stand for 2 minutes for settling the barium sulphate precipitate. The absorbance was taken at 420 nm for soluble sulphate measurement using a dual-beam spectrophotometer by Agilent Technologies.

Similarly, for measurement of biofilm, the method of Martin [24] was adopted. The biofilm-containing matrix was firstly stained for 10 minutes with crystal violet. Vigorous washing was done with distilled water to wash away the loosely bound stain. Ninety-five percent of ethanol was then added to remove the bound stain from the biofilm. The absorbance of the removed stain was measured at 620 nm for biofilm thickness measurements using a dual-beam spectrophotometer by Agilent Technologies.

The effect of biofilm formation by SRB consortium on sulphate reduction was checked for 90 days. The biofilm thickness (left) compared with sulphate reduction (right) performed by the system for the above-mentioned period (**Figure 3a** and **b**) revealed oscillatory nature of both biofilm formation and associated sulphate reduction. It is an inherent nature of a biofilm-based system. The biofilm thickness was not directly correlated with the extent of reduction. This is because biofilm thickness as reflected by the method of Martin et al. [24] consists of active cells, inactive cells and the extracellular polymeric substances, although the reduction is due to the function of just the active cells. Hence, both show an oscillatory pattern but are not directly dependent on one another. The evidence of an oscillatory nature in biofilms was also observed by others [25, 26], which eventually supported the former statement.

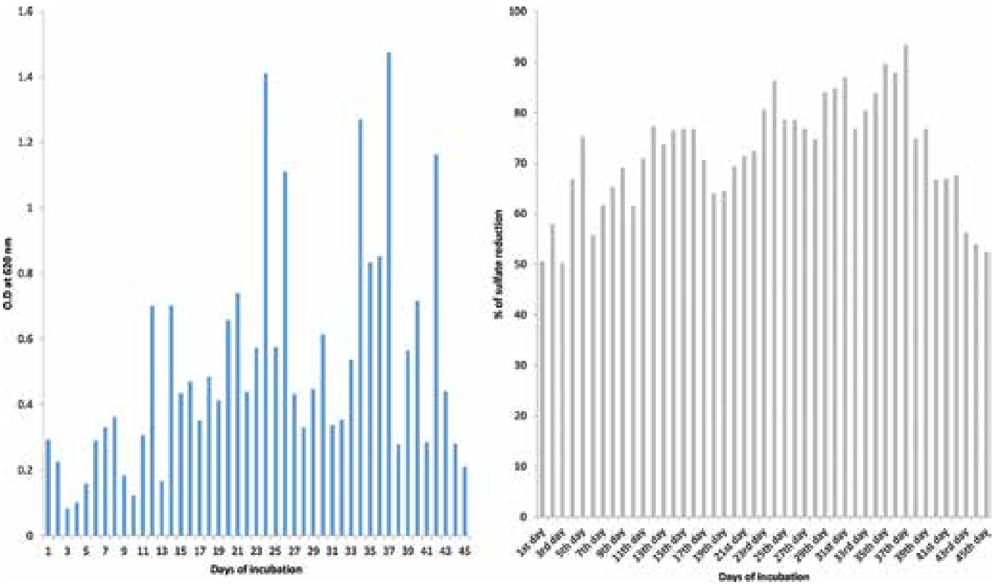

Figure 3. Graphical representation of biofilm formation by the SRB consortium on matrix (left) with associated sulphate reduction (right).

5. Performance of the bioreactor

The performance of the bioreactor in terms of sulphate reduction efficiency of the system starting from an initial concentration of 2000 ppm was measured after 24 hours of incubation according to the method of Nasipuri et al. [1] for a period of 361 days (**Figure 4**). The quarterly data revealed 36.29 ± 16.55, 63.46 ± 15.24, 57.44 ± 17.32 and 91.81 ± 7.97 sulphate reduction, respectively, indicating stabilization of the bioreactor. The data generated from the bioreactor were used for carrying out the time series analysis after detrending (**Figure 5**) the series using Matlab 7.4.0 (R2007a) to study the bioreactor performance in terms of sulphate reduction. The time series plot (**Figure 5**) clearly reflects the inherent oscillatory nature of the system as has been reported earlier by other investigators [25]. This oscillatory nature is an inherent property of the biofilm-based system. Taherzadeh reported such oscillatory property in case of continuous mode operations of reactors due to shearing force, but in this case, the same property is observed even in case of batch mode operation as an outcome of biofilm property, where there exists only minimum of shearing force [27]. However, the impact of seasonal variation may also be important. The effect of seasonal variation on the performance of the system was analysed (**Figure 6**). Its performance appears to be independent of the seasonal variation. This is a positive finding in terms of application of this system on site. Hence, the correlation between ambient temperature and age of the biofilm with that of the performance of the system was determined using Pearson's correlation coefficient. The correlation coefficient among sulphate reduction and biofilm formation, biofilm formation and ambient temperature, sulphate reduction and ambient temperature was observed to be 0.738, 0.538 and 0.284, respectively. It was observed that there was no statistical trend in performance of the system with either ambient temperature or age of the biofilm. It was revealed that the two variables were not related (**Figure 6b**).

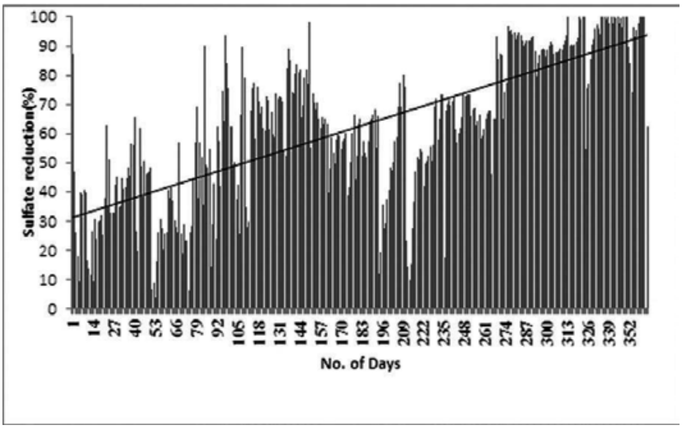

Figure 4. Performance of the SRB consortia in 78-litre packed bed bioreactor for 361 days. The 78-litre bioreactor is constructed of acrylic body and stainless steel for the bottom portion with three nozels for sample collection (distance between first and second nozels is 18 cm, whereas the distance between second and third nozels is 40 cm. The anaerobicity was mentioned by purging nitrogen gas (60 lm/cm^2) into the bioreactor from outside.

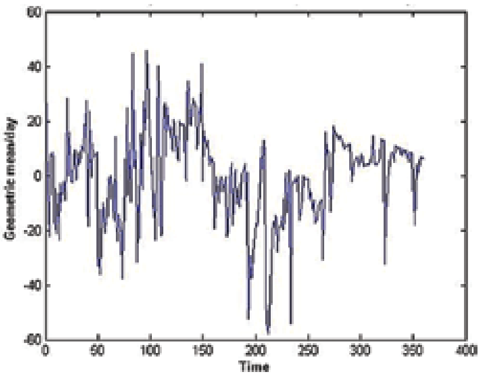

Figure 5. Time series of geometric mean of sulphate dataset after removing trend.

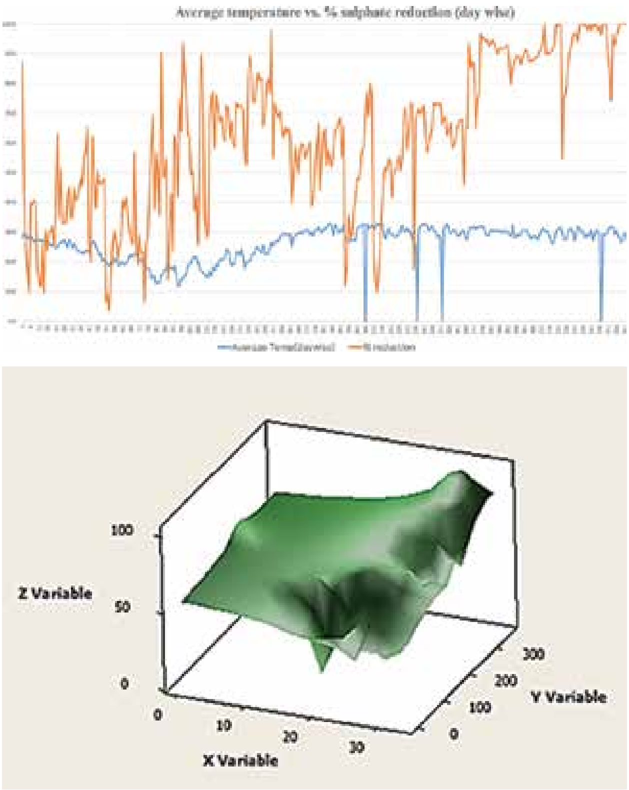

Figure 6. (a) Graph representing biofilm performance in term of sulphate reduction and temperature variation with days. Sulphate reduction indirectly indicates the active biofilm at any point of time. *X* axis represents days that the reactor was functioning, whereas *Y* axis represents performance of the system in terms of sulphate reduction in orange colour and ambient temperature in blue. (b) Surface plot among *X*, *Y* and *Z* variables, where *Z* variable is the percent sulphate reduction, *Y* variable is the age of the biofilm in days and *X* variable is the ambient temperature in degree centigrade.

6. Scalability of the process

The sulphate reduction was monitored under anaerobic condition in a 9-litre bioreactor for 25 days, and the percentage of mean reduction was 56.3 ± 11.03. In case of 78-litre bioreactor, the sulphate reduction was monitored for 361 days, and the percentage of average reduction was 62.36 ± 24.81 with the saturation obtained at around 331 days. The probability distribution of the data was found to be normally distributed. It was evident from the above observations that the efficiency of sulphate reduction was increased by 1.10-fold with scaling up of the bioreactor volume. Our results were quite similar to the study of Sarti et al. [28], where they had also successfully demonstrated sulphate reduction in an anaerobic bioreactor with maximum efficiency of 99%. A similar study of fed batch bioreactor used for sulphate reduction was demonstrated by Silva et al. in the year 2002 with an efficiency of 97% [29]. Although both the studies are similar to ours in terms of reduction efficiency, but unlike those, our system retains the reduction efficiency consistently once it gets stabilized.

7. Optimization of the time of sulphate reduction

The sulphate reduction was further optimized in terms of incubation time in the same bioreactor under identical conditions. The desired level of reduction (for environmental discharge) was reached within three and half hours (**Figure 7**). The data were fitted using Origin8pro (**Figure 8**), which resulted in a polynomial equation of order 5 with $r^2 = 0.97$. The following equation perfectly expresses this desulfurization system:

$$Y = 0.941 + 160.51x - 182.51x^2 + 83.8x^3 - 18.14x^4 + 1.39x^5 \qquad (1)$$

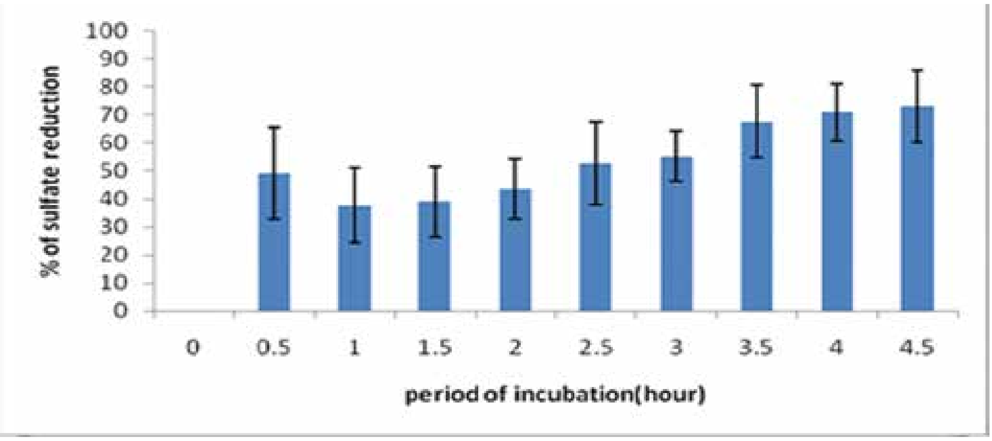

Figure 7. Time course of sulphate reduction by the packed bed bioreactor.

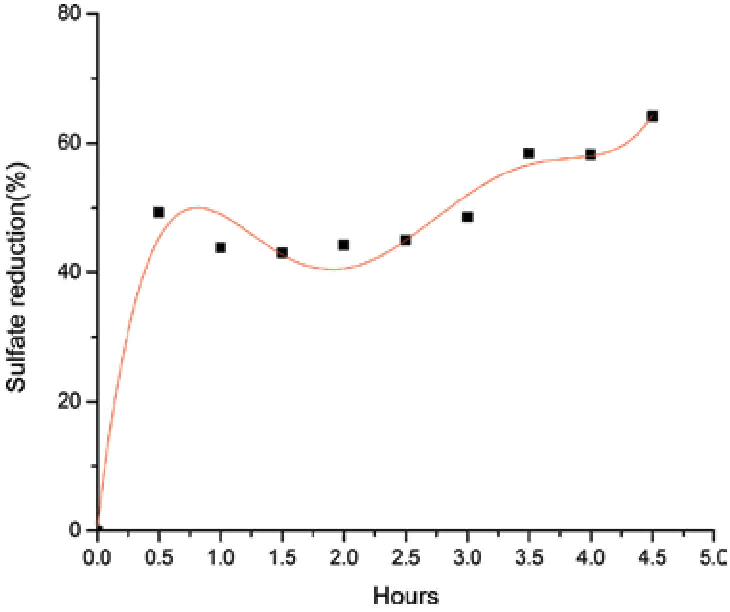

Figure 8. Fifth-order polynomial equation of time optimization of sulphate reduction using Origin8pro.

Here Y denotes the percentage of sulphate reduction, and x signifies the time required for reduction in hours.

8. Effect of height of the bioreactor on performance

The oscillatory nature of the bioreactor performance in terms of sulphate reduction was further analysed by calculating the running mean of the sulphate reduction of the samples taken from each port of the bioreactor as described in **Figure 4**. The result indicated that significant amount of sulphate reduction was observed between the first and second ports (18 cm), in contrast, there was no significant reduction between the second and third ports (40 cm; **Figure 9**). As an explanation to this observation, it can be argued that the compromised performance in the upper layer could be due to the accumulation of hydrogen sulphide gas generated by the system, which has a negative impact on system performance. The phenomenon was also supported by the report of Frank et al. in the year 2013 [30]. To decrease the dead space (where the performance is compromised) and enhance the efficiency of the system, an alternative reactor design was tested (**Figure 10**). Similar designs for one vertical system and one horizontal system were constructed and tested (**Figure 10b**). The performance of the two systems was found to be similar with no significant statistical variation observed using z test for the equality of two means with unknown variances and moderate sample sizes (n = 47 in case of both vertical and horizontal designs). The results are displayed in **Table 1**.

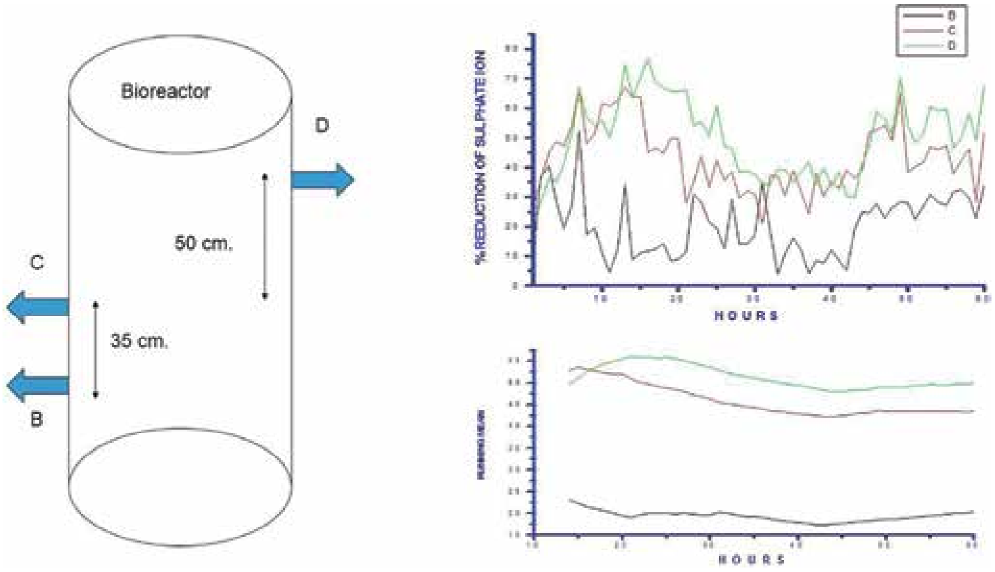

Figure 9. Left panel shows the position of the ports on the bioreactor column. The right top panel shows actual sulphate reduction at the different ports, whereas the right bottom panel shows running mean of sulphate reduction from three different ports of the bioreactor for 60 hours. Bottom curve for the first port, middle one for the second port and the upper curve was for the third port.

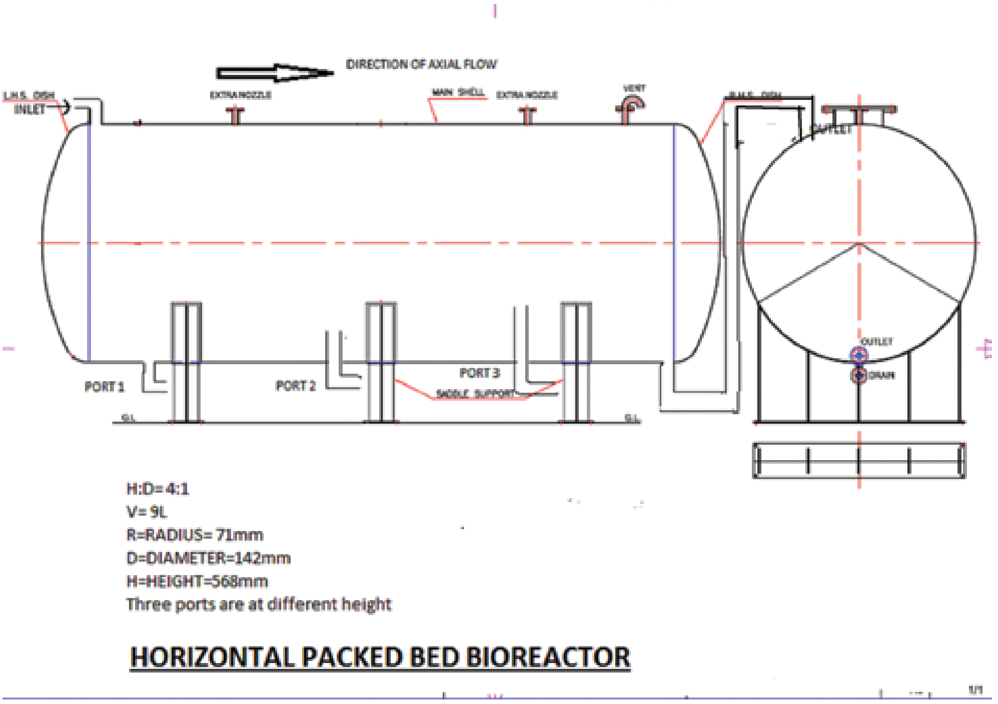

Figure 10. (a) Modified design of packed bed bioreactor. (b) Actual bioreactors constructed using plastic material.

z **Test: two sample test for equality of means with unknown population variances and large sample sizes**	H_0: $\mu_1 = \mu_2$ **Variable 1**	H_1: $\mu_1 \neq \mu_2$ **Variable 2**
Mean	50.27085106	48.98255319
Known variance	267.57	302.71
Observations	47	47
Hypothesized mean difference	0	
Z	0.369846189	
$P(Z \leq z)$ one tail	0.355748549	
z Critical one tail	1.644853627	
$P(Z \leq z)$ two tail	0.711497098	
z Critical two tail	1.959963985	

Table 1. Statistical validation of sulphate reduction using different designs of the bioreactor.

From the above observation, it was clear that the diminished performance in the upper layer was not due to accumulated hydrogen sulphide gas. There might be other factors responsible for this performance variation. As the bioreactor design was proper for the current system under investigation, the optimization of process was done using response surface methodology (RSM) under ambient condition and implemented using design expert 9 software as displayed in **Table 2**. Experimental and predicted responses were found to be broadly similar.

		Factor 1	Factor 2	Response 1	Predicted
Standard	Run	A: sulphate concentration (ppm)	B: flow rate (litre/hour)	Sulphate reduction (%)	Sulphate reduction (%)
3	1	719.67	2.82	59.66	55.62
4	2	1780.33	2.82	66.05	60.3
8	3	1250.00	3.00	46.54	56.57
1	4	719.67	1.98	60.72	58.46
9	5	1250.00	2.40	49.07	50.63
13	6	1250.00	2.40	49.07	50.63
2	7	1780.33	1.98	68.21	60.3
11	8	1250.00	2.40	49.07	50.63
10	9	1250.00	2.40	49.07	50.63
12	10	1250.00	2.40	49.07	50.63
5	11	500.00	2.40	58.63	54.05
7	12	1250.00	1.80	53.85	52.93
6	13	2000.00	2.40	63.6	58.79

Table 2. Table representing the experimental design for system optimization using response surface methodology.

From the above analysis, the optimum sulphate reduction condition was determined at an initial sulphate concentration of 1250 ppm and at a flow rate of 1.8 litre/hour (**Figure 11**). The mathematical equation derived from the model is given below. The values of each term are given in the coefficient table (**Table 3**).

$$\text{Equation for sulphate reduction} = 49.07 + 2.61 \times A - 1.69 \times B - 0.28 \times AB + 8.02 \times A^2 + 2.56 \times B^2 \quad (2)$$

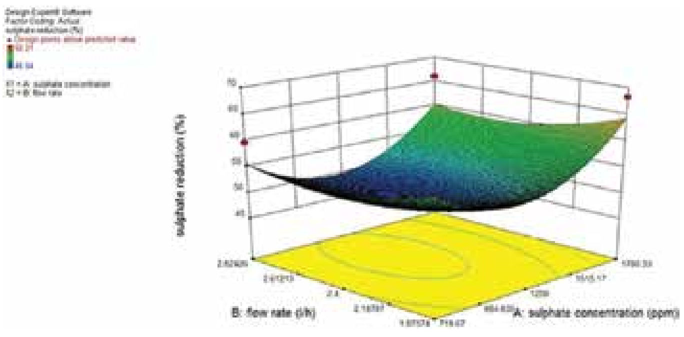

Figure 11. The model graph for sulphate reduction in response to sulphate concentration and flow rate.

Response	Intercept	A	B	AB	A^2	B^2
Sulphate reduction	49.07	2.61358	−1.69474	−0.275	8.02375	2.56375
p		0.1428	0.3199	0.9057	0.0021	0.1748
Legend		$p < 0.01$	$0.01 \leq p < 0.05$	$0.05 \leq p < 0.10$	$p \geq 0.10$	

Table 3. Statistical validation of the optimization study.

where A is the sulphate concentration, and B is the flow rate.

9. Conclusion

The work contained in this chapter describes a biofilm-based soluble sulphate reduction system operating within 3.5 hours using a well-characterized SRB consortium from 1600 ppm to discharge level under ambient condition. This ensures the treatment of 1509 litres of sulphate solution in 24 hours using a 220-litre bioreactor. A single-unit bioreactor would be the ideal configuration for this consortium. Time kinetics of sulphate reduction yielded a parabolic form significantly ($r^2 = 0.99$; $p < 0.05$). Rate of sulphate reduction was found to be independent of seasonal variation. The bioreactor designs tested during this study had practically no effect on the performance of the system. This system was the fastest sulphate-reducing system at pilot scale, which could run without maintenance for a long time with the ability to withstand an initial sulphate concentration of 1250 ppm at a flow rate of 1.8 litre/hour optimally under ambient condition. Hence, the process has been filed as an Indian patent and a PCT to protect the intellectual property associated with this invention. It has immense application for industrial effluent treatment in future.

Acknowledgements

The authors would like to acknowledge the financial assistance of Ministry of Human Resource Development (MHRD), Government of India (GOI) under the FAST scheme for conducting part of the work; Department of Atomic Energy, GOI for initiating the work and scaling it up to 220 litres; Department of Biotechnology, GOI for providing fellowship to Poulami Datta, Shashi Bhushan, Ganesh Prasath Krishnan and Swati Bhatt; Department of Science and Technology, GOI under the DST Inspire Scheme for providing fellowship to Sourav Ghosh and MHRD for the fellowship of Chaitali Chanda. The authors would like to thank Late Sourav Chakratorty, Arpan Pal and Abhishek Mitra for their technical assistance. The authors would like to thank Dr. Gauri G. Pandit and Dr. Tessy Vincent of Bhabha Atomic Research Centre for their intellectual inputs during the execution of the project.

Author details

Shaon Ray Chaudhuri[1,2*], Indranil Mukherjee[3], Debabrata Datta[4], Chaitali Chanda[3], Ganesh Prasath Krishnan[2], Swati Bhatt[2], Paulami Datta[2], Shashi Bhushan[2], Sourav Ghosh[1], Pinaki Bhattacharya[6], Ashoke Ranjan Thakur[7], Debanik Roy[5] and Parthasarathi Barat[3]

*Address all correspondence to: shaonraychaudhuri@tripurauniv.in, shaon.raychaudhuri@gmail.com

1 Department of Microbiology, Tripura University, Suryamaninagar, Tripura West, India

2 Department of Biotechnology, Maulana Abul Kalam Azad University of Technology, West Bengal (formerly known as West Bengal University of Technology), Salt Lake, Kolkata, India

3 Centre of Excellence in Environmental Technology and Management, Maulana Abul Kalam Azad University of Technology, West Bengal (formerly known as West Bengal University of Technology), Salt Lake, Kolkata, India

4 Computational Radiation Physics Section, Health Physics Division, Bhabha Atomic Research Centre, Mumbai, India

5 Scientist (Robitics) & Chief Program Co-ordinator, Board of Research in Nuclear Sciences (BRNS), Department of Atomic Energy, Bhabha Atomic Research Centre, Mumbai, India

6 Department of Chemical Engineering, Heritage Institute of Technology, Kolkata, West Bengal, India

7 Formerly at West Bengal State University, Barasat, Berunanpukuria, P.O. Malikapur, Kolkata, West Bengal, India

References

[1] Nasipuri P, Pandit GG, Thakur AR, Raychaudhuri S. Comparative study of soluble sulphate reduction by bacterial consortia from varied regions of India. Am J Envsci. 2010; 6: 45–46. DOI: 10.3844/ajessp.2010.152.158

[2] Nasipuri P Pandit GG, Thakur AR, Raychaudhuri S. Microbial consortia from taptapani hot water springs for mining effluent treatment. Am J Microbiol. 2010; 1: 23–29. http://thescipub.com/PDF/ajmsp.2010.23.29.pdf (last accessed 28 January 2016).

[3] Janssen AJH, Dijkman H, Janssen G. Novel biological processes for the removal of H_2S and SO_2 from gas streams. In: LensPNL, Hulshoff PolLW (Eds.), Environmental Technologies to Treat Sulfur Pollution – Principles and Engineering. London: International Water Association, 2000, 265–280.

[4] ISO. Water Quality—Determination of Sulfate. Geneva: International Organization for Standardization (ISO 9280:1990), 1990. http://www.iso.org/iso/iso_catalogue/catalogue_tc/catalogue_detail.htm?csnumber=16932 (last accessed 28 January 2016).

[5] Dhew US. Drinking Water Standards—1962. Washington, DC: US Department of Health, Education and Welfare, Public Health Service; US Government Printing Office (Publication No. 956), 1962. http://nepis.epa.gov/ (last accessed 28 January 2016).

[6] Bowell RJ. A review of sulphate removal options for mine water. In: Jarvis AP, Younger PL (Eds.), Mine Water, Proceeding International Mine Water Association Symposium 2, 2004, 55–91. University of Newcastle, UK.

[7] Vallero MV, Lettinga GN, Lens PN. High rate sulfate reduction in a submerged anaerobic membrane bioreactor (SAMBaR) at high salinity. J Mem Sci. 2005; 253: 217–232. DOI: 10.1016/j.memsci.2004.12.032

[8] Caumette P, Cohen Y, Matheron R. Isolation and characterization of *Desulfovibriohalophilussp*. a halophilicsulfate-reducing bacterium isolated from Solar Lake (Sinai). Syst Appl Microbiol. 1991; 14: 33–38. DOI: 10.1016/S0723-2020(11)80358-9

[9] Ollivier B, Hatchikian CE, Premier G, Guezennec I, Garcia J. *Desulfohalobiumretbaense*gen. nov., sp. nov., a halophilicsulfate-reducing bacterium from sediments of a hypersaline lake in Senegal. Int J Syst Bacteriol. 1991; l41: 74–81. DOI: 10.1099/00207713-41-4-595

[10] Jones HE, Trudinger PA, Chambers LA, Pyliotis NA. Metal accumulation by bacteria with particular reference to dissimilatory sulphate-reducing bacteria. Z Allg Mikrobiol. 1976; 16: 425–435. DOI: 10.1002/jobm.19760160603

[11] Karkhoff RRS, Huber DPW, Voordouw G. Conservation of the genes for dissimilatory sulfite reductase from *Desulfovibrio vulgaris* and *Archaeoglobus fulgidus* allows their detection by PCR. Appl Environ Microbiol. 1995; 61: 290–296. http://aem.asm.org/content/61/1/290.full.pdf (last accessed 28 January 2016).

[12] Minz D, Flax JL, Green SJ, Muyzer G, Cohen Y, Wagner M, Rittmann BE, Stahl DA. Diversity of sulfate-reducing bacteria inoxic and anoxic regions of a microbial mat characterized by comparative analysis of dissimilatory sulfite reductase genes. Appl Environ Microbiol. 1999; 65: 4666–4671. DOI: 10.1128/AEM.71.10.6353-6359.2005

[13] Fardeau ML, Ollivier B, Hirschler-Rea A, Khelifi N. Use of thermophilic sulphate-reducing archaea for the implementation of a process for the degradation of hydrocarbons. US 8455240 B2; 2006. PCT/FR2006/001541.

[14] Molwantwa JB, Molipane NP, Rose PD. Biological sulphate reduction using algar extracellular products as a carbon source. In: WISA 2000 Biennial Conference, Sun City, South Africa, 28 May–1 June 2000.

[15] Singh R, Kumara A, Kirroliaa A, Kumarb R, Yadava N, Bishnoia NR, Rajesh K. Removal of sulphate, COD and Cr(VI) in simulated and real wastewater bysulphate reducing

bacteria enrichment in small bioreactor and FTIR study. Biores Technol. 2011; 102: 677–682. DOI: 10.1016/j.biortech.2010.08.041

[16] Pawels R, Haridas A, Jose BT. Biological sulphate reduction with hydrogen in a get loop biofilm reactor. Int J Sci Res Publ. 2013; 3: 1–12. http://www.ijsrp.org/research-paper-0613/ijsrp-p1858.pdf (last accessed 28 January 2016).

[17] Chaudhuri SR, Thakur AR, Vincent T, Roy D, Wattal PK, Ghosh SK. Method of treating sulphate containing water 2015; WO 2015071833 A1; 2014. PCT/IB2014/065982.

[18] Beyenal H, Rajesh K, Sani BM, Peyton AC, Dohnalkova JE, Lewandowski AZ. Uranium immobilization by sulfate-reducing biofilms. Environ Sci Technol. 2004; 38: 2067–2074. DOI: 10.1021/es0348703

[19] Singh JS, Abhilash PC, Singh HB, Singh RP, Singh DP. Genetically engineered bacteria: an emerging tool for environmental remediation and future research perspectives. Gene 2011; 480: 1–9. DOI: 10.1016/j.gene.2011.03.001

[20] Edwards KJ, Bond PL, Gihring TM, Banfield JF. An archaeal iron-oxidizing extreme acidophile important in acid mine drainage. Science 2000; 287: 1796–1799. DOI: 10.1126/science.287.5459.1796

[21] Mitra A, Mukhopadhyay S. Biofilm mediated decontamination of pollutants from the environment. Bioengineering 2016; 3: 44–59. DOI: 10.3934/bioeng.2016.1.44

[22] Heukelekian H, Heller A. Relation between food concentration and surface for bacterial growth. J Bacteriol. 1940; 40: 547–558. DOI: 10.1111/j.1462-5822.2006.00761.x

[23] Kolev N, Nakov S, Jutzkan L, Ljutzkanov Kolev D. Comparison of the effective surface area of some highly effective random packings. IChemE 2006; Symposium Series No. 152. DOI: 10.1016/j.cep.2005.10.008

[24] Martin R, Soberon N, Vaneechoutte M, Florez AB, Vazquez F, Suarez JE. Characterization of indigenous vaginal lactobacilli from healthy women as probiotic candidates. Int Microbiol. 2008; 11: 261–266. DOI: 10.2436/20.1501.01

[25] Horn H, Lackner S. Modeling of biofilm systems: a review. Adv Biochem Eng Biotechnol. 2014; 146: 53–76. DOI: 10.1007/10_2014_275

[26] Trulear MG, Characklis WG. Dynamics of biofilm processes. J Water Pollut Control Fed. 1982; 54: 1288–1301. DOI: 10.2307/25041684

[27] Taherzadeh D, Picioreanu C, Küttler U, Simone A, Wall WA, Horn H. Computational study of the drag and oscillatory movement of biofilm streamers in fast flows. Biotechnol Bioeng. 2010; 105: 600–610. DOI: 10.1002/bit.22551

[28] Sarti A, Silva AJ, Zaiat M, Foresti E. Full-scale anaerobic sequencing batch biofilm reactor for sulfate-rich wastewater treatment. Desal W Treat. 2011; 25: 13–19. DOI: 10.1002/bit.22551

[29] Silva AJ, Varesche MB, Foresti E, Zaiat M. Sulphate removal from industrial wastewater using a packed-bed anaerobic reactor. Pro Biochem. 2002; 37: 927–935. DOI: 10.1016/S0032-9592(01)00297-7

[30] Frank KL, Rogers DR, Olins HC, Vidoudez C, Girguis PR. Characterizing the distribution and rates of microbial sulfate reduction at Middle Valley hydrothermal vents. ISME J. 2013; 13: 1751–7362. DOI: 10.1038/ismej.2013.17

Chapter 3

Monte Carlo Simulations of Nuclear Fuel Burnup

Raghava R. Kommalapati, Fiifi Asah-Opoku,
Hongbo Du and Ziaul Huque

Additional information is available at the end of the chapter

http://dx.doi.org/10.5772/62572

Abstract

In the operation of a nuclear power plant, it is very important to determine the time evolution of material composition and radionuclide inventory during the entire operation of the plant. In the experiments, the Monte Carlo N-Particle eXtended (MCNPX) code was found to be accurate in predicting the uranium fuel depletion, the plutonium production and the buildup of most of the fission products in a nuclear reactor. The goal in this chapter is to analyze the effect of different nuclear fuel grades on the total radioactivity of the reactor core by employing nuclear burnup calculations for the three different fuels: mixed oxide fuel (MOX), uranium oxide fuel (UOX) and commercially enriched uranium (CEU), utilizing simulations with MCNPX code. The calculated results indicate that there is a buildup of plutonium isotopes for UOX and CEU, whereas there is a decline in the plutonium radioisotopes for MOX fuel with burnup time. The study of reactor neutronic parameters showed UOX fuel performs better relative to MOX and CEU. Zircaloy, with low thermal neutron absorption cross-section and high thermal conductivity, produced better results for the effective multiplication factor K_{eff} and hence proved to be a much more effective clad material.

Keywords: nuclear fuel, MCNPX code, burnup, radionuclide inventory, fuel burnup

1. Introduction

Use of nuclear energy as a sustainable energy supply has both good and harmful effects like every other natural resource. The issue is mostly with the spent nuclear material that is left after the energy extraction which is no longer efficient in the splitting of its atoms to produce energy. This residual material is known as spent nuclear fuel (SNF) and contains highly radioactive elements such as uranium and plutonium. In the operation of a nuclear power plant, it is important to determine the time development of material composition and radionuclide inventory during the entire operation of the plant. The determination of plutonium (Pu) in environmental samples is also important for investigating radiotoxicity and the long-term radiation effects on humans that are attributed to Pu rather than the other transuranic elements [1]. The determination of the elemental and isotopic compositions of Pu in spent nuclear fuels is required for fuel characterization [2], and also the management of radioactive waste [3]. According to the U.S Nuclear Regulatory Commission, the elements contained in high-level waste include plutonium-239 (half-life: 24,000 years) and plutonium-240 (half-life: 6800 years). The content of Pu isotopes in high burnup spent nuclear fuel samples (33.21–59.03 GWd/MtU) were determined by alpha and mass spectrometry [4]. While it may be necessary to determine Pu content in spent fuel due to the extremely long half-life of Pu, it is also important to quantify spent fuel based on the total concentrations of key actinides and non-actinides to estimate the entire radioactive hazard posed by these fuels.

Much research work has been done in the area of sustainable nuclear energy. Some research work on nuclear burnup calculations focused on the analysis of the accuracy of the Monte Carlo Nuclear Particle (MCNP) Code as compared to other computer codes such as BUCCAL 1, GETERA Code and others. Accuracy of the new Monte Carlo based burnup computer code has been studied [5]. The research involved direct usage of neutron absorption tally generated by MCNP5 to determine new nuclide inventories. This eliminates the need to calculate neutron fluxes as input to other computer codes to generate the nuclide inventories and thus incorporates fully the capabilities of MCNP. Code-to-code comparison of BUCAL 1 with several burnup codes showed good agreement. The research shows the accuracy of the Monte Carlo Code in predicting the depletion and generation of radionuclide inventories. Monte Carlo burnup simulations of isotope correlation experiments have also been determined using the NPP Obrigheim [6]. In the experiment, the Monte Carlo Nuclear Particle eXtended (MCNPX) code was found to be accurate in predicting the uranium fuel depletion, the plutonium production and the buildup of most of the fission products in a nuclear reactor. The direct integration of the cinder.dat file as the decay code for MCNPX makes it more accurate than in previous experiments when the MCNP transport code is simply linked to other codes such as ORIGEN.

The GETERA code [7] was used to calculate fuel burnup in a miniature neutron source reactor (MNSR). A list of 19 radionuclides, including 13 fission products and 6 actinides, was identified and the total radioactivity of the MNSR at the end of the reactor core life was calculated based on these nuclides. This was found to be 9.462×10^{13} Bq. This research used highly enriched uranium as fuel in the MNSR core and does not provide comparisons of the radiological hazards associated with other fuels. The results from the research indicated that the amount of 235U and 238U after burnup decreased about 13.669 and 0.065 g, respectively, thus predicting again the accuracy of the code in estimating the depletion of uranium.

The next section gives details on the Monte Carlo methods for simulating the fuel burnup in nuclear power plants in this research. The three different fuel grades, mixed oxide fuel (MOX), uranium oxide fuel (UOX) and commercially enriched uranium (CEU), would be used for the fuel burnup simulations. Also, three different clad materials (zirconium, zircaloy and stainless steel) would be investigated based on their influence on the K_{eff}.

2. Methodology

2.1. Monte Carlo methods for nuclear plants

The principle behind the MCNP is statistical sampling, which makes use of the randomness of numbers. The MCNP records the trajectory of neutrons emitted by a source and determines whether the neutron is able to penetrate a shield after interacting with radioisotopes on the shield [8, 9]. The set-up for the simulation using MCNP5 in this study is made up of three main interacting packages of software obtained from the Radiation Safety Information and Computational Center of the Oak Ridge National Laboratory, Tennessee, USA. These three packages are MCNP1.05/MCNPX, CINDER 1.05 and MONTEBURNS 2.0.

The whole simulation process starts with an input data file to the MCNP5 as shown in **Figure 1**. Some of the parameters in the input data file include initial material compositions, geometry specifications (cell and surface cards), material specifications and source definition cards. Based on the output data required, MCNP produces a wide variety of output data files. Keys among these output files will be the group cross-sections and the neutron fluxes of materials. MONTEBURNS, which links MCNP5 and CINDER, transfers one group cross-section and neutron fluxes generated by MCNP to CINDER. This serves as the burnup or decay code for the set-up. CINDER processes these input files and generates output results such as burnup values and final material compositions. The resulting material compositions are transferred again to MCNP in a repeated or cyclic process. The end of a cycle repents the end of a burnup step. The next burnup step continues with the next cycle.

2.2. The MCNPX code

MCNPX is a software package popularly used to simulate various kinds of reactions pertaining to neutron, photon, electron transport and radioactive particles. This computer code package also has the capability of simulating nuclear burnup reactions and calculating the radionuclide inventory due to fission of fissile or fissionable isotopes and transmutation of parent nuclides. The code eliminates the need for the combination of the MCNP code with the nuclear burnup code ORIGEN or CINDER, in which one group cross-sections and fluxes are transferred from MCNP to the decay code ORIGEN or CINDER using monteburns. The MCNPX code has the CINDER.dat file responsible for nuclear fuel burnup as part of its buildup which allows the direct transfer of one-group reaction rates (cross-sections) and 63 group neutron fluxes to the depletion code cinder for decay calculations. In this study, the MCNPX is used to simulate nuclear fuel burnup calculations for a pressurized water reactor system using three different fuel grades: UOX, CEU and MOX.

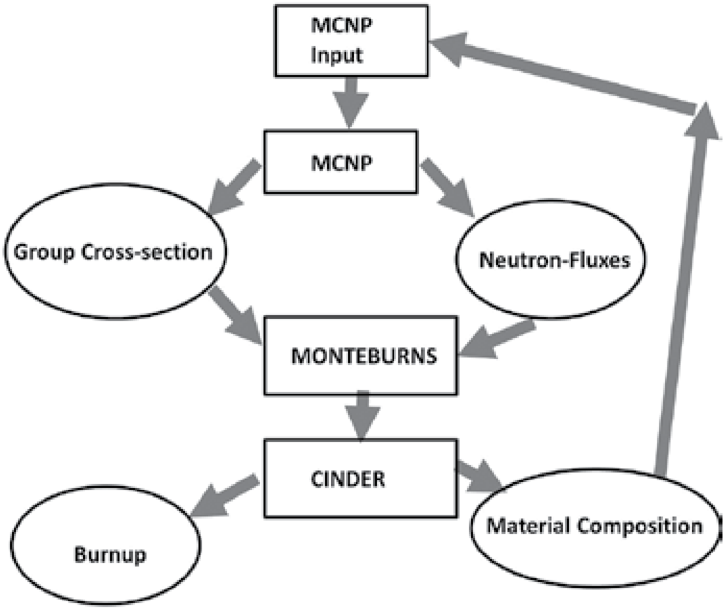

Figure 1. Simplified experimental model using MCNP and MONTEBURNS.

The inventory of important nuclides would then be analyzed with burnup time for each fuel. This would be done by burning the fuel in the reactor core for 220 days using a 30-day time step. A 10-day time step is allowed for core maintenance operations. The performance of each fuel grade on the effective multiplicative factor, reactivity and reactor core life would also be analyzed based on the inventory of radionuclides for each fuel grade. The three fuel grades would also be compared based on reactor neutronic parameters such as the reactivity and neutron fluxes. Finally, the total radioactivity of the reactor core would be analyzed using different fuel grades. This would be the key in estimating the radiological hazard at the end of the core life of the reactor.

2.3. The lattice cell structure

Nuclear reactor cores are constructed as either rectangular or hexagonal lattices of assemblies. The lattice structure could consist of several different shapes or identical shapes. The lattice assembly consists of the fuel, control and instrumentation pins surrounded by water or other material that moderates neutron energy and carries away the heat generated as a result of the fission process. The basic shapes which make up the lattice are known as unit cells or pin cells [10].

Various types of assemblies are then arranged in a lattice structure to form the reactor core. The two most common lattice structures used for nuclear reactor cores are the rectangular lattice, used in water cooled reactors, or a hexagonal lattice, more common in sodium-and-gas-cooled reactors. The lattice geometry is described by three main parameters: the unit cell shape;

the distance between the centers of adjacent unit cells, referred to as the lattice pitch; and the lattice dimension, which is a measure of how many units form the lattice.

The rectangular lattice for water-cooled reactors is used in this research. The lattice geometry is set up using the lattice fill matrix of the MCNPX visual editor. The total number of unit cells is hence NxNy. The lattice cell is shown below:

$$\begin{array}{l} 3\ 0\ 8\ \ -7\ 10\ \ -9\ \ \mathrm{U} = 1\ \mathrm{lat} = 1 \\ \mathrm{fill} =\ \ -24:24\ -24:24\ -0:0 \end{array}$$

The first number is the cell number, which is 3. The second number 0 is the material number indicating a void material. The next four numbers are the surface numbers of the planes which are the sides of the rectangular shape. The U card specifies the universe to which the cell belongs, which in this case is 1. A cell is filled with a universe which is either a lattice or an arbitrary collection of cells. There are 24 unit cells on either side of the center lattice element in the x and y direction as indicated by the fill card with no unit cells in the z direction. **Figure 2** shows the lattice geometry together with the cell and surface numbers as can be seen when using the MCNPX visual editor. This shows the position of cells and surfaces in the reactor core lattice and how they are related in the system geometry.

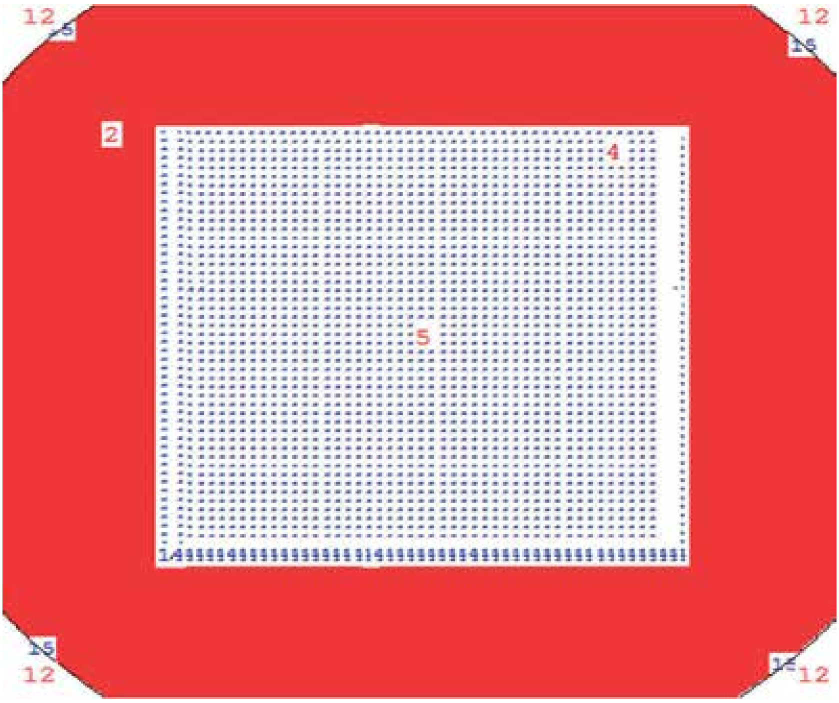

Figure 2. MCNPX simplified geometry showing both cell and surface numbers.

2.4. The critical reactor core system

A critical reactor system usually has an effective multiplication factor of 1. This usually means that the neutron production in one generation is equal to the neutron lost through either absorption or leakage in the preceding generation. While the sub-critical reactor might need an external neutron supply through accelerator-driven systems, the critical reactor system is self-sustaining. Usually, the size of the fuel cylinder and the density are much smaller for critical systems. The geometry of the critical pressurized water reactor system is modeled using the MCNPX visual editor. The material composition of the reactor core showing nuclide atom fractions for the three fuel grades and also for the clad material and moderator used is shown in **Table 1**.

Material name	Nuclide atom fraction
UO_2	^{16}O 5.85402 × 10^{-3}; ^{235}U 3.862438 × 10^{-2} ^{238}U 0.9555216
Commercially enriched uranium	^{234}U 3 × 10^{-4}; ^{235}U 2.96 × 10^{-2}; ^{238}U9.701 × 10^{-1}
Mixed oxide fuel	^{16}O 5.88402 × 10^{-3}; ^{235}U 2.5 × 10^{-3}; ^{238}U 0.9386; ^{238}Pu 1.1147 × 10^{-4}; ^{239}Pu 4.150 × 10^{-2}; ^{240}Pu 7.9657 × 10^{-4}; ^{241}Pu 1.001 × 10^{-2}; ^{242}Pu 5.6388 × 10^{-4}
Cladding (zirconium alloy)	^{50}Cr 9.98 × 10^{-4}; Fe 1.499 × 10^{-3}; Zr 0.982499; ^{112}Sn 0.014999
Moderator (light water)	^{1}H 4.7716 × 10^{-2}; ^{16}O 2.3858 × 10^{-2}; ^{10}B 3.6346 × 10^{-6}; ^{11}B 1.6226 × 10^{-5}

Table 1. Material composition of reactor core.

2.5. Normalization of tally plots

The tally plots are used to specify what needs to be investigated from the MCNP calculations. There are seven standard tallies available for use in MCNP. These tally cards are specified by Fn cards, where n specifies the tally number. SD cards are also used together with tally cards where necessary. The SD card is used to input a constant (a new area or volume) to divide the tally in cases where MCNP cannot calculate the area or volume for the regions. In all, three tally cards are used in this simulation. These are the f2, f4 and f7 tally cards. These were used to find out the flux across a surface, the track length in a cell and the track length estimate of fission energy deposition, respectively. The flux actually gives an idea of the flow of a physical property with time variation. The unit is given as quantity/(area × time). Some very important deductions were made from the flux calculations.

The tally bin width is usually normalized by dividing by the energy bin width. This gives a much broader representation of the particle distribution with energy. When a logarithmic scale is used for both axes, the visual representation is further obscured, with the tallies seen to decrease gradually with increasing energy or spread wide across the entire plot area. The two methods for normalizing energy-dependent tally are divided by the width of each energy bin or dividing by the logarithmic width of each energy bin [11].

The logarithmic width of the energy bin is referred to as the lethargy width. The governing equations are as follows (Eq. 1) [11]:

$$T_i = \int_{\mathrm{Elt}}^{E_{ut}} f(E)\,dE \tag{1}$$

where $E_{ut}$and E_{lt} are the upper and lower energy bin width, and *f*(*E*) is the flux or reaction rate. The tallies (T_i) tend to be small for small energy bins and large for large energy bins as can be seen from the above equation.

The normalized energy-dependent tally is calculated by dividing by the width of the energy bin and is shown below (Eq. 2):

$$I(E) = \int_{E_{lt}}^{\mathrm{Eut}} \frac{f(E)\,dE}{\int_{E_{lt}}^{E_{ut}} dt} = \frac{T_i}{E_{ut} - E_{lt}} \text{ (tally units)/unit energy} \tag{2}$$

For lethargy normed tallies, a definition is required for lethargy. Neutron lethargy is defined in the analysis of nuclear reactors as the logarithmic energy loss of neutrons scattered elastically. Mathematically, this is defined as in Eq. 3:

$$U = \mathrm{In}\frac{E_0}{E} = \mathrm{In}(E_0 - E) \tag{3}$$

where U is the neutron lethargy.

The difference in the log of the energy bins is related to the neutron lethargy as follows (Eq. 4):

$$\mathrm{In}(E_{ut}) - \mathrm{In}(E_{lt}) = U_{lt} - U_{ut} \tag{4}$$

where U_{lt} is the lethargy at E_{lt} and U_{ut} is the lethargy at E_{ut}. The lethargy normed value (FI) is then given by the relation (Eq. 5):

$$F_i(U) = \frac{T_i}{\mathrm{In}(E_{ut} - E_{lt})} = \frac{T_i}{U_{lt} - U_{ut}} \text{(tally units)/(unit lethargy)} \tag{5}$$

2.6. Setting up a criticality problem

The criticality calculation generally gives an idea about the ability of the reactor core to maintain a self-sustaining nuclear chain reaction. This is represented by the value of the effective multiplication factor, K_{eff}. For reactors, which are infinitely large, an infinite multiplication factor represents the criticality because it assumes that no neutrons leak out of the reactor. For a complete description of the life cycle of a real finite reactor, it is necessary to account for the neutrons that leak out. The effective multiplication factor takes this into account. Mathematically, K_{eff} is defined as follows (Eq. 6):

$$\mathrm{K}_{\text{eff}} = \frac{\text{neutron production from fission in one generation}}{\text{neutron absorbed} + \text{neutron leakage in preceding generation}} \tag{6}$$

The calculation of K_{eff} consists of estimating the mean number of fission neutrons produced in one generation per fission neutron started. The K_{eff} cycle is thus the computational equivalent of a fission generation, where a cycle is used to denote the computed estimate of an actual fission generation. MCNPX uses three different estimates to set up K_{eff} (absorption, collision and track length) estimate. The final result is the statistically combined result for the three estimates.

The KCODE card is used together with a number of cards to set up a criticality problem. These cards specify the initial spatial distribution of fission points and include the KSRC card, SDEF card and SRCTP card. The KSRC card sets the initial x, y, z locations of fission points. The SDEF card is used to define points uniformly in volume whilst the SRCTP card is defined from a previous MCNPX criticality calculation. A typical KCODE card used together with a KSRC card has the following format:

KCODE: 10000 1.000000 70 150 KSRC: 0.0000 0.0000 0.0000

The card above indicates that the nominal number of source histories is 10000 with the initial K_{eff} guess kept as 1.00. The number of inactive cycles skipped before active K_{eff} accumulation is 70 and the total number of cycles that run in the problem is 150. The KSRC card indicates that the x, y, z locations for initial fission source points were taken from the origin. The criticality calculations were performed with help from Bunde Kermit at the U.S Department of Energy.

In this research, different fuel grades and different cladding materials were used for the same reactor core configuration to investigate the effect of these on the criticality. The different fuel grades used were MOX, UOX and CEU. The materials used for cladding include zirconium, zircaloy and stainless steel. Successive fission cycles were run for determination of the criticality. **Table 2** shows the neutron absorption cross-sections and thermal conductivities for different clad materials at 25°C [12].

	Cr	Si	Mn	Fe	Ni	Mo	B	Sn	Zr	Zr-alloy	Steel
σ_a (barns)	3.1	0.17	13.3	2.56	4.49	2.6	750	0.63	0.184	0.22	3.1
k($Wm^{-1}K^{-1}$)	93.9	149.2	7.81	79.5	90.9	138	27.4	66.8	22.6	21.5	16

Table 2. Neutron absorption cross-sections and thermal conductivities for common clad materials at 25°C.

3. Results and discussion

3.1. Criticality calculation

The neutron absorption cross-sections show the ease with which a material absorbs thermal neutrons generated from fission in the reactor core. The lower the neutron absorption cross-section, the less permeable a material is to thermal neutrons. The thermal conductivity also shows how efficient a material is in conducting heat. Materials with higher thermal conductivities are more efficient conductors of heat than those with low thermal conductivities. **Table 3** shows K_{eff} values at the beginning and end of core life (BOL and EOL) as well as the corresponding standard deviations. The K_{eff} value used here is a result of the statistical combination of the three different estimates used by MCNP (absorption, collision and scattering). The major control cards used were the KCODE and the KSRC card.

From the neutron absorption cross-section in **Table 2**, the thermal neutron absorption of zirconium and zircaloy are much lower than that of stainless steel. This explains the good K_{eff} value obtained for zircaloy and zirconium clad fuels as compared to that of stainless steel. The absorptivity also explains the degree of neutron interaction with the clad material. For zirconium and zircaloy, little neutron is absorbed and hence these neutrons remain in the reactor core and are able to initiate further fission processes. This also makes zirconium very effective in preventing radioactive fission fragments from escaping the fuel into the coolant and contaminating it. Again, when UOX and CEU fuel grade materials were used, similar patterns of K_{eff} were obtained with zirconium and zircaloy showing greater results for K_{eff} as compared to stainless steel. Even though zirconium has a slightly lower neutron absorption cross-section and comparable thermal conductivity relative to zirconium alloy as shown in **Table 2**, K_{eff} results for zircaloy look slightly higher than that of zirconium. This observation may be due to enhanced alloy properties.

The zircaloy cladding used is zircaloy-4, which is similar in composition to zircaloy-2, but has reduced nickel and iron compositions. The reaction of zirconium with steam at high temperatures produces hydrogen gas by the reaction (Eq. 7):

$$\mathrm{Zr} + 2\mathrm{H_2O} \rightarrow \mathrm{ZrO_2} + 2\mathrm{H_2} \tag{7}$$

FUEL	CLAD	K_{eff} at BOL	K_{eff} at EOL
MOX	Stainless steel	1.09295 ± 0.00120	0.92315 ± 0.00087
	Zircaloy	1.15778 ± 0.00145	0.98630 ± 0.00098
	Zirconium	1.15624 ± 0.00129	0.98258 ± 0.00098
UOX	Stainless steel	0.90130 ± 0.00193	0.81205 ± 0.00212
	Zircaloy	0.95456 ± 0.00140	0.80834 ± 0.00077
	Zirconium	0.93740 ± 0.00236	0.80754 ± 0.00049

FUEL	CLAD	K_{eff} at BOL	K_{eff} at EOL
CEU	Stainless steel	0.91187 ± 0.00311	0.80920 ± 0.00097
	Zircaloy	0.97923 ± 0.00210	0.86789 ± 0.00105
	Zirconium	0.95529 ± 0.00232	0.84828 ± 0.00054

Table 3. K_{eff} values for different clad materials at the beginning and end of burnup steps for MOX, UOX and CEU fuel.

Oxidation of zirconium metal reduces the ductility and robustness of zirconium metal, and hence increases the probability for the escape of thermal neutrons from the core of the reactor [12]. This further reduces the effectiveness of zirconium for higher and prolonged fuel burnups. With respect to zirconium alloys, the hydrogen produced by oxidation of zirconium in steam diffuses into the alloy, causing the formation of zirconium hydrides. The hydrides formed are less dense and more brittle than the zirconium alloy and leads to the weakening of the clad material. This is especially the case in zirconium-2 alloy. The zirconium-4 alloy has a reduced composition of iron and no nickel composition; this reduces the hydride effect by reducing the tendency to pick up hydrogen. This characteristic of zircaloy-4 used improves its mechanical properties, reducing the probability of escape of thermal neutrons considerably, thus improving the overall K_{eff} value in the long term.

The thermal conductivities listed in **Table 2** reveal a higher value for zirconium and zircaloy, as compared to that of stainless steel. A high value means that heat can be quickly conducted away from the reactor core to the coolant. This prevents very high temperature buildup in the core leading to the melting of the fuel material or clad. The thermal conductivity of zirconium alloys, with thermal expansivity of nearly one-third that of stainless steel, is superior compared to that of stainless steel and other nuclear fuel storage materials. This also gives zirconium alloys superior dimensional stability at elevated temperatures. MCNP offers a number of statistical checks to assess the validity of a criticality calculation, which can be found in the MCNP user's manual [11]. These were found to be in good agreement with the output file when cross-checked.

3.2. Nuclear fuel reactivity

Reactivity is the degree of neutron multiplication in the reactor core. This parameter is directly related to the tendency of the reactor core to change power level. Also, control rods can be used to obtain a desired power level change or keep the power level constant by adjusting the reactivity when raised or lowered into the reactor core. Other factors which affect the reactivity include the density and temperature of the coolant or moderator and also the fuel temperature and density.

The reactivity for the three different fuel grades is calculated as a function of burnup, and the peak reactivity determined for each fuel grade is shown in **Table 4**. The reactivity is evaluated as (Eq. 8):

$$\rho = \frac{k-1}{k} \tag{8}$$

where k is the effective multiplication factor and ρ is the reactivity.

The peak reactivity is the highest reactivity obtained as a function of burnup for each fuel grade. Another parameter, the gain, is the difference between the peak reactivity and the reactivity at BOL [13]. The gain is usually used in breeding reactors to characterize the affinity of the nuclear fuel for breeding reactivity. The gain is useful in breeder reactors to measure the fuels affinity to breed 239Pu; however, it is not a very good parameter for determining the neutronics performance of the fuel. One of the most important measures of fuel performance is the peak reactivity. Since the reactivity has a direct bearing on the power level, the higher the peak reactivity, the much higher the power output. The peak and gain reactivities of the three different fuel grades as burnup proceeds are indicated in **Table 4**. Usually, fuels with higher peak reactivities are found to have much lower gain. UOX has much higher peak reactivity, but records the lowest gain in reactivity.

Reactivity	UOX	MOX	CEU
PEAK	0.270	0.142	0.155
GAIN	0.119	0.124	0.142

Table 4. Reactivity parameters for the different fuel grades.

MOX has a much lower peak value relative to UOX, but records a much higher gain in reactivity. The same is seen for CEU. A look at the compositions of the three fuel grades reveals that 235U forms the main fissile material in both UOX and CEU. Depletion of 235U is known to reduce the reactivity. The buildup of actinides due to neutron absorption of 238U is also known to reduce the reactivity. These two factors occur in both UOX and CEU and might cause loss of reactivity, but this is compensated by the buildup of 239Pu and 241Pu in these two fuels. However, in MOX fuel, added to the depletion of 235U and 238U which reduces the reactivity, the reactivity is further reduced by the depletion of 239Pu and 241Pu, which are the main fissile materials in MOX fuel. This is seen in the relatively low peak value recorded for MOX fuel.

3.3. Burnup calculations

An expected core lifetime of 220 days is used for the reactor core since the K_{eff} drops drastically after this period, hence reducing the criticality. Usually, using large time steps of 50 and above leads to encountering large flux shape change and may lead to inaccurate results. Time steps small enough to capture the flux-shape change accurately over time is necessary according to Pelowitz [14]. Again, the time step chosen for a particular reaction depends on the core lifetime of the reactor with larger core lifetimes having larger time steps. Khattab et al. [7] used a 20-day time step for a 200 days expected operating life time of an MNSR. The 10-day period (between 60 and 70 days) was chosen to allow for maintenance operations. No burnup is carried out within this period and the fuel may decay within this period from the heat built up in the core. The 10-day time step was chosen from examples used in the MCNPX user's manual [14].

In all, the uranium nuclide inventory shows similar variation with burnup time for all three different fuel grades. There is a rapid decrease of 235U and a slightly lower decrease for 238U in burnup time because these radionuclides are consumed as the fission process progresses. 236U radioisotopes, which are not fissile with thermal neutrons and are generated mainly due to gamma radiation emission of 235U as fission proceeds, are observed to increase with burnup time for each of the three fuel grades. Very little of 238U is consumed in the fission process as this is only fissionable and the main fissile material is 235U, which decreases rapidly. The uranium inventory is found to decrease for MOX fuel, but on a slightly lower scale relative to the other fuel grades due to relatively little uranium composition used in its fabrication. Our study shows that the 240Pu isotope is observed to buildup steadily for each of the three fuel grades. The 240Pu radioisotope, however, rises on a much higher scale in MOX than in CEU and UOX. This is because 240Pu is formed in a nuclear reactor by occasional neutron capture by 239Pu, much of which forms the initial fissile fuel material in MOX fuel.

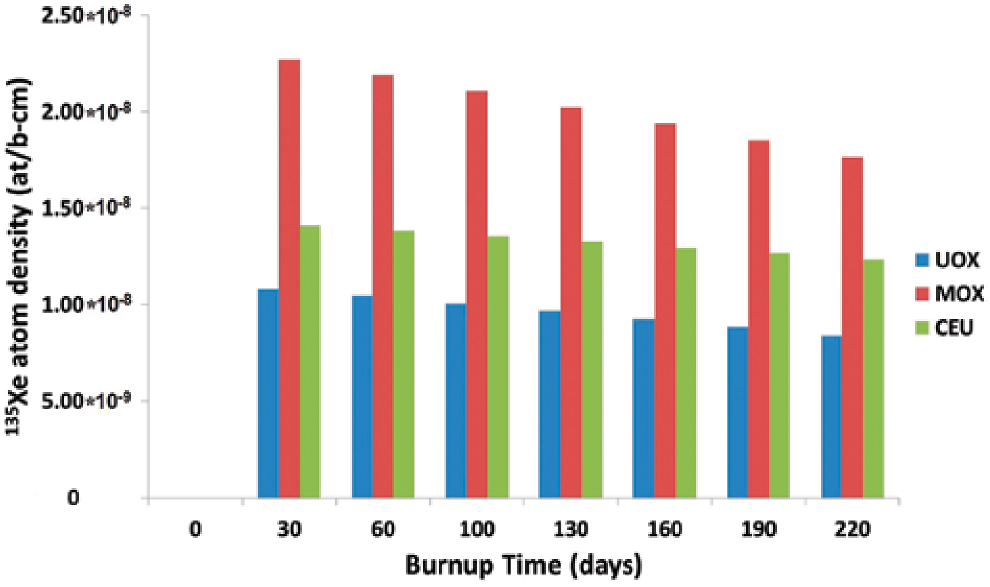

Figure 3. Atom density of 135Xe as a function of burnup time.

For 135Xe in **Figure 3**, a similar pattern is observed for all three fuel grades. There is a rapid accumulation of 135Xe after the first burn step, a result which might lead to a drastic drop in K_{eff}. This is known as the xenon poisoning. The production of 135Xe isotopes after this burn step gradually decreases, a result which helps to regulate the reactivity of the system. The accumulation of the fission product 135Cs shows a linear variation with the burnup time for all three fuel grades as seen in **Figure 4**.

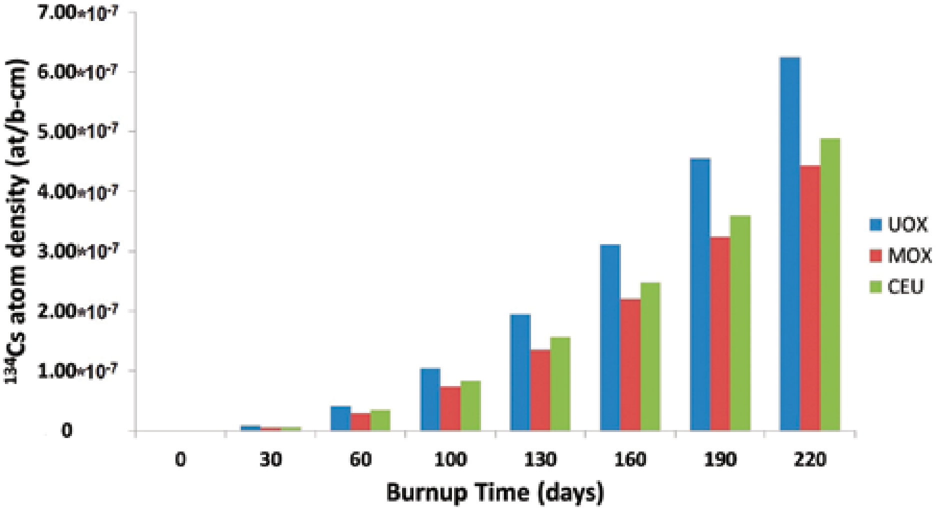

Figure 4. Atom density of 134Cs as a function of burnup time.

3.4. Time evolution of the K_{eff}

The study of the variation of K_{eff} with core burnup is of much importance as it describes whether or not the chain reaction in a nuclear reactor is stable or self-sustained. The results also give very important details on the core lifetime, defined as the length of time the reactor effective multiplication factor is above one. There is a large drop in K_{eff} during the first burn step as shown in **Figure 5**. This drop can be attributed to a drastic reduction in reactivity due primarily to the buildup of burnable poisons such as 135Xe and the depletion of fresh fuel. The K_{eff} is then gradually seen to decrease.

A similar pattern of the variation of K_{eff} with time is observed in all three different fuel grades. MOX fuel, however, might be much more effective in improving the core lifetime of the reactor, as K_{eff} is observed to remain critical for a much longer time relative to the other fuels. For UOX and CEU to maintain criticality for longer burn days, an increase in the mass fractions or weight percent (particularly for the fissile isotopes) is required. This is not too desirable due to the extremely high cost involved.

Hermine et al. [15] conducted research on the variation of K_{eff} with burnup time using AP1000 and a very high temperature reactor (VHTR) fuel cycle. Transuranic fuel arising from the AP1000 reactor was used as a part of fuel-loading of the VHTR. Transuranic fuels are fuels in which conventional uranium fuels have been mixed with a transuranic element (elements with atomic number greater than 92) in the form of mainly plutonium. A transuranic fuel containing 40% of weapons-grade plutonium (WGPu) was found as the best compromise [15]. A drastic first drop in K_{eff} occurred due to the depletion of burnable poisons, which is also observed in this study. The reactor life was extended by at least 36.7% when part of the low enriched uranium (LEU) is replaced by TRU, a result which agrees with the ability of TRU fuel to remain critical for a much longer time.

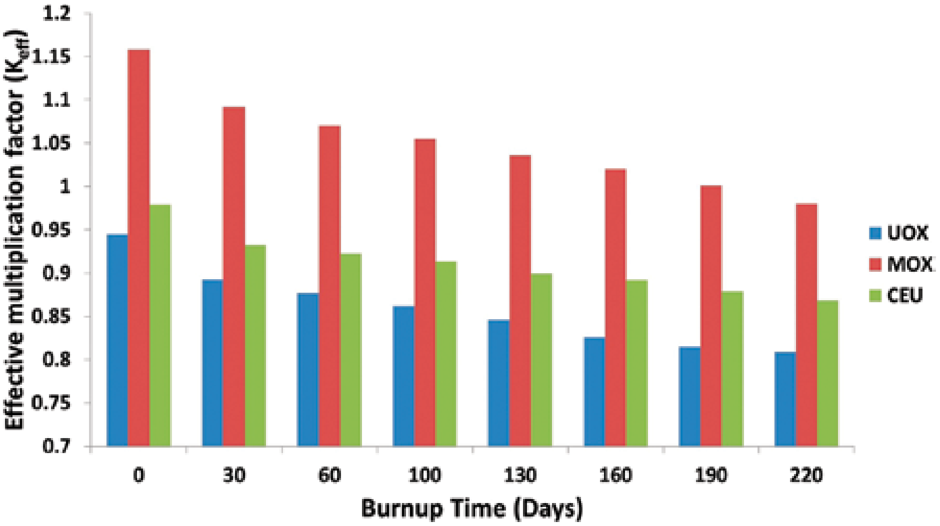

Figure 5. K_{eff} of different fuel grades as a function of burnup time.

The atom densities and radioactivities in Bequerel were calculated for each of the three fuel grades at the end of the 220-day burnup. The total radioactivities of both actinides and non-actinides were calculated for each fuel grade as shown in **Table 5**. In the event of a severe reactor core accident, the radiological hazard posed is proportional to the concentrations and radioactivities of these radionuclides. The total atom densities and radioactivities are also very important parameters in estimating which fuel grade performs better, posing a relatively less hazard at the end of the burnup time or core lifetime of the reactor. For the same burnup time, MOX fuel is found to have a relatively less total radioactivity of the reactor core, almost 15% reduction as compared to the other fuel grades.

The results from the burnup simulations were compared with some results obtained from literature to assess the validity. Yan Cao et al. [6] performed burnup simulations using the MCNPX code for a PWR with 3.15% enriched UO2 fuel. The uranium isotope depletion, increase in fissile plutonium isotope and that of 241Pu and 242Pu in that simulation are in good agreement with the results obtained from this study. Also, in assessing the accuracy of a new Monte Carlo based burnup code, burnup simulations were performed for a VVER-1000 assembly using UO2 and UO2GDO3 nuclear fuel types [5]. Again, the plot of atom densities of key radionuclides with burnup time showed good agreement with the results obtained from this study. Khattab et al. calculated the total radioactivity for a 220-day burnup period of a miniature neutron source reactor using the GETERA code. The total radioactivity at the end of the reactor core was calculated based on 19 selected radionuclides, which were considered essential to potential radiological hazard associated with the severe reactor accident in the MNSR core. This value was found to be 9.462×10^{13} Bq [7]. This study calculated the total radioactivities of the reactor core based on all radioactive actinides and non-actinides present at the end of the reactor core life as shown in **Table 5**. Comparison of the values shows reasonable agreement.

FUEL	Actinide activity (Bq)	Non-actinide activity (Bq)	Total activity (Bq)
UOX	1.6507×10^{19}	2.6011×10^{19}	4.25167×10^{19}
MOX	1.04663×10^{19}	2.59259×10^{19}	3.63859×10^{19}
CEU	1.94102×10^{19}	2.62367×10^{19}	4.56739×10^{19}

Table 5. Total activities of actinides and non-actinides after core burnup.

3.5. System Burnup and Neutronics Data

The burnup is given in units of gigawatt days (GWD) per metric tons of uranium (MTU), where MTU is the sum of the masses of isotopes with protons ≥90. The nuclear fission rate (f) is calculated from the product of the macroscopic fission cross-section ($\sum f$) and the neutron flux (). The power density (p) is determined as the product of the nuclear fission rate and the energy per fission (w). The average neutron flux is thus directly proportional to the power level in the reactor. As fuel consumption takes place with time, the neutron flux also increases, since the power is also directly related to the fuel content.

A look at the neutron fluxes of all three fuel grades reveals a general increase with time as seen in **Tables 5–7**, with UOX having a slightly higher average flux relative to CEU and MOX. The neutron flux increased by 20% for UOX fuel compared to a 17% increase in MOX fuel. The flux for UOX fuel at the end of burnup exceeds that of CEU by 17.87% and MOX by 22.68% with that of CEU exceeding MOX by 6%. This characteristic of UOX which may be due to its high fissile material density enhances the system power level. Again, these results agree with the peak reactivity parameter results in **Table 4** in which UOX and CEU had much higher reactivity relative to MOX. The burnup values indicate the fission energy released per metric ton of uranium. MOX fuel indicates comparable, but slightly higher, values of fuel burnup relative to UOX as shown in **Tables 6** and **7**. The burnup value at the end of the burn step for MOX exceeds that of CEU by 44% and UOX by 23%. This is due to the fact that MOX fuel remains much critical for a high part of the burnup period relative to the other two. **Table 8** shows CEU fuel with much lower fuel burnup values relative to the other two fuels, which may be due to its lower fissile material density.

Step	Time (days)	Flux (n/cm^2-s)	Burnup (GWD/MTU)
0	0	2.31×10^{14}	0
1	30	2.44×10^{14}	2.01
2	60	2.50×10^{14}	4.01
3	70	0	4.01
4	100	2.57×10^{14}	6.02
5	130	2.65×10^{14}	8.02
6	160	2.72×10^{14}	1.00

Step	Time (days)	Flux (n/cm^2-s)	Burnup (GWD/MTU)
7	190	2.81×10^{14}	12.00
8	220	2.91×10^{14}	14.00

Table 6. Neutronics and burnup data for UOX fuel.

Step	Time (days)	Flux (n/cm^2-s)	Burnup (GWD/MTU)
0	0	1.85×10^{14}	0
1	30	1.96×10^{14}	2.05
2	60	2.00×10^{14}	4.11
3	70	0	4.11
4	100	2.05×10^{14}	6.16
5	130	2.09×10^{14}	8.21
6	160	2.14×10^{14}	1.03
7	190	2.19×10^{14}	1.23
8	220	2.25×10^{14}	1.44

Table 7. Neutronics and burnup data for MOX fuel.

Step	Time (days)	Flux (n/cm^2-s)	Burnup (GWD/MTU)
0	0	2.06×10^{14}	0
1	30	2.17×10^{14}	1.16
2	60	2.20×10^{14}	2.32
3	70	0	2.32
4	100	2.23×10^{14}	3.47
5	130	2.26×10^{14}	4.63
6	160	2.31×10^{14}	5.79
7	190	2.35×10^{14}	6.95
8	220	2.40×10^{14}	8.10

Table 8. Neutronics and burnup data for CEU fuel.

4. Conclusions

Parallel computing of fuel burnup in nuclear reactors give important insight about the chain reaction, the fuel consumption and buildup of radionuclides. The comprehensive calculations clearly present the characterization of the neutron flux, which is essential in the reactor design.

http://dx.doi.org/10.5772/62572

Fuel burnup is one of the most important reactor core parameters in the operation of nuclear reactors as well as any fuel research program. In this research, Monte Carlo burnup simulations of a critical pressurized water reactor system were carried out using three different fuel grades: MOX, UOX and CEU. The effect of different clad materials on K_{eff} was also analyzed.

The study of reactor neutronic parameters showed UOX fuel performs better relative to MOX and CEU. The peak reactivity of UOX was found to be 0.270 compared to 0.142 and 0.155 for MOX and CEU fuel, respectively. Also, the neutron flux for UOX exceeds that of CEU and MOX by 17.87 and 22.68%, respectively.

Zircaloy, with low thermal neutron absorption cross-section and high thermal conductivity produced better results for K_{eff} and hence proves to be a much more effective clad material.

The atom densities and radioactivities in Bequerel were calculated for each of the three fuel grades at the end of the 220-day burnup. The total atom densities and radioactivities of both actinides and non-actinides were calculated for each fuel grade. This was found to be 4.251e19Bq for UOX fuel and 3.639e19Bq and 4.567e19Bq for MOX and CEU fuel, respectively. In the event of a severe reactor accident, the radiological hazard posed is proportional to the concentrations and radioactivities of these radionuclides. The total atom densities and radioactivities are also very important parameters in estimating which fuel grade performs better in the sense of posing relatively few hazards at the end of the burnup time or core lifetime of the reactor. For the same burnup time, MOX fuel was found to have a relatively less total radioactivity of the reactor core, almost 15% reduction as compared to the other fuel grades.

Acknowledgements

This work is supported by the National Science Foundation (NSF) through the Center for Energy and Environmental Sustainability (CEES), a NSF CREST Center (Award NO. 1036593).

Author details

Raghava R. Kommalapati[1*], Fiifi Asah-Opoku[2], Hongbo Du[3] and Ziaul Huque[4]

*Address all correspondence to: rrkommalapati@pvamu.edu

1 Center for Energy & Environmental Sustainability and Department of Civil and
Environmental Engineering, Prairie View A&M University, Prairie View, TX, USA

2 Center for Energy & Environmental Sustainability, Prairie View A&M University, Prairie View, TX, USA

3 Center for Energy & Environmental Sustainability, Prairie View A&M University, Prairie View, TX, USA

4 Department of Mechanical Engineering, and Center for Energy & Environmental Sustainability Prairie View A&M University, Prairie View, TX, USA

References

[1] Kim C.-S.; Kim C.-K.; Martin P.; Sansone U., Determination of Pu isotope concentrations and isotope ratio by inductively coupled plasma mass spectrometry: a review of analytical methodology. Journal of Analytical Atomic Spectrometry 2007, 22 (7), 827–841. DOI: 10.1039/b617568f.

[2] Alonso J.I.G.; Sena F.; Arbore P.; Betti M.; Koch L., Determination of fission products and actinides in spent nuclear fuels by isotope dilution ion chromatography inductively coupled plasma mass spectrometry. Journal of Analytical Atomic Spectrometry 1995, 10, 13. DOI: 10.1039/JA9951000381.

[3] Nicolaou G., Provenance of unknown plutonium material. Journal of Environmental Radioactivity 2008, 99 (10), 1708–1710. DOI: 10.1016/j.jenvrad.2008.06.001.

[4] Joe K.; Jeon Y.-S.; Han S.-H.; Lee C.-H.; Ha Y.-K.; Song K., Determination of plutonium content in high burnup pressurized water reactor fuel samples and its use for isotope correlations for isotopic composition of plutonium. Applied Radiation and Isotopes 2012, 70 (6), 931–936. DOI: 10.1016/j.apradiso.2012.03.015.

[5] El Bakkari B.; ElBardouni T.; Nacir B.; ElYounoussi C.; Boulaich Y.; Meroun O.; Zoubair M.; Chakir E., Accuracy assessment of a new Monte Carlo based burnup computer code. Annals of Nuclear Energy 2012, 45, 29–36. DOI: 10.1016/j.anucene.2012.02.011.

[6] Cao Y.; Gohar Y.; Broeders C.H.M., MCNPX Monte Carlo burnup simulations of the isotope correlation experiments in the NPP Obrigheim. Annals of Nuclear Energy 2010, 37 (10), 1321–1328. DOI: 10.1016/j.anucene.2010.05.015.

[7] Khattab K.; Dawahra S., Calculation of fuel burnup and radionuclide inventory in the Syrian miniature neutron source reactor using the GETERA code. Annals of Nuclear Energy 2011, 38 (6), 1442–1446. DOI: 10.1016/j.anucene.2011.01.030.

[8] Chadwick M.B.; Young P.G.; Chiba S.; Frankle S.C.; Hale G.M.; Hughes H.G.; et al. Cross-section evaluations to 150 MeV for accelerator-driven systems and implementation in MCNPX. Nuclear Science and Engineering 1999, 131 (3), 293–328. DOI: 10.13182/NSE98-48.

[9] Filges D.; Goldenbaum F.; Enke M.; Galin J.; Herbach C.M.; Hilscher D.; et al. Spallation neutron production and the current intra-nuclear cascade and transport codes. European Physical Journal A. 2001, 11 (4), 467–490. DOI: 10.1007/s100500170058.

[10] U.S. Nuclear Regulatory Commission, "Fault Tree Handbook", NUREG-0492. Available from: http://www.nrc.gov/reading-rm/doc-collections/nuregs/staff/sr0492/ [Accessed 15 December 2015].

[11] Brown F.; Kiedrowski B.; Bull J., "MCNP 1.60 release notes", Los Alamos National Laboratory, LA-UR-10-06235. 2008. Available from: https://laws.lanl.gov/vhosts/mcnp.lanl.gov/pdf_files/la-ur-10-06235.pdf [Accessed 20 December 2015].

[12] Asah-Opoku F.; Liang Z.; Huque Z.; Kommalapati R.R., Burnup simulations of different fuel grades using the MCNPX Monte Carlo Code. Nuclear Technology & Radiation Protection 2014, 29 (4), 259–267. DOI: 10.2298/ntrp1404259a.

[13] Yarsky P. Core design and reactor physics of a breed and burn gas-cooled fast reactor [Thesis], 2005. Pages 74–76, Massachusetts Institute of Technology. Cambridge, MA, USA.

[14] Pelowitz D.B., MCNPX user's manual version 2.7.0. LA-CP-11-00438. Los Alamos National Laboratory. 2011.

[15] Cuvelier M.-H.M.; Tsvetkov P.V., TRU management and U-235 consumption minimization in fuel cycle scenarios with AP1000 and VHTRs. Annals of Nuclear Energy 2013, 55, 137–150. DOI: 10.1016/j.anucene.2012.11.015.

Chapter 4

Oxidation, Embrittlement, and Growth of TREAT Zircaloy-3 Cladding

Charles W. Solbrig, Anthony LaPorta,
Katelyn M. Wachs and James R. Parry

Additional information is available at the end of the chapter

http://dx.doi.org/10.5772/62708

Abstract

This chapter analyzes the effects of oxidation, embrittlement, and cladding growth on the Zircaloy-3 alloy used for 25 mil thick TREAT fuel assembly cladding. The fuel cladding is a protective shell which is used to prevent damage to the enclosed fuel. Therefore, its integrity is important to guarantee this protection. The above three factors which can affect the Zircaloy-3 cladding are considered in this chapter and investigated. Limits to operation are determined. The oxidation of Zircaloy-3 in air is of interest to air-cooled reactors and Zircaloy-2 and 4 for accidents in fuel storage pools. The temperature range of interest is from room temperature where the fuel is stored for long periods of time, through the temperature range encountered in normal operation (400 to 600°C) to the highest temperatures which are possible in extreme accident situations. This temperature range is considered in this chapter to be from room temperature to 1200°C.

Keywords: cladding, zircaloy, oxidation, embrittlement, metal growth

1. Introduction

This chapter describes the corrosion rate of Zirconium-2, 3, and 4 in air. Zircaloy-2 and 4 are used to clad fuel for all commercial power reactors. The Kendall Zircaloy-2 oxidation correlation is derived based on the well-known physically justified Arrhenius equation using legacy rate data at 500, 600, and 700°C. Additional data obtained by several other authors have shown that this correlation can be extended so that it adequately covers the range of 200 to 1100°C. This correlation also bounds the oxidation rate of Zircaloy-3, which is used to clad the fuel in the TREAT reactor. Zircaloy-4 rates are seen to be higher than the Zircaloy-2 correlation. Zircaloy-2 rates are higher than the Zircaloy-3 rates. The Zircaloy-2 correlation is verified for Zircaloy-3 by comparison to oxide thickness measurement on Zircaloy-3 coupons oxidized in air for different time periods in the temperature range of 500 to 1100°C: many coupons proceeded to disintegration. Although the latter samples still had a metal layer, oxygen incursion into the metal grain boundaries caused the metal to become brittle and crack like rust. The Kendall correlation is shown to adequately describe the behavior of these samples over the entire range 500 to 1100°C. Maximum oxide limit of 15.52 mils growth for TREAT cladding was determined from these data to ensure that the fuel assemblies could still be removed without disintegration.

The TREAT reactor, a graphite-moderated thermal reactor, is designed primarily for operation in the transient or pulsed mode for destructive testing of prototypic fast reactor fuel pins. It is designed conservatively to produce a pulse with a thermal neutron fluence of at least 3.5×10^{15} neutrons/cm^2 averaged over the core. The operating TREAT core temperature limit at the peak is 600°C.

The standard TREAT fuel assembly consists of upper and lower graphite reflector sections and a central section of uranium oxide-bearing graphite fuel. The fuel section is 4 ft long and contains six fuel blocks, each 8 in. long and 3.96 in. square with chamfered corners. The reactor fuel blocks consist of small particles (mean size, 10 microns) of fully enriched ^{235}U dispersed in a graphite-carbon matrix. The carbon-to-uranium U^{235} atom ratio is nominally 10,000:1. The graphite-carbon-urania blocks are sealed within evacuated Zircaloy-3 cans.

Zirconium alloys are used for cladding in all commercial power thermal reactors because of the high corrosion resistance, low cross section for thermal neutrons, and high temperature capability. As shown later in this chapter, Zircaloy-3 (Zr-3) is more corrosion resistant in air than either Zr-2 or Zr-4 and was used to clad the TREAT fuel. In low-temperature reactors such as TRIGAs, aluminum can be used. Since TREAT has a very thermalized spectrum, the low cross section and high temperature capability were the reasons Zr-3 was used.

The compositions of the common zirconium alloys are listed in **Table 1** (Gibbons [1], Blanchard [2] for Zr-2, Zr-4, and Alloy Digest [3] for Zr-3). Zr-3 has much less zinc than either Zr-2 or Zr-4.

Alloy	Zr	Sn	Fe	Cr	Ni	Nb	O	C	N	Hf
Zr-2	98.20	1.50	0.12	0.10	0.05	–	0.13	–	–	–
Zr-4	98.20	1.30	0.22	0.10	–	–	0.13	–	–	–
Zr-3	99.42–99.22	0.2–0.3	0.2–0.3	0.05	0.05	–	–	0.05	0.01	0.02

Table 1. Composition percentages of commercial Zirconium alloys (w/o).

A considerable amount of research has been carried out in investigating the oxidation of zirconium alloys used in different environments. The early research was carried out on Zircaloy-2 and the later work was carried out on Zircaloy-4. The recent oxidation research has been carried out because of concern about loss of cooling water from spent fuel pools where temperatures range from 300 to 600°C. Natesan [4] in 2004 conducted air oxidation tests on unirradiated Zircaloy-4 cladding starting with a 25 to 30 μm (1 mil) oxide layer representative of the current inventory of spent fuel discharged after a medium or high level of fuel burnup. Temperatures were in the range of 300–600°C, which is representative of cladding heat up in the event of a partial or full draining of spent fuel pool coolant. Ji Min Lee [5] in 2012 investigated the oxidation of Zircaloy-4 under transient conditions from 500 to 800°C. Duriez [6] in 2009 summarized results of several studies comparing them in terms of kinetics and oxide scale structure and composition. Steinbrück [7] in 2009 studied the mechanism of the reaction between Zircaloy-4 and air at temperatures from 800 to 1500°C. Both of these studies considered pre-oxidized metal. Beuzet [8] in 2009 used existing correlations to simulate the zirconia scale growth under air atmosphere in the MAAP4.07 Severe Accident code. Duriez [9] in 2008 studied the degradation of Zircaloy-4 and M5 cladding tubes in air at high temperature by thermo-gravimetric analysis, in isothermal conditions, from 600 to 1200°C. Steinbrück [10] in 2007 conducted experiments on the reaction between Zircaloy-4 and air under mixed air (nitrogen) steam atmospheres and pre-oxidation conditions for severe nuclear reactor accident temperatures 800–1500°C. The earlier Zircaloy-2 and 3 work is described in the next section.

2. Oxidation characteristics of Zircaloy-3 cladding

The temperature range which might be encountered for the evaluation of the effects of oxidation on the Zircaloy-3 cladding for the TREAT fuel is from room temperature, approximately 25°C, to 1200°C. Extremely unlikely accidents cause temperature to approach 1200°C. Normal reactor operation restricts the maximum temperature to 600°C. The design basis reactivity insertion accident must not cause the cladding to exceed an equilibrium temperature of 820°C. During typical reactor operations, the cladding is below 600°C in a transient and near room temperature the rest of the time. So, the corrosion which occurs in all these temperature range is of interest.

Oxidation rate data in air have been obtained on zirconium, Zircaloy-2, and Zircaloy-4. Limited rates have been measured for Zircaloy-3, but rates are lower than Zircaloy-2. Conservatively, the data obtained by Kendall [11] on Zircaloy-2 are used to represent the rates of Zircaloy-3. Zircaloy-4 rates are higher. The following discussion presents the characteristics of the oxidation of zirconium and the above alloys in the temperature range of interest (25 to 820°C).

2.1. Zirconium oxidation

Lustman [12] summarized the oxidation rates of zirconium in air, oxygen, and nitrogen. The reaction rate of zirconium is higher with air than with oxygen or nitrogen. Lustman explains this by postulating that nitrogen dissolves in ZrO_2; since nitrogen is quadrivalent, defects would be created in the oxygen ion lattice, thus permitting a higher rate of diffusion of oxygen through ZrO_2.

Phalnikar [13] studied the oxidation behavior of graphite-melted Bureau of Mines zirconium in air from 400 to 1200°C. Both oxygen and nitrogen enter into the reaction, and for temperatures below 1050°C an outer white or buff monoclinic scale of ZrO_2 forms in addition to an inner black scale of monoclinic and tetragonal ZrO_2, cubic ZrN, voids, and possibly dissolved nitrogen in the metal [12]. The outer white layer does not form immediately, but requires a definite time to nucleate. At 400°C, this time is 100 hours, whereas at 1300°C only 5 min is required [13]. The appearance of the white scale layer is an indication of an increased rate of reaction at low, but not at, high temperatures. A parabolic relation between weight gain and time occurs before the formation of the white outer scale.

The oxidation buildup is nearly linear with time on a log log plot, indicating a power relation between weight gain and time. The curves for 800°C and below all have a significant bend in them, indicating a change from a low reaction rate regime to a much higher one at later time. The change is referred to as the regime transition. The post-transition regime is a linear relation and the reaction rate is much higher than the pre-transition regime. Reactions at temperatures of 900°C and above do not exhibit this bend because of a change in the zirconium crystal structure from the alpha phase to the beta phase which occurs at 862°C [14].

2.2. Oxidation rates of Zircaloy-2

Kendall [11] measured the corrosion rates of sponge zirconium and Zircaloy-2 in dry air at 500, 600, and 700°C. Consistent with the previous discussion, he states that the reaction proceeds in two stages: initially the rate decreases with exposure time, approximating a cubic relationship. After sufficient time of exposure (after transition), the rate becomes a constant independent of time.

TREAT fuel was built in 1958 and its cladding oxidation rate estimates were based on the alloy research of Kendall [11]. Kendall measured the reaction rates on many different samples for different air flow rates, metal geometries, cold working, annealing, and at three different temperatures, 500, 600, and 700°C. He concluded temperature and metal composition are the important parameters which determine the reaction rate. **Figure 1** illustrates the uncertainty in the measurements [11].

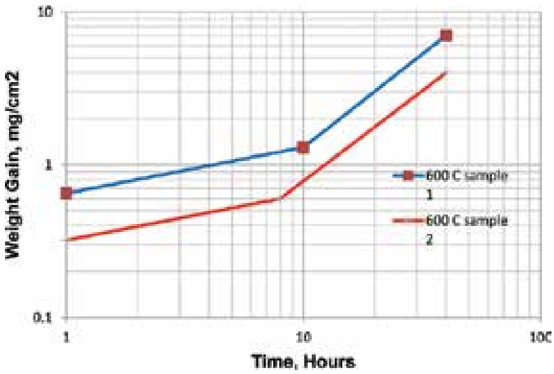

Figure 1. Weight gain of Zircaloy-2 at 600°C.

The two oxide growth measurements in **Figure 1** are for two samples cut from the same sheet and exposed to the same environment at 600°C. Oxidation growth for the other samples run at 600°C fell within these two extremes. Since the curves are almost parallel, the data obtained for each temperature were averaged to produce a single curve for each temperature. The averaged results are included in **Table 2** for Zircaloy-2 for the three different temperatures.

500°C		**600°C**		**700°C**	
Time	Wt. Gain	Time	Wt. Gain	Time	Wt. Gain
10	0.36	2	0.59	Not measured	
30	0.56	6	0.93	Not measured	
200	2.64	10	1.29	4	3.68
500	5.92	40	5.32	9	8.24

Time at Temperature (hours), Weight Gain (mg/cm^2).

Table 2. Oxidation gains Zircaloy-2

Although it appears from the table that very few data points were obtained and only two data points at 700°C, there was a large amount of data obtained for each data point presented and then they were averaged to produce the few results shown. In fact, the two 700°C points represent the average of about 10 data points each. Plots of these data are shown in **Figure 2** in log-log coordinates. As stated previously, the bend in the 500 and 600°C curves is referred to as the transition point between the initial (parabolic to cubic) reaction regime and the post transition linear reaction rate regime.

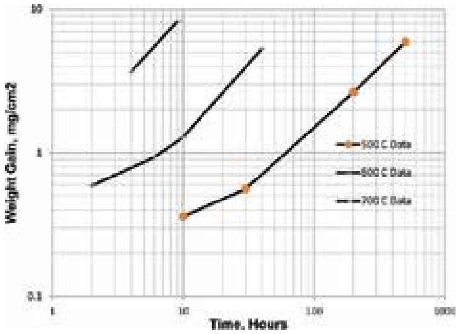

Figure 2. Averaged weight gain of Zircaloy-2, specimens at 500, 600, and 700°C [11].

Since the data appear as straight lines in each regime, the weight gain, *M*, in each section can be represented by a the product of the rate constant *k* and the time *t*.

$$M^n = kt \tag{1}$$

The values of n and k for each straight line section of a plot can be determined by first taking the log of this equation and evaluating it at two data points and subtracting one from the other to obtain

$$\begin{aligned} &n * \left(\log\left(M_2\right) - \log\left(M_1\right)\right) = \left(\log\left(t_2\right) - \log\left(t_1\right)\right); \text{is rearranged to;} \\ &n * \log\left(M_2 / M_1\right) = \log\left(t_2 / t_1\right) \end{aligned} \tag{2}$$

so that

$$n = \frac{\log\left(t_2 / t_1\right)}{\log\left(M_2 / M_1\right)} \text{ and } k = \frac{M_1^{\,n}}{t_1} \tag{3}$$

Kendall's Zirconium constants [11] and this work's slightly improved constants for Zircaloy-2 are presented in Table 2. Kendall [11] states that, "From the shapes of the curves and the calculated values of n_1 and n_2 above, it is evident that the same reactions control the rates at the different temperatures and that the reaction of Zircaloy-2 and zirconium are determined by the same mechanism. Variations in the values of n and k are then due to experimental error. A major source of error results from spalling of the reaction products. The reaction products of Zircaloy-2 are adherent and tough while those of zirconium are fragile and flaky." Kendall concludes that the exponents for the pre-transition regime are $n_1 = 2.58$ and linear, $n_2 = 1$, for the post-transition regime (**Table 3**).

Initial Reaction			**After Transition**	
Temperature, °C	k_1 (mg/cm^2)^n/hour	n_2	k_2 (mg/cm^2)^n/hour	n_2
Zircaloy-2				
500	7.43×10^{-3}	2.49	1.25×10^{-2}	1.13
600	1.34×10^{-1}	2.41	1.31×10^{-1}	0.98
700	Not determined	–	9.18×10^{-1}	1.01
Zirconium				
500	3.34×10^{-3}	2.64	3.52×10^{-3}	1.14
600	5.62×10^{-2}	2.41	(2.57×10^{-2})	1.11*
700	8.93×10^{-1}	2.82	1.57×10^{-1}	1.07

*Average of values at 500 and 700°C; data at 600°C inadequate for direct determination because of sample failure. k_2 calculated from this average value. (Units of w are mg/cm^2 and unit of t is hours for these values of k_1 and k_2.)

Table 3. Reaction constants.

The rate coefficients for Zircaloy-2 are plotted in **Figure 3** and the logarithms are seen to be linear with $1/T$, which shows that an Arrhenius equation can be used to fit these data.

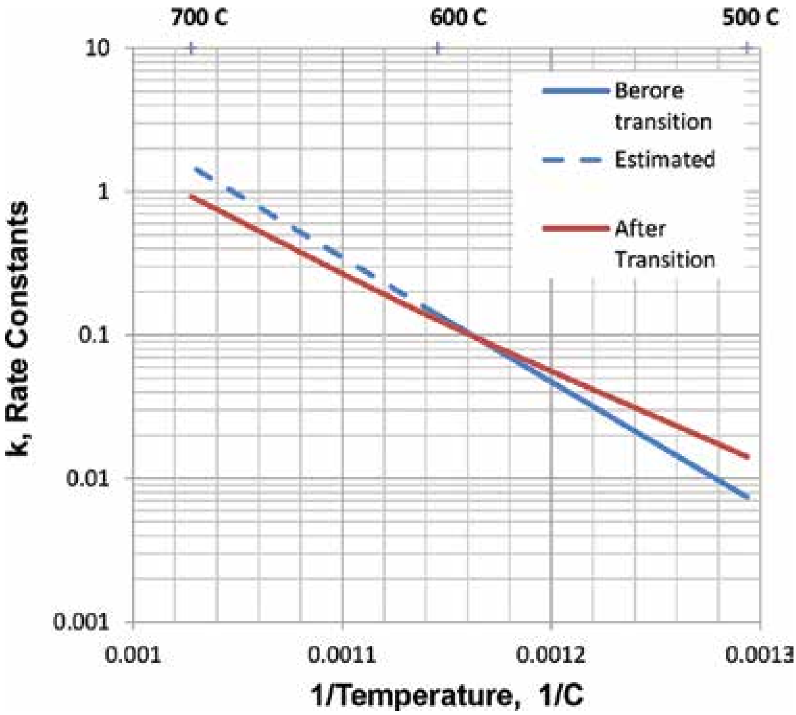

Figure 3. Rate constants for Zircaloy-2.

The rate constants in **Figure 3** are fit with the Arrhenius equation of the form

$$k = A * e^{\left(\frac{-Q}{RT}\right)} \tag{4}$$

where *k* is the rate coefficient, *A* is the "frequency factor", *Q* is the activation energy,

R is the gas constant = 1.9872 cal/(g-mole°K), and *T* is the absolute temperature, °K.

The activation energy, *Q*, is determined by taking the logrithm of both sides of the Arrhenius expression, evaluating at two data points, subtracting and solving for *Q* and *A*

$$\ln k = \ln A - \frac{Q}{RT} Q = R\frac{\ln\frac{k_1}{k_2}}{\left(\frac{1}{T_2} - \frac{1}{T_1}\right)} A = k_1 e^{+\frac{Q}{RT_1}} \tag{5}$$

Constants for both the pre-transition and post-transition regions were determined by Kendall [11]. The calculated values of A and Q that he reported for his data for both the pre-transition and the post-transition regions for both Zirconium and Zircaloy-2 are listed in Table 4.

	Before Transition			**After Transition**		
	A_1 $(mg/cm^2)^{2.58}$/hour	Q_1 cal/mole	n_1	A_2 (mg/cm^2)/hour	Q_2 cal/mole	n_2
Zircaloy-2	1.1×10^9	3.94×10^4	2.58	8.5×10^6	3.10×10^4	1
Zirconium	1.8×10^9	4.14×10^4	2.58	7.9×10^5	2.98×10^4	1

Table 4. Values of *A* and *Q* in the Arrhenius equation for Zircaloy-2 and Zirconium in dry air [11].

The final equation is obtained by substituting the Arrhenius expression into Equation 1

$$M_{\text{gain}} = \left\{ \mathrm{A} * \mathrm{t} * e^{\left(\frac{-Q}{RT}\right)} \right\}^{\frac{1}{\mathrm{n}}} \tag{6}$$

So, for example, the predicted amount of the oxide deposit after 10 hours at 500°C obtained from the above equation is calculated to be

$$M_{\text{gain}} = \left\{ 1.1\text{x}10^9 * 10 * e^{\left(\frac{-3.94x10^4}{2*(500+273)}\right)} \right\}^{\frac{1}{2.58}} = 0.400011\,\text{mg} / \text{cm} \tag{7}$$

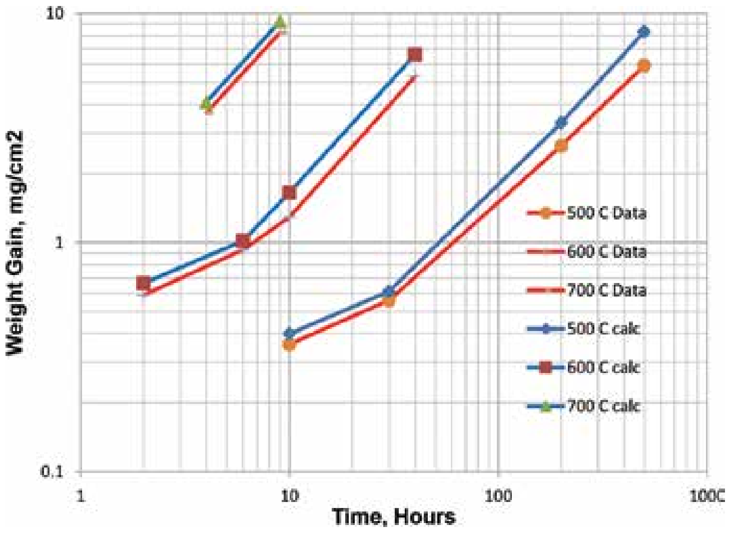

Figure 4. Comparison of final equations to original data.

The calculated results from the above correlation are compared in **Figure 4** to the original averaged data of **Figure 2**. It is seen the correlation values are all greater than the experimental values. So the constants in Table 4 will be used since they overestimate the total oxidation.

Equation 3, the above table, and graph list the weight gain per unit area from the reaction. The quantities of interest are: (1) the oxide thickness and (2) the loss of Zircaloy metal. These are obtained from Equation 3 for weight gain per unit area with the following relations.

The mass gain per unit area, $M_{gain}(mg/cm^2)$, due to Zr being oxidized to ZrO_2, is given by

$$\mathrm{M_{gain}} = M_{\mathrm{ZrO_2}} - \mathrm{M_{Zr}} \tag{8}$$

M_{ZrO_2} = mass per unit area of the oxide gained and M_{Zr} = mass per unit area of the metal lost.

$M_{\mathrm{ZrO_2}}$ and M_{Zr} to be related by the ratio of molecular weights as

$$M_{ZrO_2} = M_{Zr}\left(\frac{mw_{ZrO_2}}{mw_{Zr}}\right) \text{or transposing } M_{Zr} = M_{ZrO_2}\left(\frac{mw_{Zr}}{mw_{ZrO_2}}\right) \tag{9}$$

Substituting in gives

$$M_{\mathrm{gain}} = M_{\mathrm{ZrO_2}} - M_{\mathrm{Zr}} = M_{\mathrm{Zr}} * \left(\frac{mw_{\mathrm{ZrO_2}}}{mw_{\mathrm{Zr}}} - 1\right) = M_{\mathrm{ZrO_2}}\left(1 - \frac{mw_{\mathrm{Zr}}}{mw_{\mathrm{ZrO_2}}}\right) \tag{10}$$

Solving for M_{Zr} and M_{ZrO_2} from these equations and dividing by the densities ρ_{Zr} = 6.52 gm/cm^3 ρ_{ZrO_2}= 6.0 gm/cm^3, the thickness of metal lost and oxide gained are obtained.

The thickness of metal loss, T_{Zr} , in mils is given as

$$\mathrm{T_{Zr}} = \frac{M_{\mathrm{Zr}}}{\rho_{\mathrm{Zr}}} = \frac{M_{\mathrm{gain}}\left\{\dfrac{\mathrm{mg}}{\mathrm{cm^2}}\right\}}{6.52\dfrac{\mathrm{g}}{\mathrm{cm^3}} * 2.54\dfrac{\mathrm{cm}}{\mathrm{in}} * \left(\dfrac{123.224}{91.224} \quad 1\right)} \frac{1\,\mathrm{gm}}{10^3\,\mathrm{mg}} \frac{10^3\,\mathrm{mils}}{\mathrm{in}} = 0.172 * M_{\mathrm{gain}} \tag{11}$$

Similarly, the thickness of the oxide layer is

$$\mathrm{T_{ZrO_2}} = \frac{M_{\mathrm{ZrO_2}}}{\rho_{\mathrm{ZrO_2}}} = \frac{M_{\mathrm{gain}}\left\{\dfrac{\mathrm{mg}}{\mathrm{cm^2}}\right\}}{6.0 * 2.54 * \left(1 \quad \dfrac{91.224}{123.224}\right)} = 0.253 * M_{\mathrm{gain}} \tag{12}$$

So in summary, the thickness of the oxide layer in mils is 0.253 times the weight gain in mg/cm^2. The reduction in metal thickness in mils is 0.172 times the weight gain in mg/cm^2.

Figure 4 shows the post-transition period produces the highest rate of oxidation (i.e., slope or derivative, mg/cm^2/hr) so that use of the post-transition equation to estimate the oxidation rate, the oxide accumulation, and metal loss will overestimate these quantities. Since the weight gain post-transition is linear with time, this conservative oxidation rate is constant for a given temperature.

The oxidation rate in the post-transition region is the derivative of correlation equation (2a) or

$$R = \frac{dM}{dt} = A * e^{\left(\frac{-Q}{RT}\right)} \tag{13}$$

Kendall [11] used the values of *A* and *Q* from Table 4 to extrapolate the reaction rates to temperatures below 500°C without the benefit of additonal data but based on the applicability of the Arrhenius expression. Kendall's post-transition correlation is used in this document to conservatively estimate the oxidation rate over the range of interest from room temperature to 820°C. Additional data are referenced in the following discussion to show that use of his correlation conservatively bounds the Zircaloy-3 data obtained by Argonne at 600, 700, and 800°C and that his correlation conservatively bounds literature values of on Zircaloy-2 below 500°C even though his data were limited to the 500 to 700°C range.

2.3. Oxidation rates of Zircaloy-3 and low temperature data on Zircaloy-2

Boland [15] states that, "Data from the literature, (Kendall [11]; Lustman [12] and Tipton [16]) indicate that zirconium is more resistant to oxidation in air than Zircaloy-2, but no directly comparable data were found on the oxidation of Zircaloy-3 so that experimental data were obtained to supply the missing information. Since Zircaloy-3 contains less tin and more iron than Zircaloy-2, information in the literature would indicate that it should be more resistant to oxidation in air than Zircaloy-2. The published experimental data on oxidation has a scatter of about 50% and can be used only as a guide in estimating how fast oxidation occurs in alloys or environments that differ from those actually tested.

To obtain Zircaloy-3 oxidation data under temperature conditions similar to those expected in the reactor, samples of the cladding, which were removed from a fuel element after 805 transients, were tested in a furnace in the TREAT reactor building. Samples were cycled from room temperature to 600°C thirty-five times with a total time at 600°C of 69 hours. One of these samples was then heated to 800°C for 2 hours to simulate the cladding temperature that might follow an accident. The sample heated to 800°C showed an oxide penetration of about 2 mils while the other sample showed an oxide penetration of less than 0.5 mils." Boland did not translate the above into rates at 600 and 800°C, but instead reported corrosion rates for 600, 700, and 800°C.

Zirconium and Zircaloy-2 corrosion rates were computed at 500, 600, and 700°C using Kendall's constants substituted in Equation 2a. These and the Zircaloy-3 corrosion rates at 600, 700, and 800°C reported by Boland [15] are shown in **Table 5**. Boland did not include any details about the measurement or about whether they were based on the post-transition kinetics or simply the total corrosion weight divided by the time at temperature. The 0.5 mils at 600°C corresponds to 2.07 mg/cm^2 and if divided by 69 hours to a rate of 0.029 mg/cm^2/hour which is less than the 600°C value in Table 5. The 2.0 mils corresponds to 8.26 mg/cm^2 and if divided by 2 hours to a rate of 4.13 mg/cm^2/hr. The latter value is higher than the data in Table 5. A value of 0.21 mg/cm^2/hour reported by Freund [17] (converted from 0.9 mil/day) at 700°C is also included in the table and is close to the Boland number. The table values of Zircaloy-3 are less than those of Zircaloy-2 and slightly greater than zirconium.

Temperature, °C	Zirconium	Zircaloy-2	Zircaloy-3	Zircaloy-3*
500	0.003	0.015		
600	0.026	0.148	0.041	
700	0.150	0.926	0.24	0.21*
800			2	

*Converted value of 0.9 mil/day for Zircaloy-3 at 700°C P. 85 of Freund [17].

Table 5. Comparison of corrosion rates (mg/cm^2/hour).

Causey [18] of Sandia reports that a considerable amount of data on Zircaloy-2 have been obtained since the work of Kendall [11]. He states: "There are a substantial number of reports dealing with the oxidation of Zircaloy at temperatures of 527°C and below. Regardless of the type of oxidant (oxygen, water, water vapor, CO, etc.) to which zirconium or its alloys such as Zircaloy-2 and 4 are exposed, the general behavior of the process is more or less the same. The reaction rate depends more on the pressure of the gas than the composition and that it applies to air as well. Oxidation occurs at the same rate in air or in water and proceeds in ambient condition or in high vacuum. He reports the dependence of the post-transition oxidation rate R on temperature and pressure as

$$R = 13.9\, P^{\frac{1}{6}} \exp\left(\frac{1.47}{\mathrm{k}_B T}\right) \tag{14}$$

where R is oxidation rate gram/(cm^2·second); P is the pressure in atmospheres (note the factor $P^{1/6} = 1$ at ambient pressure; the activation energy is 1.47 eV; k_B is the Boltzmann constant (8.617×10^{-5} eV/°K).

This correlation is plotted in **Figure 5** along with Kendall's Zr-2 extrapolated correlation down to 200°C. It agrees well with the Kendall Zircaloy-2 correlation over the temperature range of 200 to 800°C. It is lower below 500°C than the Kendall Zircaloy-2 correlation extrapolated below 500°C, which means the Kendall correlation conservatively overestimates the rates below 500°C. And the Kendall correlation fits the Zircaloy-2 data in the medium temperature range of 500 to 700°C range where Kendall took his data. The Kendall correlation (extrapolated to 800°C) is also higher than the Argonne 600 to 800°C Zircaloy-3 data. Therefore, the Kendall correlation which is used by TREAT to estimate the amount of oxide which has formed on the fuel does so conservatively. Note no transients performed so far have brought the fuel or cladding above 600°C.

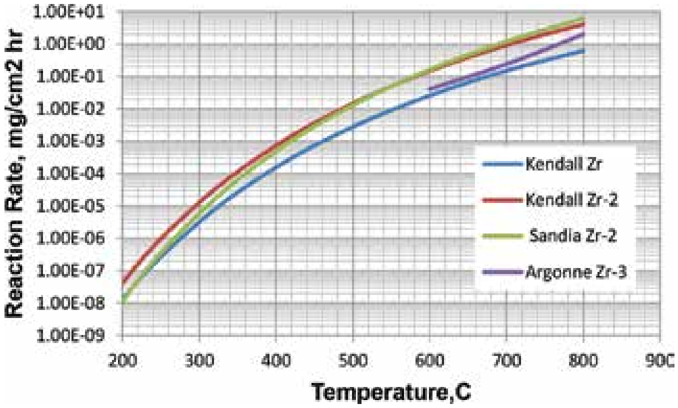

Figure 5. Comparison of the Kendall and Sandia correlations and Argonne Zircaloy-3 values.

2.4. Oxidation rates at higher temperatures and Zircaloy-4

Although the TREAT design basis accident shows that the cladding temperature does not exceed 820°C, higher temperature data are also of interest. The above three correlations were extrapolated to 900°C and are shown in **Figure 6** along with other data.

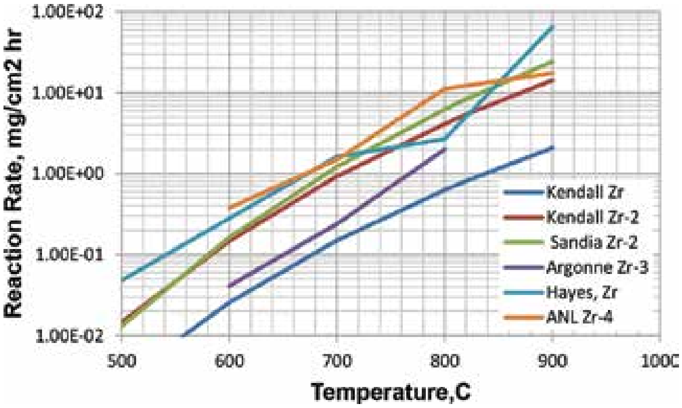

Figure 6. Comparison of correlations and data in the high temperature range.

Hayes [19] made measurements on zirconium in moist air up to and including 900°C. Hayes was only able to obtain oxidation data at 900°C for 1 hour whereas his 500 to 800°C data were gathered over a 24 hour period. As shown in **Figure 6**, except for the 800°C data point, the oxidation rate was higher for zirconium oxidation in moist air than the Zircaloy-2 rates of

Kendall. Other 900°C data include measurements at Argonne reported by Natesan [4] on bare Zircaloy-4 up to 900°C, which is also shown in **Figure 6**. Again, this is higher than the Zircaloy-2 data.

Hayes [19] concluded that the increase in the oxidation rate at 900°C is due to the change from alpha phase zirconium to beta phase zirconium at 862°C. He states "Microscopic examination of all specimens shows that there is no evidence of oxygen or nitrogen penetration into the body of the metal below 700°C. Short time exposures of less than 1 hour at 800°C produced only oxide surface layers and showed no evidences of further penetration. The specimens exposed for 1 hour and longer showed the intragranular rods and coarsened grain boundaries found in the oxygen series. In the 900°C series, it was found that the diffusion was extremely rapid. In one test with a thicker section, oxides were observed at the center of a quarter-inch (6.3 mm) sheet, which had been held at this temperature only 30 min. It appears probable that this sudden vulnerability to oxygen penetration can be ascribed to the change in volume that takes place at 862°C when the close-packed, hexagonal, alpha phase transforms to the body-centered, cubic beta form."

This large increase in the rate is not seen for Zircaloy-4, but perhaps this one metal sample was not representative. The design basis reactivity insertion accident maximum temperature is 820°C and this is below the zirconium phase change of 862°C. Although zirconium data in moist air and the Zircaloy-4 data are higher than the 1955 Kendall Zircaloy-2 correlation, the experience with the TREAT cladding is that the Kendall correlation in the dry climate of the INL and the less reactive Zircaloy-3 cladding has conservatively bounded the oxide growth. If there has been any oxide growth so far on the fuel, it is less than the uncertainty in the measurements of 0.5 mils [20]. Based on the continued low oxide buildup reported in Mouring [21] and Kramer [20], the conservative method of estimating oxide buildup is sufficient with visual observation if the computed buildup is greater than 3 mils or if the temperature of a transient exceeds 600°C.

2.5. Corrosion rate summary

In summary, to conservatively calculate oxide buildup on Zircaloy-3, use the oxide buildup rate equation for Zircaloy-2 which is

$$M_{\text{gain}} = 8.5 \times 10^{6} * t * e^{\left(\frac{-3.1\times 10^{4}}{1.9872*(T+273)}\right)} \tag{15}$$

Where M_{gain} is in mg/cm^2 and T is temperature in °C and t in hours.

The relations between the weight gain due to oxide buildup, M_{gain}, the metal loss thickness, and the oxide thickness, T_{ZrO_2}, are:

$$T_{Zr} = 0.172 * \bar{M}_{\text{gain}} \quad T_{ZrO_2} = 0.253 * \bar{M}_{\text{gain}} \quad T_{Zr} = 0.680 * T_{ZrO_2} \tag{16}$$

$$\frac{\text{Zirc Lost}}{\text{Oxide Thickness}} = 0.680$$

3. Maximum recommended operating temperature for Zirconium-3

The maximum cladding oxidation which is allowed in a light water reactor (LWR) is 0.17 times the total cladding thickness. This limit is imposed to prevent the cladding from becoming brittle, which occurs due to the incursion of hydrogen and oxygen into the grain boundaries in the unreacted Zircaloy-2 cladding. Oxygen incursion into the remaining metal is also a problem with the oxidation of Zircaloy-3. This problem is circumvented by limiting the maximum cladding temperature. Lustman [12] states that: "below 900°C no evidence was found for the penetration of oxygen or nitrogen into zirconium. Above the alpha-to-beta phase transformation the diffusion of oxygen into the metal was rapid." Alpha zirconium transforms to beta zirconium above 862°C as reported in Hayes, 1949. Both confirm that oxygen does not diffuse into zirconium below 862°C. So, the zirconium which remains under the oxidation layer will not become brittle as long as it remains below 862°C. Note, there is some variation in the literature on the alpha-to-beta temperature (for example, Lyman [22] reports 872°C). All, however, are equal to or above 862°C.

The zirconium transformation temperature is changed when it is alloyed into Zircaloy-3. The major additives in Zircaloy-3 are reported in Gibbons [1] as 0.2–0.3% Sn and 0.2–0.3% Fe. The only other trace element is a maximum of 0.05%. Lyman [22] and Hanson [23] report an increase in the transformation temperature with tin (Sn) concentration so that the tin addition does not lower this temperature. Hanson [23] shows a decrease in this temperature when Fe is added. A portion of the phase diagram boundary is shown and magnified in **Figure 7**. It is seen that with 0.3% addition of iron, the transformation temperature remains above 857°C.

Therefore, the transformation temperature for Zircaloy-3 is 857°C or above. Since Lustman [5] states that no penetration of oxygen or nitrogen was observed below 900°C for exposure up to 6 hours, this penetration is assumed to be very small between 850 and 900°C. Taking all of the above information into account leads to the conclusion that as long as the maximum limiting temperature is selected at or below 900°C, the disintegration of the metal due to nil ductility will not be a problem nor will there be a rapid increase in oxidation rate over that described above.

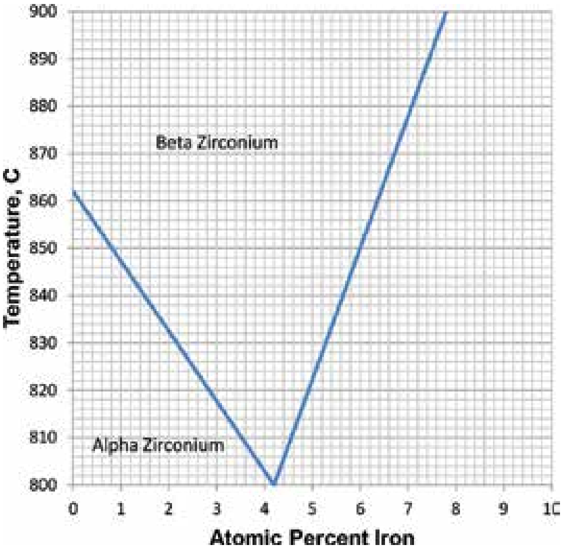

Figure 7. Partial phase diagram for the Zr Fe binary alloy.

The brittleness of the cladding material was also investigated experimentally. The approach to nil ductility is accompanied by an increase in hardness. Microhardness tests on a control sample and on each of the above samples showed an average hardness increase of about 45 Knoop hardness points for the heated samples. There was no clear pattern established between the center and the edges of the samples. If oxygen had diffused into the surface metal, one would expect a significantly harder material at the edge than in the center [15].

The weld material was also tested to determine if there was any preferential oxide formation in this area. A section of a sample that contained a weld was bent on a 3/8-in. diameter mandrel after the 600°C thermal cycling test without cracking the weld or the oxide layer over the weld. Metallographic examination of the welded area of a sample heated at 600°C did not show any greater oxide penetration than in the adjacent areas of the base metal [15].

The value of 820°C is recommended as the safety limit based on the above discussion and data. This value is sufficient to allow margin for operation, but is below the zirconium phase change of 862°C. This is a temperature limit at which further accident analysis would predict to not be exceeded with a large degree of certainty. Data for highly oxidized samples at 800°C do exhibit embrittlement and these are discussed in the next section.

4. Comparison oxidation correlation to experimental data on Zircaloy-3 samples

Zircaloy-3 samples approximately 1 in. square were oxidized in air for a range of temperatures for various times. The thickness of the oxide layer has been measured by an eddy current instrument. A color picture of the resulting sample set was taken and included in this chapter. The measured oxide layer is compared to the conservative equation (Equation 3) developed earlier. A best estimate correlation for cladding thickness was developed from the results. The sample pictures are placed on an excel spread sheet as a function of temperature and oxide thickness. The metal thickness remaining is estimated for those samples.

4.1. Comparison of conservative oxide calculation and measured data

Figure 8 shows a palette of 25 mil thick, 1 in. square samples of legacy Zircaloy-3 oxidized at specific temperatures for fixed periods of time (time listed is in hours(h)) starting at 500°C up to 1100°C. Two samples of the un-oxidized metal are also included in the top row. According to personnel observations, these samples, (photo, 2014) have the same appearance as when originally placed on the chart (circa, 1983). This provides evidence that the TREAT Zircaloy-3 cladding does not oxidize while in storage or in the inactive reactor.

Figure 8. Photograph of Zircaloy-3 oxidation chart (Photo taken 10/1/2014).

Wachs [24] recently measured the oxide thickness of these 1 in. square coupons. The oxide thickness was also calculated using the conservative technique (Equation 3). Both the measured and the conservative values are included in **Figure 8**. The reaction products of Zircaloy-2 are adherent and tough, while those of zirconium are fragile and flaky [11]. The samples of Zircaloy-3 also are tough and none of the oxide has scaled off.

The conservative equation for calculating the oxide thickness discussed earlier is:

$$\bar{M}_{\text{gain}} = t * 8500000 * e^{\left(-\frac{-31000}{1.9872*(T+273)}\right)} \tag{17}$$

The deposition in mg/cm^2 of each sample is converted to mils (Equation 4) as

$$T_{\text{ZrO}_2} = 0.253 * M_{\text{gain}} \tag{18}$$

For a few cases (very thin oxide layers), the measured values appear larger than the calculated values, but surface roughness and imperfections cause measured values to be at least 0.1 mils. In those cases, the conservative calculation is more accurate than the measured and the conservative values would be larger than the actual. A correlation which describes the actual thickness will be derived using the measurements and the conservative equation. For the highest temperature 1100°C, the measured values were slightly greater than the calculated values, which is probably due to the sample distortion.

All samples with measured oxide thicknesses less than 5 mils show color change due to oxidation and the samples are flat and undeformed. The largest oxide thickness measured on samples held at 700°C and lower was 4.9 mils (equivalent to 3.33 mils of metal loss) for 30 hours at 700°C. The oxidation occurs on both sides of these 25 mil thick samples, but for this subset of samples the backside oxidation has not affected the top side. Due to the TREAT fuel cladding cans being evacuated during fabrication, these samples with a metal loss of 3.33 mils or less on a side are representative of the TREAT cladding which only is exposed to air on one side.

This sample chart is reproduced in black and white, so colors have not been preserved. The five samples that appear in 500, 530, and 600°C are grey. The dots on the samples are light pink. All of the colors for samples 700 and 800°C that appear grey are actually a light pink. The grey colors in 1000 and 1100°C are really grey.

Figure 9 is a more detailed look gradual transition from a black oxide through pink dots to all grey for the samples at 530°C illustrating the color change as oxide thickness increase to 0.5 mils.

Figure 9. Expanded view of the 530°C gradual transition from black to grey oxide.

4.2. Correlation between the oxide measured and calculated thicknesses

A plot of the measured data versus calculated values from **Figure 8** is shown in **Figure 10**. An identity line is also shown. Data points below this line indicate that the calculated values are larger than the measured values. Points above are non-conservative. Three points are above the line which means they are non-conservative, one is for 1000°C and the other two are for 1100°C. Using all the data points to fit a straight line which goes through the origin gives a relation between measured and calculated of

$$T^{M}{}_{\mathrm{ZrO_2}} = 0.4794 * T^{C}{}_{\mathrm{ZrO_2}} \tag{19}$$

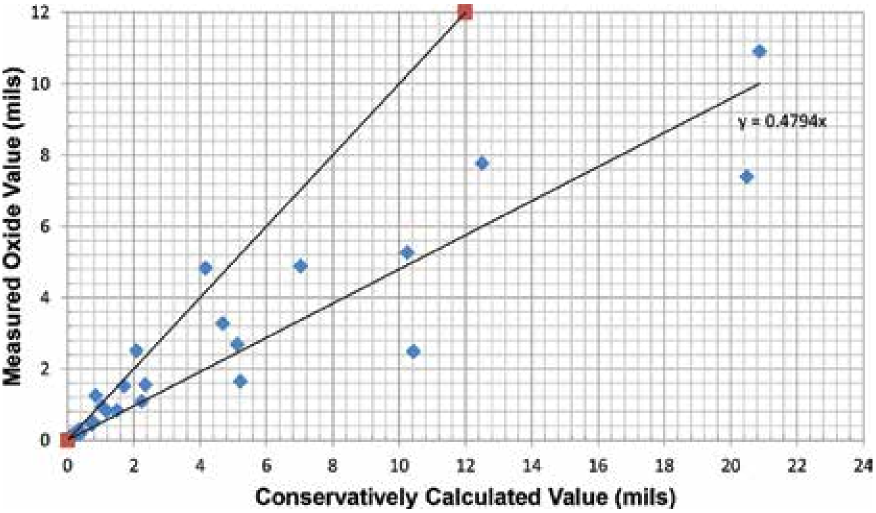

Figure 10. Measured versus conservative oxide values.

Combining this with the previous equation gives a correlation which predicts the actual oxide thickness.

$$T^{M}{}_{\mathrm{ZrO_2}} = t * 1030949.7 * \mathrm{EXP}\left(\frac{-31000}{1.9872 * (T + 273)}\right) \tag{20}$$

4.3. Oxide color as a tool for estimating oxide thickness

A qualitative evaluation may be made of oxide thickness by correlating color to oxide thickness. The surface color change to black occurs almost immediately with the start of oxidation (0.1 mils), but then remains the same for a certain amount of oxidation until it gets spots of pink. This occurs at slightly different amounts of oxidation for different temperatures. To see this more clearly, the samples have been placed on a grid in order of ascending oxidation as shown in **Figure 11**. The oxidation values used for plotting are the smoothed values from the above correlation, which are 0.4794 of the conservatively calculated values in **Figure 8**.

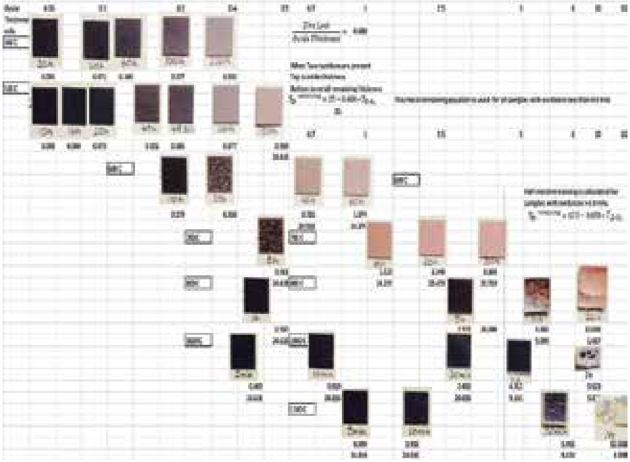

Figure 11. Samples placed according to oxide thickness and temperature.

Pink dots start to appear with about 0.2 mils of oxide for 500, 530, and 600°C. But this does not represent higher temperature oxidation, since the 5 hours 800°C is still black with an oxide thickness of 3.2 mils, and the 1 hour 1000°C is still black with an oxide thickness of 6.3 mils. The 500, 530, and 600°C start to turn grey at a thickness of 0.45 mils, although the grey in the 600°C samples appear to start at slightly larger thicknesses.

As a result of the above observation, it may be concluded that the oxide thickness transition between black oxide and grey oxide increases with temperature, so that a single color does not indicate a unique thickness of the oxide, but it does if the temperature history is known as it is in TREAT.

Figure 12 reproduces the 500, 530, and 600°C data, which is the expected region of interest in oxidation of the TREAT cladding since none of past transients have exceeded 600°C. As long as TREAT reactor excursions remain in the temperature range of 600°C and below, then the

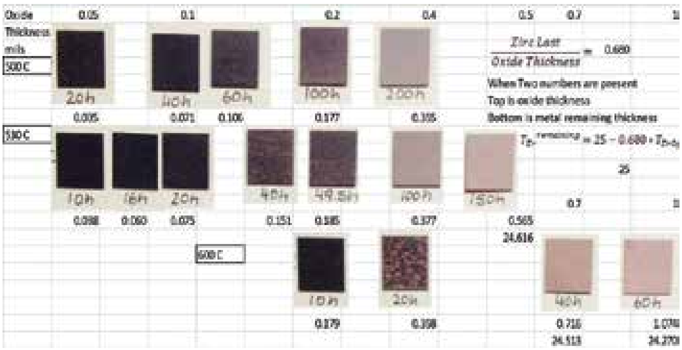

Figure 12. Color chart of concern to TREAT operation.

start of a grey color oxide layer would be evidence of an oxide between 0.35 and 0.75 mils thick. Black oxide would indicate an oxide thickness of 0.18 or less.

Since Equation 7 yields an estimate of the actual oxide thickness, the metal remaining in each sample is calculated by subtracting the metal loss from the original 25 mils. The metal loss is obtained from the ratio of oxide growth to metal loss, which is shown below as 0.680.

$$T_{\mathrm{Zr}} = 0.172 * \bar{M}_{\mathrm{gain}} T_{\mathrm{ZrO_2}} = 0.253 * \bar{M}_{\mathrm{gain}}, \text{so}\ \frac{\text{Zirc Lost}}{\text{Oxide growth}} = \frac{T_{\mathrm{Zr}}}{T_{\mathrm{ZrO_2}}} = \frac{0.172}{0.253} = 0.680 \tag{21}$$

For the 500, 530, and 600°C samples, the oxidation on the back side of the samples has no effect on the remaining metal, so the oxidation characteristics would be the same as that which would occur on the TREAT cladding which only oxidizes on one side. Therefore, the remaining cladding thickness on TREAT cladding which looks like the color of these samples can be calculated by subtracting the metal loss from 25 mils as in the following

$$T_{\mathrm{Zr}}^{\ \mathrm{remaining}} = 25 - 0.680 * T_{\mathrm{ZrO_2}} \tag{22}$$

These numbers have been included in **Figure 12** as the second number under some of the samples.

4.4. Determination of the minimum cladding thickness remaining

Although the TREAT cladding will probably never oxidize more than 2 mils, regulations require that a minimum undamaged metal (no oxygen incursion into the metal grain boundaries) remaining thickness limit be specified. This section determines the thickness of undamaged metal that is required for sufficient mechanical strength to be able to remove, insert, or handle a fuel assembly. This is then followed by a determination of the amount of oxidation that is acceptable to have the required thickness of the metal remaining.

The minimum undamaged cladding thickness needed during handling operations is based on the strength of the cladding. The handling forces,F_H, that the assembly must withstand are primarily in the axial direction being the weight of the fuel being suspended, friction between assemblies during insertion or removal, and sticking forces between the assemblies and the bottom grid plate. These forces are assumed to be borne by the cladding horizontal cross section,A_c. This undamaged cladding cross section is modelled as a uniform layer of metal around the circumference of the fuel times the perimeter of the fuel cross section. This assumes that oxidation leaves a uniform thickness of undamaged metal. The stress,σ , which occurs during fuel handling, is then estimated by the equation:

$$\sigma = \mathrm{F_H} / \mathrm{A_c} \tag{23}$$

The minimum area, and hence the minimum thickness allowed, would be that area able to support the maximum stress which the metal can support without incurring damage. This stress is taken to be the yield stress of Zircaloy-3. From the Alloy Digest, the yield strength of Zircaloy-3 at room temperature is 44.2 ksi and 16.7 ksi at 500°F (260°C) for undamaged metal. The yield strength of 16.7 ksi will be used to calculate minimum cladding thickness. Using the yield strength at 260°C is conservative in two ways. First, the yield strength is the stress where proportional elongation ends and where plastic deformation begins. The ultimate yield strength is where the material breaks. The yield strength is approximately 58% lower than the ultimate yield strength. Second, the use of the yield strength at 260°C is conservative because fuel handling operations are normally done at room temperature, with no reason to attempt to remove fuel from the reactor at higher temperature.

The force used to calculate the minimum cladding thickness is 300 lbs. This includes the weight of the fuel assembly (95 lbs) and any friction forces associated with assembly removal. The value of 300 lbs has historically been used as the limit during fuel handling operations. The area of the cladding, A_c, is obtained by solving Equation 12 for the area, by using the values of 300 lbs, and by requiring a safety factor of five times the area to account for non-uniformity in the oxide layer. The thickness of the cladding, T, is calculated by dividing the area required by the approximate circumference of the cladding.

$$\mathrm{A_c} = 5 * \frac{300}{16700} = 0.090\,\mathrm{in}^2 \quad T = 0.090\,\frac{\mathrm{in}^2}{16\,\mathrm{in}} = 5.6\,\mathrm{mils} \tag{24}$$

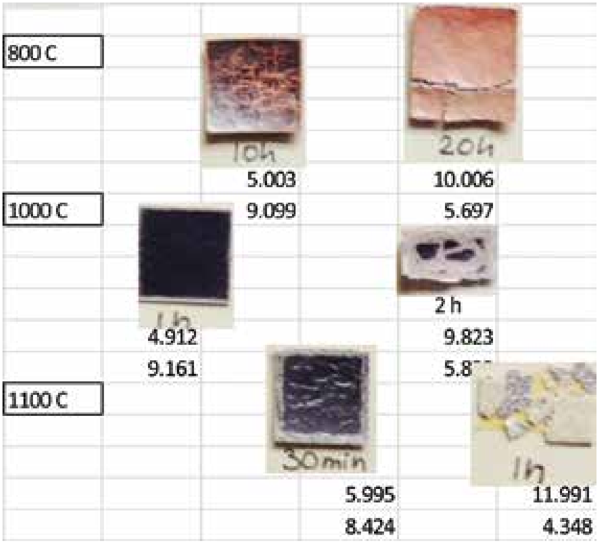

Figure 13. High temperature, high oxidation samples.

Since data are not available on 25 mils thick, one-sided Zircaloy-3 oxidized on one side, the minimum cladding thickness must be inferred from the data 25 mils samples oxidized on two sides. It is seen in **Figure 12** that the longer oxidation runs at 800, 1000, and 1100°C have experienced oxygen incursion and have become brittle. **Figure 13** shows this high temperature large oxidation part of Figure 12.

If a sample has become brittle, then oxygen incursion must have occurred from both the top and the bottom. Assuming symmetry, this would mean that the oxygen incursion reached half way through the 25 mils or 12.5 mils. A determination of half metal thickness remaining is calculated by the equation

$$T_{\mathrm{Zr}}^{\mathrm{remaining}} = 12.5 - 0.680 * T_{\mathrm{ZrO_2}} \tag{25}$$

Even though the 20 hours 800°C sample is below the 862°C limit temperature mentioned in Section 14a, it has become brittle which is evidenced by the large crack. To be conservative, it is assumed that in addition to the temperature limit of 862°C, there is also a limit on the amount of oxidation which can occur before oxygen penetration of the grain boundaries occurs at temperatures below 862°C. For this sample, the effective thickness of 12.5 mils shows that 10 mils of oxide formed (a loss of 6.8 mils of metal) and that 5.7 mils of metal under it became brittle. Almost the same value is observed in the 1000°C sample. This result is applied to TREAT cladding that is 25 mils thick and protected on one side by realizing that if 10 mils of oxide forms (which is 6.8 mils of metal loss), then an additional 5.7 mils of cladding under it has been damaged (brittle) and could not support a load. This would leave a thickness of 25 − 6.8 − 5.7 = 12.5 mils of undamaged metal left.

This is extended to other oxide thicknesses by assuming the damage thickness (embrittled) is proportional to the cladding thickness as

$$T_{\mathrm{damaged}} = 5.7 * T_{\mathrm{oxide}} / 10 \tag{26}$$

The amount of undamaged metal T_{Good} remaining is estimated by subtracting the metal loss due to the oxide layer 0.68 * T_{oxide} and the damaged metal layer 0.57 * T_{oxide} from the original metal thickness of 25 mils to obtain

$$T_{\mathrm{Good}} = 25\ \mathrm{mils} - 0.68 * T_{\mathrm{oxide}} - 0.57 * T_{\mathrm{oxide}} \tag{27}$$

Thus, the oxide thickness limit required to leave 5.6 mils of undamaged metal is determined by

$$5.6\ \mathrm{mils} = 25\ \mathrm{mils} - 0.68 * T_{\mathrm{oxide}} - 0.57 * T_{\mathrm{oxide}} \tag{28}$$

$$T_{\text{oxide}} = \frac{25\ \text{mils} - 5.6\ \text{mils}}{0.68 + 0.57} = 15.52\ \text{mils} \tag{29}$$

It must be remembered that the measurement technique measures oxide thickness and does not differentiate damage metal from undamaged metal. The remaining 5.6 mils of metal thickness remaining provides a factor of 5 safety factor to account for experimental uncertainties and non-uniformities in the oxide layer growth and excess.

The total remaining metal is 5.6 + 0.57 * 15.52 = 14.4464 mils, which is the minimum allowable metal thickness. These three components, oxide, brittle metal, and undamaged metal add up to the original 25 mils = 0.64 * 15.52 + 0.57 * 15.52 + 5.6. In summary, the two limits are:

Maximum oxide thickness allowable = 15.52 mils

Minimum metal thickness allowable = 14.45 mils

The oxide thickness which leaves only damaged metal is

$$0 = 25\ \text{mils} - 0.68 * T_{\text{oxide}} - 0.57 * T_{\text{oxide}} T_{\text{oxide}} = \frac{25\ \text{mils}}{0.68 + 0.57} = 20\ \text{mils} \tag{30}$$

The metal converted to oxide 0.68 * T_{oxide} = 13.6 mils. The damaged metal is 0.57 * T_{oxide} = 11.4 mils. This remaining oxygen damaged metal layer would not provide a complete barrier to keep air from the graphite-carbon fuel which might burn if it is at temperature over 700°C.

4.5. Deductions about cladding oxidation

The calculation of the cladding remaining with the Zircaloy-2 reaction rate from Section 1 compared to the oxidation samples shows that this equation is conservative. The measured data and calculations also show that, after approximately 35 years of operation at recorded temperatures up to approximately 570°C, and an accumulated energy development of over 2.6×10^6 MJ, there is minimal measured cladding oxidation. A continued program of oxide growth tracking for fuel assembly temperatures that exceed 400°C is considered prudent, but is not of sufficient concern to be included as a technical specification surveillance. However, as discussed in the previous subsection, an evaluation of cladding oxidation should be made if fuel assembly temperatures exceed 600°C. Part of this recommended evaluation should be the requirement to remove any fuel element that has less than 14.45 mils of cladding remaining or an oxide layer greater than 15.52 Mils. These are sufficient criteria to ensure fuel elements can be removed from the core.

As long as TREAT reactor excursions remain in the temperature range of 600°C and below, then the start of a grey color oxide layer would be evidence of an oxide between 0.45 and 0.92 mils thick. Black oxide would indicate an oxide thickness of 0.23 mils or less.

4.6. Current oxidation of TREAT fuel

The current oxidation of the TREAT fuel is basically the same as measured in the report of Kramer [20] in 1983. In the report, he determined the average amount of oxidation at that time (0.76 mils) and pointed out that it was less than the average measurement of Mouring [21] in 1977 (0.83 mils). In fact, the accuracy of the measurement method used on the fuel assemblies seems to be about 0.5 mils because the measurement head is affected by surface irregularities [20]. This is about the same magnitude as the most recent oxide measurements. Although Kramer [20] measured the average thickness at 0.76 mils, he also said that the observation of color put it in the range of 0.4 to 0.6 mils. Observations made in 1981 showed that the color was black with a touch of pink. This corresponds to a thickness of about 0.4 mils. Thus, it seems that the oxidation is less than 0.76 mils and may be as small as 0.4 mils.

It should be pointed out that even though the average measurements in Mouring and Kramer are about 0.8 mils, some of the measurements were as high as 2 mils. But Kramer pointed out that several factors caused inaccuracies in the measurements made with the fuel assembly in motion and tended to increase the value so that these higher values are probably misleading. These factors included roughness of the surface due to oxidation, scratches on the surfaces with left ridges, weld seams, etc. Also, the fact that the oxidation did not increase over the time between the two measurements in 1977 and 1983 indicates that the oxidation rate has been small.

A conservative method described in the next section is in place to keep track of an upper limit on how much oxidation has occurred. This tracking method is based on the conservative method of estimating the oxide growth rate. Measurements may be required as part of the evaluation for any fuel assembly that exceeds 600°C. It should be noted that 151 transients were performed since the last measurement and the oxide buildup is estimated at 0.229 mils [26].

The current number of transients on the fuel assemblies over 35 years of operation is 2880. The oxidation of the TREAT fuel has resulted in a loss of less than 1 mil of cladding loss over those transients. No more than an additional 1 mil cladding loss would be expected within the next 35 years of operation if the same type of transients and frequency as the original 35 years resulting in a minimum cladding thickness of 23 mils.

4.7 Predicted cladding losses during 10 years of operation

The section presents calculated results of temperature predictions in transients which are run in TREAT reactor and the amount of cladding oxidation which can be expected in each. **Figure 14** shows calculated temperatures for fuel and cladding following a transient where the hot spot fuel temperature reaches a maximum of 600°C.

It is assumed in the analysis that the reactor air flow rate is about 6000 cfm, which is the normal mode of operation during a transient. **Figure 14** shows temperatures for the case where the cladding has collapsed on the fuel. The control rods are pulled to their full out programmed location to begin a transient. The graphite carbon uranium fuel matrix heats up very fast (~1 sec). In this case, the cladding and fuel surface temperature equilibrate within 0.5 minutes.

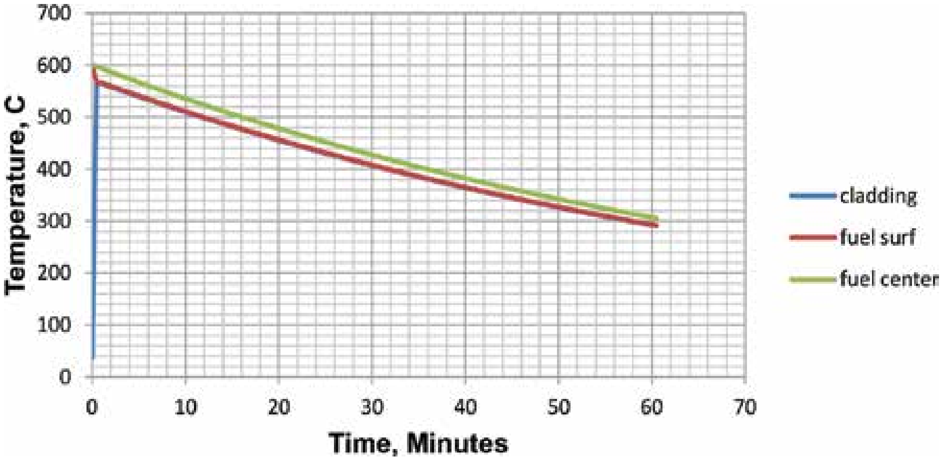

Figure 14. Cladding and fuel temperatures for the no cladding-fuel gap case.

Figure 15 shows the cladding loss during this transient, which is seen to reach 0.00152 mils. This value is less than 1/10 of one used by TREAT to estimate cladding oxidation, showing that the TREAT method is quite conservative.

Figure 16 shows the temperatures when it is assumed that the original 55 mil design gap still exists. The lower cladding temperature results in a cladding loss of only 0.000007 mils. The fuel assemblies in the outer regions of the core may retain their original gap, but the gap in assemblies in the inner region where the temperatures are highest have closed due to the weaker cladding at higher temperatures and the vacuum in the cladding can. Visual observation of the fuel (by technicians using binoculars) in the past has shown that the cladding has shrunk down on the higher temperature fuel because cladding indents were observed at the interfaces between the 8 in. long fuel blocks.

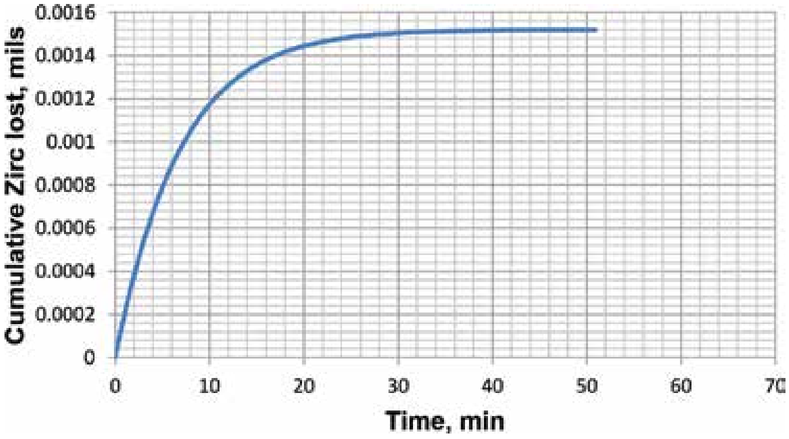

Figure 15. Cladding loss for the no cladding-fuel gap case.

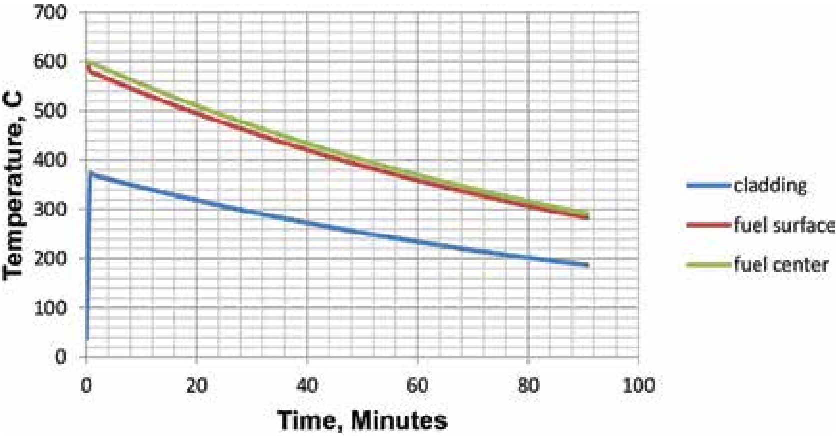

Figure 16. Cladding and fuel temperatures with a 55 mil gap.

Since the no-gap model of the fuel shows the most metal loss, it is conservatively used to estimate the cladding loss in other transients. The calculated amount of metal loss at the fuel hot spot for three temperature limited transients with no gap fuel is shown in **Table 6**. This calculation uses the conservative reaction rate described in the previous sections of this chapter.

Maximum Temperature of Transient	Metal Thickness Loss Calculated, mils	Metal Thickness Loss Used by TREAT, mils	Temperature Range Where the TREAT Metal Loss is Used.
600	0.00152	0.01693	500 to 600°C
500	0.00014	0.00153	400 to 500°C
400	0.000007	0	<400°C

Table 6. Comparison of calculated metal loss to loss used by TREAT.

The TREAT constants used to estimate cladding loss uses values [25, 26] also listed in Table 6. The metal loss for a 600 and 500°C transient that TREAT uses to estimate the total metal loss is seen to be over 10 times larger than the calculated value. Thus, the method used by TREAT is very conservative and estimates a metal loss more than 10 times larger than the conservative calculation presented here.

To be even more conservative, the TREAT method assumes that all the transients which have a maximum temperature between 500 and 600°C use the metal loss for a 600°C transient, and those which had a maximum temperature between 400 and 500°C use the metal loss calculated for 500°C. The metal loss for transients below 400°C is neglected.

As an example, the metal loss calculated with the TREAT method for an experimental program of 100 experiments in the 500 to 600°C range and 300 in the 400°C to 500°C range is

$$\text{Metal loss} = 100 * 0.01693 + 300 * 0.00154 = 2.17 \text{ mils} \tag{31}$$

which corresponds to a buildup of 3.19 mils of oxide. If 600 additional transients are assumed which reached 400°C, this would increase the calculated metal loss less than 1%. Thus, the metal will still be at least 22 mils thick after the above program assuming this conservative result. In fact, the smaller conservative values calculated after such a program is less than 0.2 mils.

$$\text{Metal loss} = 100 * 0.00152 + 300 * 0.00014 = 0.194 \text{ mils} \tag{32}$$

Even this later estimate is extremely conservative. Based upon the more realistic estimate of cladding oxidation, it is recommended that the TREAT values could be reduced by a factor of 10.

5. Cladding growth

Cladding oxidation also causes lateral growth of the cladding due to the increased specific volume of the oxide over that of the cladding. This growth could reduce cooling of the fuel assembly because it decreases the flow area between fuel assemblies. Such a decrease could also hamper fuel handling operations. When Zircaloy is oxidized in air, the oxide film is under lateral compression [11], and the growth of the base metal occurs from the tension the oxide puts on the base metal. Three measurements of growth were made: (1) A Zircaloy-3 fuel-element 48 in. long can exposed to air at 700°C for 48 hours exhibited longitudinal and transverse growth of 7/8 and 1/16 in., respectively [17]. (2) The growth observed in the 1 in. samples at 600°C for 69 hours was 3.2×10^{-3}in./in. (3) The sample heated to 800°C for 2 hours grew 2.5×10^{-3}in./in. Based on these tests, growth rate constants of 4.6×10^{-5}, 3.25×10^{-4}, and 1.2×10^{-3}in./in./h were obtained for temperatures of 600, 700, and 800°C, respectively.

An Arrhenius expression for the metal growth rate (MGR) has been used to describe the above data which is

$$\text{MGR} = 5000 * e^{\left(\frac{-32000}{RT}\right)} \tag{33}$$

where MGR is in (in./in./hour).

This expression is plotted for a range of temperatures in **Figure 17** and compared to the data. The expression is slightly larger than the above reported data so it is slightly conservative.

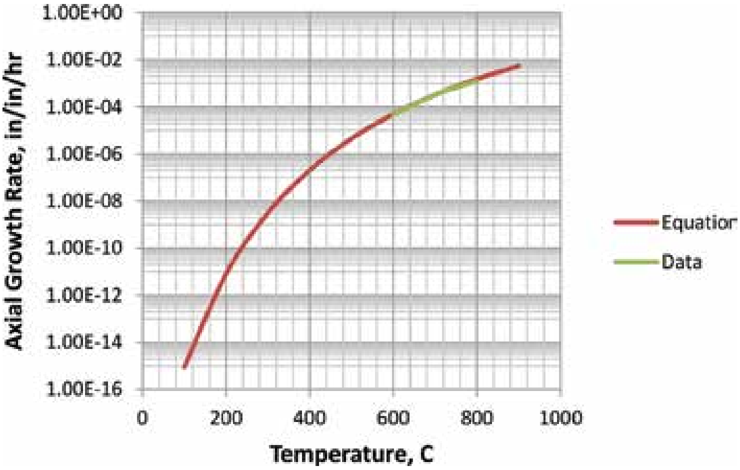

Figure 17. Growth rate of Zirconium-3.

The lateral growth for the TREAT 4 in. with fuel elements was calculated for 600°C transient presented in the previous section and the growth is shown in **Figure 18**. Similar calculations were done for 500 and 400°C. The resultant growth for each transient is shown in **Table 7**.

Maximum Temperature of Transient	Lateral Calculated Growth, mils	Temperature Range Where the TREAT Metal Loss is Used
600	0.011096	500–600°C
500	0.000949	400–500°C
400	0.000041	<400°C

Table 7. Calculated lateral growth of TREAT fuel elements.

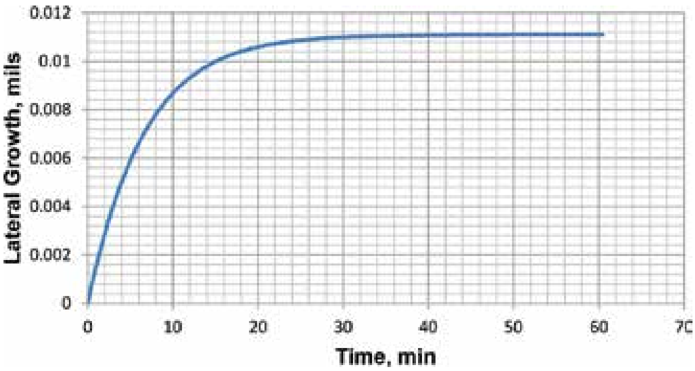

Figure 18. Lateral growth of fuel element during a 600°C transient.

Based on the conservative assumptions that the growth rate for transients above 500°C is equal to that at 600°C, growth rates for transients between 400 and 500°C are calculated at the 500°C rate, and transients 400°C or less at 400°C rate. The experimental program analyzed in the last section yields a total lateral increase of 1.15 mils.

$$\text{Cladding Growth} = 100 * 0.011096 + 300 * 0.000949 + 600 * 0.000041 = 1.15\ \text{mils} \tag{34}$$

This is a value which is too small to measure accurately due to the uncertainty of original width. The highest temperature elements would be the ones with the most growth, but these are the most likely to have the cladding collapsed on the fuel due to high temperatures and the evacuation of the fuel during manufacture. Fission gas production or any leakage into the cans would also change the geometry. The consequences of this possible growth are very small since the core is unclamped when fuel is to be moved and adjacent fuel elements can be moved to take out any elements which have grown.

A fuel element with 48 in. long fuel section could grow in the axial direction; but since the fuel elements are supported on a bottom grid and are free to grow longitudinally, a gradual change in length should not interfere in any way with reactor loading operations.

If temperatures in the fuel assemblies exceed 600°C during an off-normal event, an evaluation of the effect of oxidation on the cladding of a fuel assembly from the region of highest temperature shall be evaluated. If any unexpected oxidation or resulting growth of the cladding is detected during such an inspection, appropriate actions will be taken, such as removing all assemblies that have similar time-at-temperature histories or moving them to cooler areas in the core. Alternatively, reactor fuel temperatures could be limited to 400°C until a complete evaluation is made.

6. Summary of conclusions/recommendations

An equation based upon Zircaloy-2 oxidation rate is developed from the literature and compared to literature data that covers the range of temperatures from room temperature to 1100°C. This equation is shown to be conservative when predicting the oxidation rate of Zircaloy-3 based on the Zircaloy-3 data available. This equation is recommended to conservatively predict oxide growth, metal loss, and remaining Zircaloy metal.

An evaluation of the minimum temperature at which Zircaloy-3 transition between alpha and beta phase occurs concluded that 857°C is consistent and conservative with the data reported in the literature. The beta phase shows a rapid increase in oxygen inclusion in the grain boundaries with a corresponding increase in the brittleness of the Zircaloy-3. A safety limit of 820°C was chosen to avoid this undesirable behavior.

An equation was developed that expresses the relationship between the conservatively calculated oxide growth and measured data on 1 in. Zircaloy-3 samples. This equation was used to predict the actual oxide growth. A chart is provided on the use of Zircaloy-3 color to estimate oxide thickness in the range of interest for operation (<600°C).

A corroded cladding thickness of 14.45 mils is recommended as the limit below which fuel assemblies should be removed from service to ensure that fuel may be handled without damage. It was concluded that, based on historical data and conservative calculations, fuel assembly cladding would only develop another 1 mil of oxide for the next 35 years of operation if the cladding temperatures are maintained below 600°C. The total fuel growth was calculated for 150 transients conducted in TREAT. The total calculated growth was 0.36 mils. This is a value too small to measure accurately. It is recommended that the effects of cladding growth be evaluated if fuel assembly temperatures ever exceed 600°C.

Acknowledgements

This work is supported by the US Department of Energy, Office of Nuclear Energy, under DOE Idaho Operations Office Contract DE-AC07-05ID14517. Accordingly, the US Government retains a non-exclusive, royalty-free license to publish or reproduce the published form of this contribution, or allow others to do so, for US Government purposes. This information was prepared as an account of work sponsored by an agency of the US Government. Neither the US Government nor any agency thereof, nor any of their employees, makes any warranty, expressed or implied, or assumes any legal liability or responsibility for the accuracy, completeness, or usefulness of any information, apparatus product, or process disclosed, or represents that its use would not infringe privately owned rights. References herein to any specific commercial product, process, or service by trade name, trademark, manufacturer, or otherwise do not necessarily constitute or imply its endorsement, recommendation, or favoring by the US Government or any agency thereof. The views and opinions of authors expressed herein do not necessarily state or reflect those of the US Government or any agency thereof.

Author details

Charles W. Solbrig*, Anthony LaPorta, Katelyn M. Wachs and James R. Parry

*Address all correspondence to: Charles.Solbrig@inl.gov

Idaho National Laboratory, Idaho Falls, Idaho, United States

References

[1] Gibbons, R. C., Woldman's Engineering Alloys, American Society for Materials, 1979.

[2] Blanchard, J., Zirconium Cladding, *fti.neep.wisc.edu/neep423/FALL97/lecture9.pdf*, 1997.

[3] Alloy Digest, Zircaloy-3: Corrosion & Heat Resistant Alloy, ZZR5, ASM International, Engineering Alloy Digest, May 1969.

[4] Natesan, K., and Sopper, W. K., Air Oxidation Kinetics for Zr-Based Alloys, NUREG-CR-6846, University of Chicago; Argonne National Laboratory University of Chicago, U.S. NRC Division of Systems, June, 2004.

[5] Lee, J. M., Kim, J. S., Kim, Y. S., Air oxidation behavior of Zircaloy-4 at transient condition, Transactions of the Korean Nuclear Society Spring Meeting Jeju, Korea, May 17–18, 2012.

[6] Duriez, C., Steinbrück, M., Ohai, D., Meleg, T., Birchley, J., Hasted, T., Separate-effect tests on zirconium cladding degradation in air ingress situations, Nuclear Engineering and Design, 2009; 239: 244–253.

[7] Steinbrück, M., Prototypical experiments relating to air oxidation of Zircaloy-4 at high temperatures, Journal of Nuclear Materials, 2009; 392: 531–544

[8] Beuzet, E., Lamy, J. S., Simoni, E., Modelling of Zr-4 cladding oxidation by air under severe accident conditions using MAAP4 code, International Conference Nuclear Energy for New Europe, 2009, Bled/Slovenia/September 14-17.

[9] Duriez, C., Dupont, T., Schmet, B., Enoch, F., Zircaloy-4 and M5 high temperature oxidation and nitriding in air, Journal of Nuclear Materials, 2008; 380: 30–45.

[10] Steinbrück, U. Stegmaier, T., Prototypical Experiments on Air Oxidation of Zircaloy-4 at High Temperatures, report FZKA 7257, Institut für Materialforschung Forschungszentrum Karlsruhe, January 2007.

[11] Kendall, L. F., Reaction kinetics of Zirconium and Zircaloy-2 in dry air at elevated temperatures, HW-39190, Hanford Atomic Products Division, GE, September 1955.

[12] Lustman, B., Kerze, F., Jr., The Metallurgy of Zirconium, Chapter 11, First Edition, McGraw Hill Book Company, Inc., New York, 1955; 581–600.

[13] Phalnikar, C. A., Baldwin, W. M., Jr., The scaling of zirconium in air, American Society Testing Materials, Proceedings, 1951; 51: 1038.

[14] de Boer, J. H., Fast, J. D., The influence of oxygen and nitrogen on the α-β transition of zirconium, Recueil des Travaux Chimiques des Pays-Bas, 1936; 55: 461–468.

[15] Boland, J. F., Safety analysis of the operation of treat with fuel temperatures up to 600°C, Addendum to ANL-5923, Hazards Summary Report on The Transient Reactor Test Facility (TREAT), Idaho Division, December 7, 1967.

[16] Tipton, C. R., Jr., Editor, Reactor Handbook, Vol. 1, Materials, Interscience Publishers, Inc., New York, 1960, 726–738.

[17] Freund, G. A., et al., Design Summary Report on the Transient Reactor Test Facility (TREAT), Argonne National Laboratory, ANL-6034, 1960.

[18] Rion, A. C., Don, F. C., Bob, H. N., Review of the Oxidation Rate of Zirconium Alloys, Sandia National Laboratory, SAND2005-6006, November 2005.

[19] Hayes, E. T., Roberson, A. H., Some effects of heating zirconium in air, oxygen, and nitrogen, Journal of the Electrochemical Society, 1949; 96 (3): 142–151.

[20] Kramer, N. A., TREAT Fuel Assembly Cladding Oxidation Measurements Report, Argonne National Laboratory, ANL Report, October 1983.

[21] Mouring, R. W., TREAT Zr-3 Fuel Cladding Oxidation Measurements using Electromagnetic Techniques, Argonne National Laboratory, ANL Report, July 1977.

[22] Lyman, T., Ed., Metals Handbook, American Society for Materials, 1973.

[23] Hanson, M., Anderko, K., Constitution of Binary Alloys, McGraw-Hill, New York, 1958.

[24] Wachs, K. M., TREAT Eddy Current Oxide Evaluation, Technical Evaluation Report, Idaho National Laboratory, 2016, January 25.

[25] Solbrig, C. W., Intra-Laboratory Memo to L. J. Harrison, Tech Spec Requirements to Measure Cladding Thickness and Elongation, March 6, 1989.

[26] Neuman, L., Log of Maximum Metal Loss and Lateral Elongation as of 20 October 1995, 1995.

Chapter 5

Gamma Uranium Molybdenum Alloy: Its Hydride and Performance

Enrique E. Pasqualini

Additional information is available at the end of the chapter

http://dx.doi.org/10.5772/63652

Abstract

The high density metastable gamma uranium molybdenum alloy (γ-UMo) is being qualified as a nuclear fuel for the conversion of high enriched uranium (HEU) to low enriched uranium (LEU) fuels in research nuclear reactors. γ-UMo, with compositions between 7 and 10 wt.% molybdenum, has excellent properties to allocate fission gases but unacceptable behavior in contact with aluminum in the matrix of dispersed fuels. Development and processing alternatives are welcome to decide final working paths and new nuclear fuels design. A historical introduction on the development of materials testing reactors (MTR) nuclear fuels is presented to illustrate comings and goings to reach desired qualification objectives. Several studies performed on UMo probes, miniplates and full size plates are mentioned to contribute to the knowledge of fuel properties and to incorporate new process technologies. Focus is directed to the discovery of the gamma uranium molybdenum hydride and the hot rolling colamination of monolithic UMo with nonaluminum claddings. A scalable process of hydriding, milling and dehydriding (HMD) to comminute the ductile UMo was developed. Monolithic UMo miniplates with Zircaloy-4 (Zry4) cladding was colaminated for the first time and under irradiation conditions showed excellent performance after high burn-up.

Keywords: uranium, molybdenum, zircaloy-4, hydride, comminution, colamination, coverage

1. Introduction

Nuclear reactors can be divided into two types: those used to produce electrical power and those for other purposes. Power reactors take advantage of the energy liberated in the fission of fissile nuclides (^{235}U, ^{239}Pu) to produce electricity and nonpower reactors are used for training and mainly uses the neutrons produced in the fission reactions for materials testing, fuel qualification, radioisotope production, neutron activation analysis, neutron diffraction, silicon transmutation, research, etc. Actually, there are 442 operating nuclear power reactors in 33 countries around the world, while 66 are being constructed [1]; those used for naval propulsion are not recorded. Modern nuclear power reactors can generate more than 1000 MW of electrical power and one important characteristic of this type of reactors is that they work at temperatures higher than 300°C and usually at very high pressures [2]. Nonpower reactors are nominated by their maximum thermal power generated, which is proportional to neutron density; thermal power ranges go from practically zero up to some tens of MW, reaching in some cases powers of several hundreds of MW and fluxes greater than 10^{14} neutrons.cm^{-2}.s^{-1}. In these nonpower reactors, working temperatures are normally near room temperature; for very high density powers, maximum temperatures at the center of these high surface to volume ratios, fuel units do not surpass 200°C. There are 248 operating nonpower reactors in 52 different countries around the world [3].

Considering the different requirements to which both kinds of reactors are subsumed, the corresponding nuclear fuels have different characteristics. Typical operating power densities in power reactors are usually higher than 100 kW/l; in the case of nonelectrical power reactors, operating power densities can reach values as high as 1000 kW/l. Power reactors have their fuel material in the form of oxides, basically UO_2, with ^{235}U enrichment lower than 5%, in pellet form filling a zirconium alloy tube. Nonpower reactors have usually plate-like fuels, or pins, with some uranium compound powder dispersed in an aluminum matrix and with an aluminum alloy cladding. Seventy-six research reactors use high enriched uranium fuels (HEU > 90% ^{235}U) [4] and the remaining ones use low enriched uranium (LEU < 20% ^{235}U) fuel.

Actually, there is an important interest that the reactors that are working with HEU fuels be converted to LEU, trying to not affect their performance. The reason is to diminish proliferation risks since HEU is used for the construction of nuclear weapons.

1.1. The beginnings of testing reactors, 1948–1978

One of the first necessities in the development of power reactors was to acquire knowledge on the behavior of irradiated materials and devices. For these purposes, materials testing reactors were constructed. The greatest interest for this purpose, by the beginning of the 1950s, was to obtain thermal neutron fluxes higher than 10^{14} n.cm^{-2}.s^{-1}, high specific power and high excess reactivity, with the possibility of configuring slab geometries of the nuclear core so as to obtain particular neutron spectra [5, 6]. The reactor nucleus had a volume of 100 liters with a total power of 30 megawatts. The fuel elements with 200 grams of ^{235}U were assemblies of 19 hot colaminated curved plates brazed into slotted lateral plane plates [7]. The plates had inside a monolithic aluminum alloy with HEU shaping a dispersion of UAl_4 precipitates in a rich aluminum matrix and aluminum cladding. The monolithic meat had a total uranium density of 1.6 gU/cm^3. The typical size of the plates was 1.4 x 69 x 555 mm with a cladding thickness of 0.46 mm. Separation between plates was 2 to 3 mm with cooling water flowing between them at a velocity of 10 ms^{-1}.

Plates were also developed using powder metallurgy technology [8] with UO_2 dispersed in aluminum and in stainless steel obtaining higher charges of uranium densities. Maximum heat fluxes were 32 W/cm^2 in the case of aluminum plates working at 93°C and 70 W/cm^2 in the case of stainless steel plates working at 290°C. These power densities are equivalent to a maximum specific power of 2 kW/g of ^{235}U. Stainless steel plates had total and cladding thicknesses of 0.7 and 0.12 mm, respectively [9]. Plutonium and ^{233}U charged fuel plates were also developed [10].

At those early times, reactors with LEU were proposed showing that the critical mass does not increase significantly over that obtained using HEU; some metallurgical problems have to be reconsidered to fabricate in the highly concentrated combination required [11]. Tubular geometries of plate-like fuels were also used. Pool-type reactors and pressurized vessels were constructed. Channel-type reactors had different positions to obtain desired neutron fluxes and spectra avoiding fuel elements reconfigurations. Many other experiences were encouraged but the ones mentioned have many of the basic elements that are used up today in the fuel nuclear industry.

1.2. Enrichment reduction of nuclear fuels start up, 1978–1996

After India exploded a nuclear bomb in May 1974 a nonproliferation International Nuclear Fuel Cycle Evaluation (INFCE) was set up [12]. The Reduced Enrichment for Research and Test Reactors (RERTR) Program was released in 1978 to "develop technology necessary to enable the conversion of civilian facilities using HEU to LEU fuels and targets" [13]. The reason to adopt this criterion is that LEU is considered to be less of a proliferation concern than HEU because the critical mass—without neutron moderation—increases rapidly below 20% ^{235}U. One of the first fuels to be developed as nonproliferate was the French Caramel that consisted in plates with thin square slabs of UO_2—with uranium enrichment lower than 10% placed in a square pitch grid of zircaloy and welded between two zircaloy sheets [14]. The total uranium density of this fuel is 10.3 gU/cm^3 and takes advantage of the experience gained in power reactors. Because of low conductivity of the oxide, thin square type slabs were developed. Fuels with uranium oxides and silicides dispersed in aluminum had at that time less known performance. It is interesting to revisit some of the initial review works that followed the consolidated policy of enrichment reduction [15]. In this guidebook of 1980, preferred high density fuels were mentioned, such as U_3Si, UMo alloys and UO_2.

Experience can also be gathered from the design of nuclear fuels for naval propulsion, where several uranium compounds and enrichments were reviewed. As an example it can be mentioned that uranium with 10 wt.% (21.6 at.%) molybdenum alloys were used in fast reactors without surpassing 2% burn up because of excessive fission gas induced swelling that occurs at temperatures greater than 400°C [16]. It is also mentioned that in comparison with uranium niobium and uranium zirconium alloys, at lower temperatures, UMo alloys are apparently more resistant to swelling.

It was inevitable to move on to powder metallurgy to incorporate to the fuel more uranium to compensate the ^{235}U lower concentration. This technology was already known since dispersion fuel elements present several advantages over elements containing the fuel in homogeneous ceramic form [17]. Also it was in mind trying to use high density uranium compounds. In the case of uranium alloy worked as a monolithic meat with UAl_4 precipitates, the uranium loading must be less than 35 wt.% uranium (4 at.% U)—to avoid inhomogeneous dispersions that could produce hot spots—rendering a final meat density of 1.35 gU/cm^3 of total uranium. In the case of a UAl_x ($x = 2, 3$ or 4) dispersed powder in an aluminum matrix with a concentration between 40 and 50 v/v%, densities of total uranium in the meat can reach values higher than 2 gU/cm^3.

One of the simplest choices to increase fuel density was to develop fuel plates with LEU U_3O_8 dispersed powder in an aluminum matrix. The density of U_3O_8 is 8.3 g/cm^3 and the meat total uranium density can reach values higher than 3.1 gU/cm^3. Dispersed UO_2 powder in an aluminum matrix is less stable than U_3O_8 since important swelling is formed due to low density reaction products and diffusion porosity formed [17].

Uranium silicide compounds such as U_3Si and U_3Si_2 have different behavior under irradiation. While the first one presented in some cases break away swelling [18], U_3Si_2 was finally selected to rich total uranium densities at the fuel plate meat of 4.8 gU/cm^3 [19]. This fuel is the last one that has been qualified for general uses in research reactors using LEU. It is worthwhile to comment that U_3Si is a ductile compound and centrifugal atomization [20] was specially dedicated to obtain a ductile compound in powder form.

1.3. Uranium molybdenum long run qualification

By 1996, in a systematic study, several high density uranium compounds were revisited to be used as nuclear fuels with the intention of reducing even more the utilization of HEU in research reactor fuels and to look for a fuel more easily reprocessed than the U_3Si_2 dispersions [21, 22]. Some of these compounds to be qualified resulted to be gamma stabilized uranium alloys [23], in particular the metastable phase γ-UxMo. Quickly, it was determined in irradiation experiments that the needed composition had to have more than 6% w/w Mo ($x > 6$) [24]; afterwards it was observed that γ-UMo had an exceptional behavior in the allocation of fission gas bubbles [25]. UxMo alloys, with weights percent between seven and ten ($7 \leq x \leq 10$), are being tested since the stability of the gamma phase is enhanced as molybdenum concentration increases [26, 27], favoring intermediate fabrication processes. UMo presents interface incompatibilities with aluminum at high irradiation fluxes when fission gases generate undesired porosity [28–30]; this drawback is diminished by the incorporation of silicon to the aluminum matrix [31]. Fuel/cladding interaction can be minimized by covering the fuel particles with a diffusion barrier material or tailoring the fuel or matrix materials with the incorporation of additional alloying elements.

Since γ-UMo is a ductile alloy, it can be used as a monolithic fuel; nevertheless it cannot be colaminated with aluminum because of the different thermomechanical properties of both materials [32]. Several alternatives have been proposed to obtain a γ-UMo monolithic fuel with aluminum cladding [33]. They comprise a first step in which UMo foils are hot laminated to final dimensions and a second step is the incorporation of the aluminum cladding that can be performed by transient liquid phase bonding, friction stir welding or hot isostatic pressing. All of these three alternatives have UMo/Al interfaces where fission gas bubbles can coalescence. To avoid a UMo/Al interface a zirconium diffusion barrier can be incorporated between both materials and afterwards hot pressed to complete an aluminum cladding [34]. Irradiation results can be obtained in more detailed overviews [35].

2. γ-UMo massive hydride discovery and powder production

Several methods have been used to comminute UMo alloys: the more sophisticated centrifugal atomization already mentioned from KAERI, mechanical grinding performed initially in Canada and rotating electrode [36]. Studies of gaseous atomization with gold used as surrogate material to evaluate production performance were also performed [37]. Another explored possibility of comminuting UMo ductile alloys is by the decomposition of metastable γ-UMo in α-U and U_2Mo by a controlled heat treatment. When an incipient cellular precipitation totally decorates grain boundaries, the α-U phase present can be hydrided. The brittle hydride weakens the material that can easily be milled to particles of dimensions similar to the original grain size [38, 39].

Increasing the temperature of a quenched melted rod of U7Mo in a hydrogen atmosphere, hydrogen pick up started at around 100°C; the incorporation went higher than the hydrogen solubility limit and before decomposition of the metastable gamma phase took place [40,41]. It could be observed that a new phase begun to form at the place where tensile stresses were bigger. With this input, the method to completely hydride the γ-UMo alloy was developed. An hydriding, milling and dehydriding method, HMD, was set forward to obtain γ-UMo powder [42, 43].

2.1. Casting of UMo with stress retention

Batches of up to one kilogram of alloy were prepared with natural uranium (>99.7% U) and LEU (>99.9% U). Lumps of metallic uranium and molybdenum chips were used to prepare a 7% w/w molybdenum alloy. Uranium was deoxidized using nitric acid and molybdenum with melted sodium hydroxide. A high frequency induction furnace was used for melting the alloy in magnesium oxide crucibles and an inert gas atmosphere.

The melt was poured in a graphite dish obtaining a circular plate of approximately 8 mm thick and 120 mm diameter. Tension stresses at the top of the plate are retained since solidification begins at the bottom in contact with the graphite. The plate is finally broken in pieces (**Figure 1**) such that they can be incorporated in a hydriding chamber.

Residual tension stresses at the upper surface were checked by peak displacement in X-ray diffractions (DRX) in the as melted condition and after an annealing treatment (**Figure 2**). These stresses in the γ-UMo alloy are needed to allow the initiation of hydriding.

Figure 1. Eight millimeters thick uranium molybdenum lumps with residual stresses.

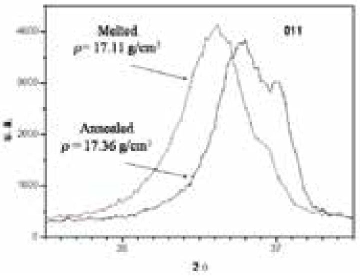

Figure 2. Evidence of stresses in γ-U7Mo shown by the displacement of the (011) DRX peak of a just melted and an annealed sample.

2.2. Low temperature hydriding of γ-UMo alloy

γ-U7Mo alloys were hydrided in a 1.5 l chamber vacuum and temperature assisted. A flow meter was used to measure the incoming hydrogen needed to keep a constant hydrogen pressure during absorption. In the stressed sample, hydrogen can be allocated in interstitial positions in the crystal structure (solubilization) or in hydrogen traps in dislocations generated by tension stresses. Traps must be filled with hydrogen to allow massive hydriding of γ-UMo afterwards. At 230°C, in a 10^{-3} torr vacuum, high purity hydrogen is introduced up to a pressure of 1 atmosphere, filling traps of the stressed γ-U7Mo alloy with some hundreds ppm of hydrogen in less than one hour [44]. Lowering the temperature to 120°C, hydrogen absorption begins after a few minutes; typical hydrogen absorption rates can reach values higher than 1 liter of hydrogen gas—at standard temperature and pressure—per minute per kilogram of alloy. After several hours, hydriding is completed. Hydrogen absorption dependence with time is shown in **Figure 3**. Additional temperature controls are needed during the process since the hydriding reaction is exothermic.

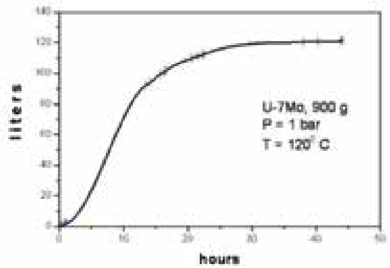

Figure 3. γ-U7Mo time dependence absorption of gaseous hydrogen at 120°C.

Optimum hydriding conditions were set up by observing the different hydrogen pick up rates in an increasing temperature slope and in a decreasing one, after hydrogen saturation of traps at 230°C. In **Figure 4**, it can be observed that hydrogen absorption rate while heating has a maximum value of 220 ppm/l and while cooling is much higher, 650 ppm/l, for a 700 g batch. From this curves it was determined that hydriding conditions were between 50 and 190°C, and the maximum rate is at 120°C.

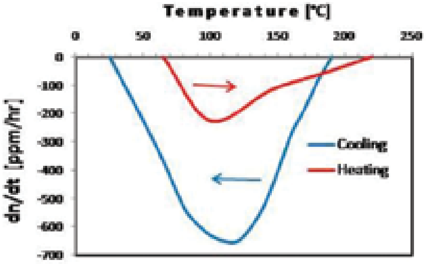

Figure 4. Hydrogen absorption rates during heating and cooling of a γ-U7Mo batch.

If a piece of γ-UMo is heated above 230°C in a hydrogen atmosphere, tension stresses will appear as it is cooled, inducing the massive hydriding of the material. This explains why in a cooling cycle hydrogen absorption is higher than in a heating one [42]. U10Mo has also been hydrided with similar results utilizing selected heating and cooling cycles such that hydriding conditions can be reached without initially incorporating residual stresses [45, 46].

After the hydride is totally formed at 120°C, it is convenient to increase the temperature up to 325°C and evacuate the chamber to eliminate the hydrogen in traps; this procedure makes the hydride less pyrophoric. Finally, at room temperature, air is introduced in a temperature controlled way such that the hydride is passivated.

2.3. Characterization of the γ-UMo hydride

The γ-U7Mo hydride is dark gray, brittle, fragmented in platelets, with small transgranular cracks (**Figure 5**). It is pyrophoric and burns with flame because of hydrogen liberation. When oxidized in air, it is dark brown. Rietveld refinement of a X-Ray diffraction—XRD—pattern

(**Figure 6**) show wide peaks corresponding to a unique stressed crystalline cubic *A-15* structure (space group $Pm\bar{3}n$, *N° 223*) of the β-W prototype, the same as β-UH_3 [47, 48] with eight heavy atoms in its unit cubic cell with parameter 6.6598 Å; the stoichiometry is of $(U7Mo)H_{3\text{-}y}$ with values of y smaller than 0.2 obtained experimentally by weight difference. The XRD hydride density is 10.39 g/cm^3. Since the density of γ-U7Mo with a unit bcc cell parameter of 3.4785 Å is 17.5 g/cm^3, the increase in volume during hydriding is 68%, causing the fragmentation of the brittle hydride that is being formed.

Figure 5. γ-U7Mo hydrided fragments.

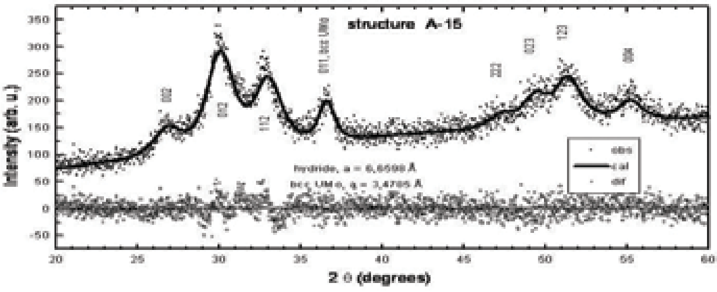

Figure 6. XRD, Rietveld refinement and indexation of $(U7Mo)H_3$ A-15 structure.

2.4. Milling of the γ-UMo hydride

Vickers hardness of the hydride $(U7Mo)H_3$ is approximately 300 VH. This hydride must be milled in a sufficient inert atmosphere to avoid burning up. Low impact mills are preferred to avoid excess fines (particle size smaller than 45 μm). Two roll mills and/or conical vibratory crushers were used (**Figure 7**). Hydride was first reduced with a manual roll mill in a glove box with less than 5% oxygen (mesh #10, 2 mm opening). These particles were then passed once through a conical crusher in a dynamic inert atmosphere reducing the size (#120, 125 microns). **Figure 8** shows hydride (γ-$U7Mo)H_3$ milled particles of 80 μm mean size. Passivation is needed before exposing the particles to air.

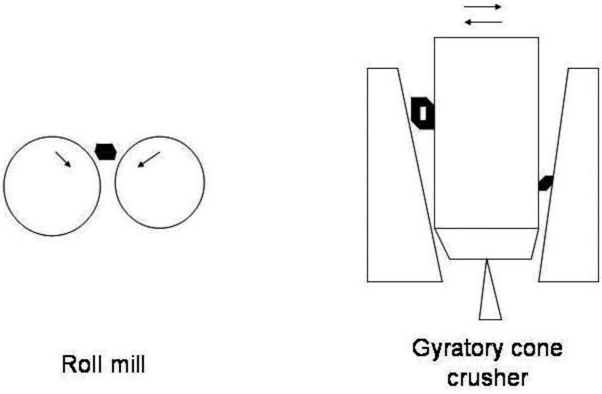

Figure 7. Low impact mills: roll (left) and gyratory cone (right).

Figure 8. (U-7Mo)H_3 powder of 80 μm mean size. SEM.

2.5. (U7Mo)H_3 dehydriding

The dehydriding of the powder is done in a vacuum atmosphere with a decrease of hydride size that is important because of the density difference with the final γ-U7Mo powder. Any gas evolution is followed by pressure measurements with a closed chamber; periodic evacuation is performed to reduce excess pressure. Hydrogen liberation begins at 125°C and beyond 425°C can be bursting. The hydrogen in traps—that is incorporated at 230°C—is liberated at temperatures between 300 and 375°C, whereas the hydrogen in interstitial sites—incorporated at 120°C—will begin to be evacuated at temperatures above 380°C as shown in **Figure 9**. If, after hydriding, hydrogen in traps is removed as mentioned in 2.2., the bump of hydrogen pressure increase at 325°C will not be observed.

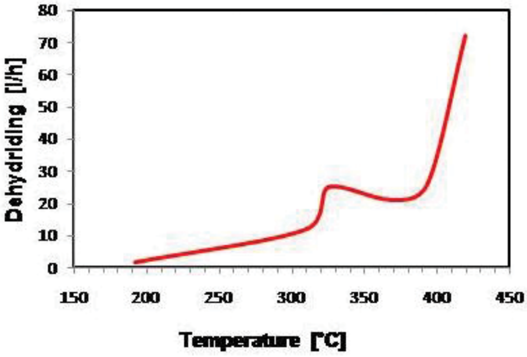

Figure 9. Hydrogen evolution during dehydriding. Hydrogen in traps and interstices are liberated around 325°C and beyond 425°C, respectively.

To eliminate hydrogen to lower values than 50 ppm heating up to 700°C in a dynamic vacuum atmosphere during 2 hours is needed. The heating chamber was vibrated to avoid the sintering of the particles. When the dehydriding is finished, an inert gas is introduced and quick cooling to room temperature is needed to quench the metastable γ-U7Mo phase. Controlled passivation is done by slow removal of the inert gas and air introduction. Dehydriding needs at least 5 hours. Cracks formed during the hydriding process are still present after dehydriding (**Figure 10**). The powder must be kept in an inert atmosphere to avoid oxidation.

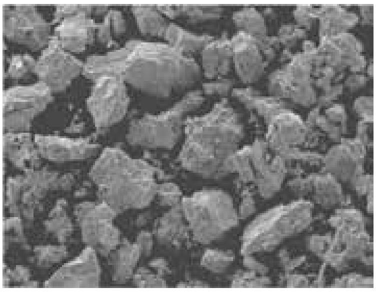

Figure 10. HMD γ-U7Mo powder. Big particles are 100 μm size (SEM).

If it is of interest, cracks can be sintered with a heat treatment of 8 hours at 1000°C in a vacuum atmosphere in the vibrating chamber [44]. **Figure 11** shows the results of this treatment.

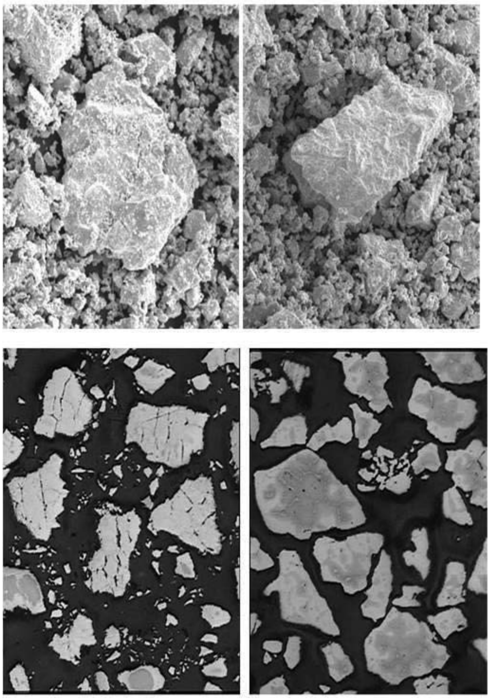

Figure 11. SEM (first row) and metallographies (second row) of γ-U7Mo powder before (left column) and after (right column) heat treatment at 1000 °C in a vacuum atmosphere. Big particles are 100 μm.

2.6. Absorption, coverage and lamination

The surface absorption of HMD powder in an air atmosphere was studied by increasing the temperature in a closed vibrating chamber. The volume of the chamber and piping was of approximately 3 liters and runs with 64 and 130 grams of γ-U7Mo HMD powder were performed [49]. **Figure 12** shows the pressure evolution from an initial value of 800 mbar air atmosphere as temperature is increased up to 500°C. The initial increment in pressure corresponds to surface gas desorption, fundamentally water at 120°C. A first run with 64 g showed an important pressure reduction up to a value of 200 mbar. Two consecutive runs were performed with a fresh 130 g sample of γ-U7Mo to evaluate if equilibrium is reached or a diffusion barrier was formed. The first run with this second batch, curve 130 g in **Figure 12**, was heated up to equilibrium. The second run, curve 130 g bis, was performed after cooling and reintroducing air in the chamber. These last two runs showed that pressure equilibrium was achieved without reaching saturation. Oxygen and nitrogen were incorporated without presenting a barrier to gas diffusion; nitrogen incorporation is known that begins to be important at temperatures higher than 300°C in metallic uranium [40]. A similar scenario will be present inside a picture and frame ensemble before hot rolling.

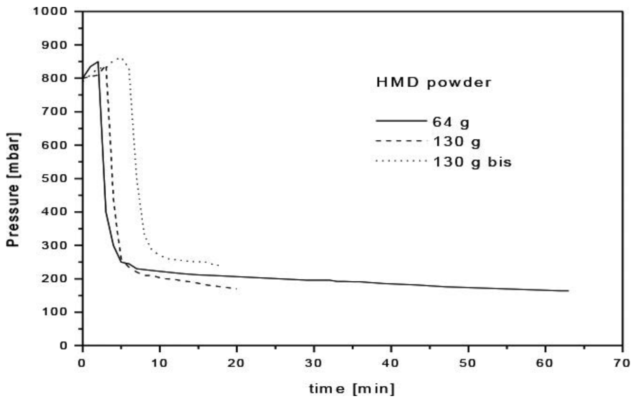

Figure 12. Pressure evolution with temperature of γ-U7Mo HMD powder exposed to an air atmosphere in a closed chamber.

Coverage of γ-UMo powder is of interest not only to diminish oxidation during storage but fundamentally to have a diffusion or metallurgical barrier protection against undesirable growth of, for example, the UMo/Al interaction zone during high flux irradiation. Surrogate powders were used to initially set up equipment and coverage conditions; silicon, aluminum, magnesium and silicon were used with chemical vapor deposition and dip coating techniques [50, 51]. Physical vapor deposition [52] is another possibility of coverage technique. Mixed powders of UMo and silicon in the vibrating chamber at 950°C in vacuum during 2 hours cover the bigger UMo particles with silicon [51].

The coverage of ductile UMo particles with brittle materials is thermomechanically incompatible in layers thicker than 1 micron. Probably ductile nickel and niobium seem to be better candidates as they have been tested previously in other nuclear fuel developments. New technologies are now available that consist in particles spheroidization and coverage using an induction couple plasma equipment that nowadays can be purchased in a commercial form [53].

The brittle transgranular fractures produced during comminution of the hydride gives as result polyhedral shaped particles. **Figure 13** shows a metallography of the laminated meat of a dispersed HMD miniplate with γ-U7Mo powder in an aluminum matrix. The irregular shape of HMD particles favors the mixing with Al powder, diminishes flow segregation—compared with spherical particles—and green compacts practically have no shredding. Cracks in the HMD particles do not propagate during hot lamination since UMo is a ductile alloy. Final porosity of a meat with HMD powder is between 5 and 10% v/v. Dispersed UMo particles in an aluminum matrix miniplates were also colaminated using silicon covered U7Mo HMD powder and centrifugal atomized particles with LEU and natural uranium [51].

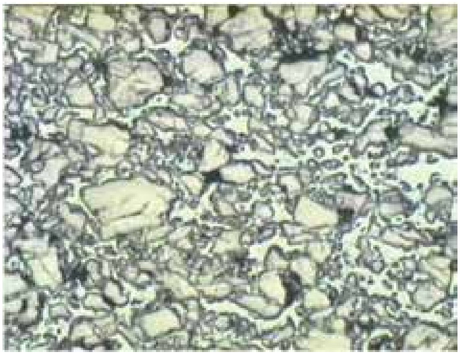

Figure 13. Metallography of the meat of γ-U7Mo HMD powder dispersed in an aluminum matrix of a laminated mini-plate. The size of the big particle is approximately 100 microns. Holes between particles were fundamentally produced during polishing.

Monolithic UMo meats can be obtained by powder metallurgy. A coupon of U7Mo HMD powder was cold pressed and surrounded by AISI 304L stainless steel in the standard lids and frame configuration to conform the cladding (**Figure 14**). Colamination was performed at 675°C, a temperature in the gamma phase stable zone of the U7Mo, in a nitrogen atmosphere. The use of a UMo monolithic meat elaborated by powder metallurgy allows an easier way of obtaining different meat widths in the same plate using conformational dies, incorporation of powdered neutron moderators such as high temperature stable hydrides, burnable poisons and also nanosized porous powders to adsorb fission gases at grain boundaries so as to reduce overall swelling of fuel plates [54].

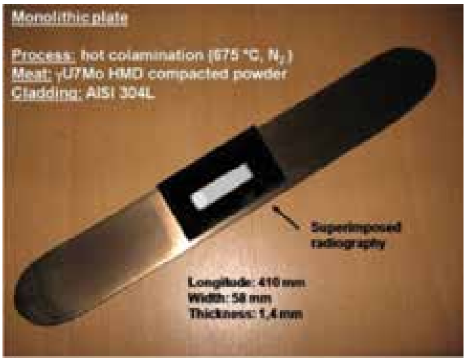

Figure 14. Monolythic UMo miniplate with stainless steel cladding.

3. Monolithic γ-UMo miniplates with cladding of Zircaloy-4

UMo and aluminum have interlayer incompatibility under irradiation and different thermo-mechanical properties that complicates a monolithic plate fabrication. These conditions can be avoided if the aluminum is replaced by a more friendly material with UMo such as Zircaloy-4, used in fuel tubes in power nuclear reactors [49, 50]. UMo has low plastic deformation compared with Zry-4; the latter has a coefficient of thermal expansion (6.10^{-6} $°C^{-1}$) less than half of the UMo coefficient [55]. Probably for this reason never before hot rolling colamination was applied to the system UMo/Zry, although UMo alloys have been co-extruded with Zircaloy-2 in plate and rod shapes [40, 56]. Hot rolling colamination needs several deformation steps while coextrusion is performed at higher temperatures in only one deformation step. The interaction zone growth kinetics between UMo and Zry is well known [40] and more recently it was shown by calculation that there exists a low interaction between Zr and UMo alloys [57]. Finally, a fabrication technique was developed [51], and two fuel miniplates were produced, irradiated and the post irradiation examination (PIE) was performed [43, 54, 58, 59].

3.1. Colamination parameters

Colamination temperature was chosen around 650°C where γ-UxMo phase is stable and Zry-4 is in α phase (<850°C) minimizing oxide layer growth in an air atmosphere. A uranium 7% (w/w) molybdenum alloy was chosen to maximize uranium content. Total welding in the sandwich hot colamination can only be achieved through sequential deformation steps. Differential contraction of UMo and Zry-4 in the cooling between colamination steps was avoided by quick reentrance to the heating furnace. It is illustrative to repeat a detailed description of this process mentioned in reference [43]: "The process of furnace extraction, lamination and placement again in the furnace was carried out as quickly as possible minimizing contact with cold surfaces. Thickness measurements were replaced by a very fast measurement of the plate length with a ruler from which the reduction pass was calculated. If the reintroduction in the furnace is not quick enough, repeated "crick" sounds are heard, indicating the breaking of the partial welds that were formed. After several steps, the contact surfaces are totally welded. The involved difference in contraction after final cooling are of the order of 1% and the stresses involved are absorbed by plastic deformation, as it is clear from past successful extrusion experiences. Very different sounds are heard when dropping good and bad laminated miniplates in a table: an'applause' sound stands for not totally welded surfaces, while a metallic sound is heard with a 100% surface welded miniplates. Welding between meat and frame was checked by destructive metallographic techniques."

3.2. Fabrication of miniplates

After several testing developments steps of the hot co-lamination processes (**Figure 15**), two monolithic LEU γ-U7Mo fuel miniplates with Zry-4 cladding were fabricated in CNEA for irradiation in the Advanced Testing Reactor (ATR) at Idaho National Laboratory (INL). Miniplates final size was 100 x 25 mm with a total thickness of 1 mm; nominal meat thicknesses were 0.25 (MZ25) and 0.50 (MZ50) with 0.36 and 0.25 mm of cladding thickness, respectively.

Figure 15. Monolithic γ-U7Mo/Zry-4 miniplates used along the different development stages. The three at the right extreme are in an intermediate step of surface oxide removal.

3.2.1. Alloy melting and sandwich preparation

The LEU uranium molybdenum alloy for the MZ25 and MZ50 miniplates was melted in the same way as described for powder production in section 2.1. using a graphite vertical mold to cast a 75 x 100 mm^2 plate of 2 mm thickness. Sandwich preparation was performed using the lids and frame technique thoroughly described in a previous work [43]; overall thickness of both packs was 4 mm (**Figures 16** and **17**)

Figure 16. Finished frames, lids and coupons of MZ25 and MZ50 ready to be stacked and welded to conform the two sandwiches.

Figure 17. TIG welded sandwich of monolithic U7Mo meat and Zry-4 clad ready for hot co-lamination.

3.2.2. Colamination of UMo with Zry-4

Both Zry-4/U7Mo/Zry-4 stacked plates TIG welded (sandwich) were hot colaminated using 150 mm rolls. The Stanat rolling mill had entrance guides to quickly position plates that were heated at a temperature of 675°C in an air atmosphere. To minimize the oxide layer growth the heating time between passes was set up at minimum values that could guarantee tension relieving and recrystallization of UMo. Totally welded interfaces ND near final thickness were reached after eight passes. Mean reduction step was 17.5% and mean heating time was 7.5 min; all the colamination process takes a total time of one hour. The cooling after the last lamination step must guarantee the retention of the metastable γ-U7Mo phase.

3.2.3. Final procedures

After the hot colamination, the plates were straightened in a multi roller machine and the oxide layer must be removed. Wet silicon carbide sand papers were used for this last purpose. The final thickness was reduced in 0.1 mm with the oxide layer removal and surface polishing.

Ultrasonic testing was performed to control 100% welding, and X-Ray radiography was used for checking meat dimensions, density homogeneity, dog boning, meat folding, etc. Cutting to obtain final dimensions was done with a guillotine. Identification of the miniplates was the last step of the fabrication procedure (**Figure 18**).

Figure 18. γ-U7Mo/Zry4 finished mini-plate of 100 x 25 x 1 mm^3 size. Meat and cladding thickness are 0.50 and 0.25 mm, respectively.

3.3. Monolithic miniplates characteristics and irradiation

The final characteristics of miniplates MZ25 and MZ50 are summarized in **Table 1** showing plate and cladding thickness, the dimensions and density of the monolithic γ-U7Mo meat and the total uranium with its meat uranium bulk and surface density.

Miniplate	Units	MZ25	MZ50
U enrichment	% ^{235}U	19.86	
U composition	% w/w U	92.91 ± 0.09	
Mo composition	% w/w Mo	7.04 ± 0.07	

Miniplate	Units	MZ25	MZ50
Plate thickness	mm	0.99	1.01
Cladding thickness	mm	0.36	0.25
Meat thickness	mm	0.26	0.51
Meat width	mm	18.8	18.6
Meat longitude	mm	73.0	71.0
Meat density	g/cm^3	17.7	17.3
Total U	g	5.9	10.9
Meat U density	gU/cm^3	16.5	16.2
Ratio U/surface	gU/cm^2	0.21	0.41

Table 1. MZ25 and MZ50 characteristics. Miniplates size is 25 x 100 mm^2.

Miniplates MZ25 and MZ50 were irradiated 90 effective full power days (EFPD) during the RERTR-7A test experiment in the ATR. Local burn-ups of ^{235}U were between 28.5 and 53.3% for MZ25 and between 25.2 and 48.3% for MZ50. Average total burn-ups were 37.5 and 33.1% for MZ25 and MZ50, respectively. The estimated beginning of life (BOL) thermal conditions, operating parameters, peak surface heat flux, power density generated at the beginning and end of irradiation, minimum and maximum clad surface temperatures, fission density, internal and external temperatures, heat flux and total swelling were previously shown [43, 59–63].

3.4. Post-irradiation examination

The post irradiation examination (PIE) was performed at the Hot Fuel Examination Facility of the Material and Fuel Complex (INL) [58, 59]. Plate swellings were 3.6% for MZ25 and slightly higher than 4% for MZ50 miniplate. Meat swellings of 15 and 12% were measured for MZ25 and MZ50, in accordance with fission densities. The swelling is low and uniform and consistent with other monolithic UMo plates with aluminium cladding irradiated in previous experiments (RERTR-6 and RERTR-7) with similar burn-ups.

An eddy current probe (HELMUT FISCHER model Delta Scope MP30) modified for hot cell was used for measuring the oxide thickness. Zero calibration was done using nonirradiated Zry-4. The average oxide layer thickness after irradiation was 2.6 and 3.2 +/− 0.5 μm for miniplates MZ25 and MZ50, respectively.

Figure 19 shows a montage of metallographic images of MZ25 miniplate cut transversally and polished. The arrow indicates the direction of the ATR core center. At the nearer end, the neutron flux is higher and burn-up reached 53.3%. The burn-up gradient across the width of the plate was 1.85. **Figure 20** shows a higher magnification optical image of the UMo/Zry-4 irradiated interface with fuel and clad remaining adherent and with no evidence of fission gas bubbles.

Figure 19. Optical metallographic montage of a polished transversal cut of MZ25 fuel plate.

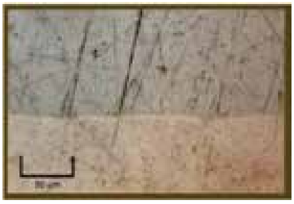

Figure 20. Metallographic cross-section of the interaction zone showing fuel (bottom) and clad (top) of MZ25 irradiated miniplate.

Figure 21 shows another high magnification optical image montage of the width end of plate MZ50 fuel/cladding interface plate that faces the ATR core centerline; a zone with the highest fission density rate and highest temperature with a 48.3% final burn-up. The width of the interaction layer between γ-U7Mo fuel and Zry-4 cladding is extremely thin and can hardly be seen. No fission gas bubbles were visible in the fuel, and the bonding between fuel and cladding is intact. The swelling is uniform.

Figure 21. Metallographic cross-section of a hot zone in MZ50 miniplate.

PIE reports in both miniplates states that the fuel/clad bonding looks excellent.

4. Discussion

4.1. HMD γ-U7Mo powder performance

Hydriding in the presence of stresses can be easily corroborated using two annealed probes of γ-U7Mo, one of which has been indented after the heat treatment with a Vickers hardness

http://dx.doi.org/10.5772/63652

tip. The beginning of hydriding can be noticed only at the indented probe after slow heating of both samples up to 300°C in a hydrogen atmosphere and slow cooling. Another way of obtaining stressed samples is by melting alloy buttons in an arc furnace with a refrigerated copper crucible. Also a stressed sample of γ-UMo can probably be cathodically charged filling with hydrogen the traps preparing the alloy for massive hydriding in an hydrogen atmosphere.

Microscopic fractures are produced during the hydriding of γ-U7Mo without producing a nanosized powder as it happens with the hydriding of pure uranium. The rate of hydrogen incorporation during massive hydriding of γ-U7Mo is greater than a square root dependence with temperature because of fragmentation of the material in the phase transformation. Hydrogen incorporation increases with pressure with no variation in the absorption temperature range. UMo samples with higher purity take less time for total hydride formation [64].

The vibrating chamber allowed many of the thermal treatments at temperatures above 500°C avoiding powder sintering. The vibration was connected during hydriding, dehydriding and passivation for moving the interior material, enhancing diffusion and increasing cooling rates for quenching the metastable gamma phase. Vibration was also used for testing different coverage techniques with surrogate and UMo particles.

The oxidation kinetics of γ-UMo alloy is lower than in pure uranium. The hydride can spontaneously burn at room temperature in air. The burning of the hydride is reduced after heating in vacuum at 325°C with the elimination of hydrogen in traps. In all experiments the temperature control was performed with a thermocouple immersed in the powder, allowing immediate control of hydriding (exothermic), dehydriding (endothermic) and passivation (exothermic) processes. Direct pressure control was achieved by maintaining the chamber closed, when possible; evolution of pressure can be directly correlated with hydrogen absorption and desorption. Powders of γ-U7Mo in contact with air diminish their density from one year to another evidencing surface oxidation and hitherto should be kept in inert atmosphere containers.

4.2. Performance of monolythic γ-UMo fuel with nonaluminum cladding

Special precautions must be taken to allocate UMo monolithic coupons in the frame with very small tolerances to avoid blistering formation during the lamination process. As usual, surface contaminations of any kind—in the assembling of the fuel coupon with the lids and frame, in the welding of the sandwich, in the cleaning of the casting molds, in the maintenance of fresh reactives, etc.—must be avoided. Colamination of monolythic UMo with Zry-4 or stainless steel used as cladding materials is performed at temperatures higher than 650°C where the gamma UMo high temperature phase is stable. No special precautions are needed to avoid decomposition at working temperatures and TTT diagrams are used only in the evaluation of final cooling velocities to retain the γ-UMo phase.

The different coefficients of thermal expansion of U7Mo and Zry-4 needed a special procedure of not allowing the cooling at intermediate steps of hot Colamination. When finally cooling to room temperature with 100% welded interfaces, the appearing stresses produced by differential contraction coefficients will be absorbed by elastic or plastic deformation of Zry-4; they probably disappear during final straightening and polishing or even during irradiation. No special treatment is needed and this is not an issue. In the case of stainless steel claddings, there is no great mismatch between thermal coefficients, and no problems are presented during hot colamination with monolithic UMo.

Nonaluminum monolithic fuel plates need to be straightened after hot lamination. More power machinery than with aluminum dispersed fuel plates is needed. The oxide layer of the Zry-4 cladding after hot colamination could only be removed by mechanical means. Since sand blasting must be done in an inert atmosphere, wet sand papers were used semimanually. In the case of stainless steel claddings the polishing can be assisted with chemical means. A more industrialized polishing can be performed using a scanning abrasive water blasting that can follow small surface deformations maintaining uniform cladding thickness. Also abrasive powders assisted by brushes can be used.

Nonaluminum claddings in UMo monolithic fuels can be smaller than 150 μm [9]. MZ50 miniplate had a cladding thickness of 250 μm and a total plate thickness of 1 mm. This cladding reduction thickness can compensate lower thermal conductivity, compared with aluminum alloys, in heat extraction. The reduction of cladding and fundamentally plate thickness can help in new designs introducing a more satisfactory adjustment of neutron moderation ratios.

The growth kinetics of oxide layer in Zry-4 and stainless steel claddings during irradiation is much lower than in aluminum claddings. The lids and frame process of monolithic γ-UMo with nonaluminum cladding using the lids and frame hot colamination fabrication process can be scaled up to full size plates.

5. Conclusions

The development of the HMD process was carried out with the production of more than 5 kg of γ-UMo powder. Basic research is still needed to study thermodynamic properties of the just discovered hydride. Equilibrium stoichiometry, hydrogen allocation in traps and interstitial positions need more elaborated studies. Scalability of the HMD UMo powder production using enriched uranium is possible up to mass batches compatible with security standards, requiring low man-power and equipment investment.

Many coverage techniques can be applied to UMo particles with different objectives and results. There is a great versatility of methods that have not all been tested under irradiation, but it seems that more focused research is needed.

The traditional picture and frame technique for the fabrication of monolithic γ-UMo plates can be used if aluminum cladding is replaced by Zircaloy-4 or AISI 304L. This is a flexible and practical production scale technology that can be used for fuels with densities greater than 17 gU/cm^3. Monolithic γ-U7Mo with Zry-4 cladding miniplates irradiated up to 50% burn up show, in PIE results, a gentle interaction zone without bubble nucleation. The monolithic UMo coupon can be fabricated from powder, with the possibility of blending burnable poisons, inert powders, gas adsorption materials, and conforming special geometrical shapes.

Conversion of high flux reactors from HEU to LEU can be done using UMo monolithic fuel technology. Usual equipment can be used with small modifications for fuel fabrication at industrial scale. Other benefits can probably be achieved by thorough evaluation of the fuel cycle up to the analysis of back end options that can bring some other benefits. Reduction in cladding and plate thickness can open the door for new designs and HEU-LEU conversion possibilities.

Author details

Enrique E. Pasqualini*

Address all correspondence to: pascua@cnea.gov.ar

Sabato Institute (UNSAM/CNEA). Nuclear Nanotechnology Laboratory, Constituyentes
Atomic Center, Argentina

References

[1] Nuclear Power Reactors in the World. Reference Data Series No 2. 2015 Edition. IAEA. http://www-pub.iaea.org/MTCD/Publications/PDF/rds2-35web-85937611.pdf and https://www.iaea.org/pris/

[2] Handbook of Nuclear Engineering. Editor Dan Gabriel Cacuci. Springer Science +BusinessMedia LLC (2010). http://www.springer.com/us/book/9780387981307

[3] Research Reactor Data Base. IAEA (2009). https://nucleus.iaea.org/RRDB/RR/ReactorSearch.aspx

[4] Personal communication with F. M. Marshall of the Research Reactor Section, International Atomic Energy Agency.

[5] L. Kowarski. Report on Research Reactors. Proceedings of the International Conference on the Peaceful Uses of Atomic Energy. Vol. II, 233–247. Geneva (1955).

[6] J. R. Huffman. The Materials Testing Reactor. Nucleonics, 12, 20–26 (1954).

[7] J. E. Cunningham and E. J. Boyle. MTR-Type Fuel Elements. Proceedings of the International Conference on the Peaceful Uses of Atomic Energy. Vol. IX, 203–207. Geneva (1955).

[8] C. E. Weber and H. H. Hirsch. Dispersion Type Fuel Elements. Proceedings of the International Conference on the Peaceful Uses of Atomic Energy. Vol. IX, 196–202. Geneva (1955).

[9] J. Howe. The Metallurgy of Reactor Fuels. Proceedings of the International Conference on the Peaceful Uses of Atomic Energy. Vol. IX, 179–195. Geneva (1955).

[10] O. J. Wick, T. C. Nelson and M. D. Freshley. Plutonium Fuels Development. Proceedings of the International Conference on the Peaceful Uses of Atomic Energy. Vol. VI, 700–709. Geneva (1955).

[11] A. M. Weinberg, T. E. Cole and M. M. Mann. The MTR and Related Research Reactors. Proceedings of the International Conference on the Peaceful Uses of Atomic Energy. Vol. II, 402–419. Geneva (1955).

[12] C. B. Waff. Administration pushes alternative nuclear fuel cycles. Phys. Today 32, 2, 85 (1979). http://scitation.aip.org/content/aip/magazine/physicstoday/article/32/2/10.1063/1.2995433

[13] RERTR, Reduced Enrichment for Research and Test Reactors. US DOE.http://www.rertr.anl.gov/

[14] J. P. Schwartz. Uranium Dioxide Caramel Fuel. An Alternative Fuel Cycle for Research and Test Reactors. International Conference on Nuclear Non-Proliferation and Safeguards. New York (1978). https://www.oecd-nea.org/science/docs/1978/neacrp-l-1978-214.pdf

[15] Research Reactor Core Conversion. From the Use of Highly Enriched Uranium to the Use of Low Enriched Uranium Fuels. Guidebook. Technical Document, IAEA (1980). http://www-pub.iaea.org/MTCD/publications/PDF/te_233_web.pdf

[16] T. D. Ippolito Jr. Effects of Variation of Uranium Enrichment on Nuclear Submarine Reactor Design. MIT, USA (1990). http://fissilematerials.org/library/ipp90.pdf

[17] A. G. Samoilov, A. I. Kashtanov and V. S. Volkov. Dispersion-Fuel Nuclear Reactor Elements. Atomizdat, Moskva 1965. Translated from Russian, Jerusalem (1968).

[18] G. L. Hofman, J. Rest, and J. T. Snelgrove. Comparison of Irradiation Behavior of Different Uranium Silicide Dispersion Fuel Element Designs. International Meeting on Reduced Enrichment for Research and Test Reactors. Williamsburg, Virginia, USA (1994). http://www.osti.gov/scitech/servlets/purl/10107567/

[19] NUREG 1313. Safety Evaluation Report Related to the Evaluation of Low-Enriched Uranium Silicide-Aluminum Dispersion Fuel for Use in Non-Power Reactors. U.S. Nuclear Regulatory Commission Office of Nuclear Reactor Regulation (1988). https://www.iaea.org/OurWork/ST/NE/NEFW/Technical-Areas/RRS/documents/mo99/NUREGfuelexp1988.pdf

[20] K. H. Kim, D. B. Lee, Ch. K. Kim, I. H. Kuk and K. W. Paik. Characteristics of U3Si and U3Si2 Powders Prepared by Centrifugal Atomization. J. Nucl. Sci. Technol. 34, 12, 1127–1132 (1997).

[21] J. L. Snelgrove, G. L. Hofman, C. L. Trybus, and T. C. Wiencek. Development of Very-High Density Fuel by the RERTR Program. International Meeting on Reduced Enrich-

ment for Research and Test Reactors. Republic of Korea (1996). http://www.rertr.anl.gov/FUELS96/SNELGR96.PDF

[22] Good Practices for Qualification of High Density Low Enriched Uranium Research Reactor Fuels. IAEA Nuclear Energy Series N° NF-T-5.2 (2009). http://www-pub.iaea.org/MTCD/publications/PDF/pub1400_web.pdf

[23] G. L. Hofman and M. K. Meyer. Design of High Density Gamma-Phase Uranium Alloys for LEU Dispersion Fuel Applications. International Meeting on Reduced Enrichment for Research and Test Reactors. Brazil (1998). http://www.rertr.anl.gov/Fuels98/GHofman.pdf

[24] M. K. Meyer, G. L. Hofman, J. L. Snelgrove, C. R. Clark, S. L. Hayes, R. V. Strain, J. M. Park and K. H. Kim. Irradiation Behavior of Uranium-Molybdenum Dispersion Fuel: Fuel Performance Data from RERTR-1 and RERTR–2. International Meeting on Reduced Enrichment for Research and Test Reactors. Budapest, Hungary (1999). http://www.rertr.anl.gov/Web1999/PDF/09Meyer99.pdf

[25] S. Van den Bergue, W. Van Renterghem and A. Leenaers. Transmission Electron Microscopy Investigation of Irradiated U-7 wt% Mo Dispersion Fuel. International Meeting on Reduced Enrichment for Research and Test Reactors. Prague, Czech Republic (2007). http://www.rertr.anl.gov/RERTR29/PDF/13-2_VandenBerghe.pdf

[26] G. L. Hofman, M. K. Meyer and A. E. Ray. Design of High Density Gamma-Phase Uranium Alloys for LEU Dispersion Fuel Applications. International Meeting on Reduced Enrichment for Research and Test Reactors. Sao Paulo, Brazil (1998). http://www.rertr.anl.gov/Fuels98/GHofman.pdf

[27] R. J. Van Thyne and D. J. McPherson. Transformation Kinetics of Uranium-Molybdenum Alloys. Transactions of the American Society for Metals, 49, 598–619 (1957).

[28] J. M. Hamy, F. Huet, B. Guigon, P. Lemoine, C. Jarousse, M. Boyard and J. L. Emin. Status as of October 2003 of the French UMo Group Development Program. International Meeting on Reduced Enrichment for Research and Test Reactors. Chicago, Illinois, USA (2003). http://www.rertr.anl.gov/RERTR25/PDF/Lemoine.pdf

[29] G.L. Hofman, Y.S. Kim, M.R. Finlay and J.L. Snelgrove. Recent Observations at the Postirradiation Examination of Low-Enriched U-Mo Miniplates Irradiated to High Burnup. International Meeting on Reduced Enrichment for Research and Test Reactors. Chicago, Illinois, USA (2003). http://www.rertr.anl.gov/RERTR25/PDF/Hofman.pdf

[30] P. Lemoine, J. L. Snelgrove, N. Arkhangelsky and L. Alvarez. UMo Dispersion Fuel Results and Status of Qualification Programs. International Topical Meeting on Research Reactor Fuel Management (RRFM). München, Germany (2004). http://www.iaea.org/inis/collection/NCLCollectionStore/_Public/35/036/35036191.pdf

[31] G. L. Hofman, M. R. Finlay and Y. S. Kim. Post-Irradiation Analysis of Low Enriched U-Mo/A1 Dispersions Fuel Miniplate Tests, RERTR 4 & 5. International Meeting on

Reduced Enrichment for Research and Test Reactors. Vienne, Austria (2004). http://www.rertr.anl.gov/RERTR26/pdf/10-Hofman.pdf

[32] T. C. Wiencek and I. G. Prokofiev. Low-Enriched Uranium-Molybdenum Fuel Plate Development. International Meeting on Reduced Enrichment for Research and Test Reactors. Las Vegas, Nevada, USA (2000). http://www.rertr.anl.gov/Web2000/PDF/Wien00.pdf

[33] C. R. Clark, S. L. Hayes, M. K. Meyer, G. L. Hofman and J. L. Snelgrove. Update on U-Mo Monolithic and Dispersion Fuel Development. International Topical Meeting Research Reactor Fuel Management. München, Germany. 41–45 (2004). http://www.euronuclear.org/pdf/RRFM%202004%20Session%202.pdf

[34] G. A. Moore, B. H. Rabin, J. F. Jue, C. R. Clark, N. E. Woolstenhulme, B. H Park, S. E. Steffler, M. D. Chapple, M. C. Marshall, J. J. Green, and B. L. Mackowiak. Development Status of U10Mo Monolithic Fuel Foil Fabrication at the Idaho National Laboratory. International Meeting on Reduced Enrichment for Research and Test Reactors. Lisbon, Portugal (2010). http://www.rertr.anl.gov/RERTR32/pdf/S12-P1_Moore.pdf

[35] S. Van Den Berghe, A. Leenaers, E. Koonen and L. Sannen. From high to low enriched uranium fuel in research reactors. Adv. Sci. Technol. 73, 78–90 (2010). http://www3.sckcen.be/microstructure/Research/VA-ASCT-10.pdf

[36] C. R. Clark, B. R. Muntifering, and J. F. Jue. Production and Characterization of Atomized U-Mo Powder by the Rotating Electrode Process. International Meeting on Reduced Enrichment for Research and Test Reactors. Prague, Czech Republic (2007). http://www.rertr.anl.gov/RERTR29/PDF/15-2_Clark.pdf

[37] C. R. Clark, M. K. Meyer and J. T. Strauss. Fuel Powder Production from Ductile Uranium Alloys. International Meeting on Reduced Enrichment for Research and Test Reactors. Sao Paulo, Brazil (1998). http://www.iaea.org/inis/collection/NCLCollectionStore/_Public/35/040/35040232.pdf

[38] S. Balart, P. Bruzzoni, M. Granovsky, L. Gribaudo, J. Hermida, J. Ovejero, G. Rubiolo and E. Vicente. U-Mo alloy powder obtained by a hydride-dehydride process. International Meeting on Reduced Enrichment for Research and Test Reactors. Las Vegas, Nevada, USA (2000). http://www.rertr.anl.gov/Web2000/PDF/Balar00.pdf

[39] M. I. Solonin, A. V. Vatulin, Y. A. Stetsky, Y. I. Trifonov and B. D. Rogozkin. Development of the Method of High Density Fuel Comminution by Hydride-Dehydride Processing. International Meeting on Reduced Enrichment for Research and Test Reactors. Las Vegas, Nevada (2000). USA. http://www.rertr.anl.gov/Web2000/PDF/Vatu00.pdf

[40] W. D. Wilkinson. Uranium Metallurgy. Interscience Publishers. John Wiley and Sons Inc. New York (1962).

[41] G. L. Powell. Solubility of hydrogen and deuterium in a uranium-molybdenum alloy. J. Phys. Chem., 80 (4), 375–381 (1976).

[42] E. E. Pasqualini, J. Helzel Garcia, M. López, E. Cabanillas and P. Adelfang. Powder Production of U-Mo Alloy, HMD Process. (Hydriding-Milling-Dehydriding). International Topical Meeting on Research Reactor Fuel Management. Ghent, Belgium. 183–187 (2002). http://www.euronuclear.org/meetings/rrfm/pdf/RRFM%202002.pdf

[43] E. E. Pasqualini. Alternative processes of comminution and colamination of uranium molybdenum alloys. Prog. Nucl. Energy. 75, 92–104 (2014).

[44] E. E. Pasqualini, M. López and A. Gonzalez. Set Up of U-Mo Powder Production by HMD Process. International Meeting on Reduced Enrichment for Research and Test Reactors. Vienne, Austria (2004). http://www.rertr.anl.gov/RERTR26/pdf/P11-Pasqualini.pdf

[45] M. Chen, X. Yi-fu, W. Jing, J. Jia and P. Zhang. Characterization of γ-U–10 wt.% Mo alloy powders obtained by hydride-milling-dehydride process. J. Nucl. Mat. 400, 1, 69–72 (2010).

[46] R. M. Leal Neto, C. J. Rocha, E. Urano de Carvalho, H. G. Riella and M. Durazzo. Investigation of powdering ductile gamma U-10 wt% Mo alloy for dispersion fuels. J. Nucl. Mat. 445, 218–223 (2014).

[47] H. J. Goldschmidt. Interstitial alloys. Butterworths, London (1967).

[48] International Tables for Crystallography. Volume A: Space-Group Symmetry. Editor Theo Hahn, Fifth Edition (2002). ISBN-13: 978-0792365907

[49] E. E. Pasqualini. Advances and Perspectives in U-Mo Monolithic and Dispersed Fuels. International Meeting on Reduced Enrichment for Research and test Reactors. Cape Town, Republic of South Africa (2006). http://www.rertr.anl.gov/RERTR28/PDF/S6-4_Pasqualini.pdf

[50] E. E. Pasqualini and M. Lopez. Increasing the Performance of U-Mo Fuels. International Meeting on Reduced Enrichment for Research and Test Reactors.Vienna, Austria. 2004. http://www.rertr.anl.gov/RERTR26/pdf/23-Pasqualini%20II.pdf

[51] E. E. Pasqualini. Dispersed (Coated Particles) and Monolithic (Zircaloy-4 Cladding) U-Mo Miniplates. International Meeting on Reduced Enrichment for Research and Test Reactors. Boston, USA (2005). http://www.rertr.anl.gov/RERTR27/PDF/S15-3_Pasqualini.pdf

[52] S. Van Den Berghe, A. Leenaers and C. Detavernier. Selenium Fuel: Surface Engineering of U(Mo) Particles to Optimise Fuel Performance. International Topical Meeting on Research Reactor Fuel Management. Marrakech, Morocco. 26–34 (2010). http://www.euronuclear.org/meetings/rrfm2010/transactions/RRFM2010-transactions-s2.pdf

[53] M. Boulos. New frontiers in thermal plasmas from space to nanomaterials. Nucl. Eng. Technol. 44, 1, 1–8 (2012). http://www.kns.org/jknsfile/v44/JK0440001.pdf

[54] E. E. Pasqualini. Monolithic γ-UMo Nuclear Fuel Plates with Non Aluminium Cladding. International Meeting on Research Reactor Fuel Management. Hamburg, Germany. 67–72 (2008). http://www.euronuclear.org/meetings/rrfm2008/transactions/rrfm2008-session2.pdf

[55] J. Rest, Y. S. Kim, G. L Hofman, M. K. Meyer and S. L. Hayes. U-Mo Fuels Handbook. ANL-09/31 (2009).

[56] H. J. Snyder. Fuel-Clad Bond Testing of Zircaloy-2 Clad, Uranium-12 w/o Molybdenum Fuel Rods. OSTI: 4348214. Report Number(s): WAPD-141. DOE Contract Number: AT-11-1-GEN-14. Feb 15 (1956).

[57] J. E. Garcés and G. Bozzolo. Atomistic Simulation of High-Density Uranium Fuels. Sci. Technol. Nucl. Instal. 2011, 16 (2011); Article ID 531970. http://www.hindawi.com/journals/stni/2011/531970/

[58] A. B. Robinson and M. R. Finlay. RERTR-7 Post Irradiation Examination (PIE) Letter Report. INL/EXT-07-13271. Sep. 2007.

[59] D. M. Perez, M. A. Lillo, G. S. Chang, G. A. Roth, N. E. Woolstenhulme and D. M. Wachs. RERTR-7 Irradiation Summary Report. INL/EXT-11-24283. Dec. 2011.

[60] D. M. Wachs, R. G. Ambrosek, G. S. Chang and M. K. Meyer. Design and Status of RERTR Irradiation Tests in the Advanced Test Reactor. International Meeting on Reduced Enrichment for Research and Test Reactors. Cape Town, Republic of South Africa (2006). http://www.rertr.anl.gov/RERTR28/PDF/S9-3_Wachs.pdf

[61] G. S. Chang and M. A. Lillo, "RERTR-7A As-Run Physics Analysis and Test Train Isocoveres Radiological Characterization Versus Cooling Time," EDF-6857, rev.2, INL, 2007.

[62] A. B. Robinson, G. L. Chang, D. D. Keiser, Jr., D. M. Wachs and D. L. Porter. Irradiation Performance of U-Mo Alloy Based Monolithic Plate-type Fuel – Design Selection. INL/EXT-09-15903, Rev 0 (to be published).

[63] A. Denis and A. Soba. Placa/Dplaca Simulation of Monolithic/Disperse UMo Plates. International Topical Meeting Research Reactor Fuel Management. Lyon, France. 96–100 (2007). http://www.euronuclear.org/meetings/rrfm2007/transactions/rrfm2007-transactions-postersession.pdf

[64] R. Van Houten. Selected engineering and fabrication aspects of nuclear metal hydrides (Li, Ti, Zr, and Y). Nucl. Eng. Design. 31, 434–448 (1974).

Dedicated Monte Carlo Procedures Applied in Gamma-ray Spectrometry Used in Decommissioning of Nuclear Facilities

Daniela Gurau

Additional information is available at the end of the chapter

http://dx.doi.org/10.5772/62937

Abstract

Because the experimental efficiency calibration is limited to several measurement geometries and cannot be applied directly to all measurement configurations, the efficiency transfer method for the efficiency computation was applied using ETNA software. An approach using efficiencies measured with point sources combined with theoretical procedures was applied for obtaining the peak efficiency $\varepsilon(E)$ for disk sources measured with a NaI(Tl) detector. The transfer method was applied for the computation of the efficiency of an HPGe detector using as a reference a point source placed at 10 cm height from the face of the detector. The method was applied both for point sources and volume sources with varied compositions and densities. To correct the experimental values of the efficiencies, coincidence summing effects were evaluated using GESPECOR Monte Carlo code. The study of the response function characterization of the ISOCART and Segmented Gamma Scanner WS1100 gamma-ray spectrometry systems was related. GEANT 3.21 Monte Carlo code was used to simulate the spectra expected to be obtained for the photon energy range from 50 to 2000 keV. A big volume represented by a 220l cylindrical source was considered to be measured with the two systems. The full energy peak efficiency and the total efficiency were evaluated.

Keywords: gamma-ray spectrometry, Monte Carlo simulations, NaI(Tl) and HPGe detectors, efficiency transfer, radioactive waste assay

1. Introduction

The decommissioning of nuclear facilities is a topic of great interest to many Members States of IAEA because a large number of facilities have to be retired from service. The term "decommissioning" is defined in the TRS 267 [1] as actions taken at the end of a facility useful life to retire the facility from service in a manner that provides adequate protection for the health and safety of the workers, public and environment. It is a complex process because it involves many operations such as detailed survey, decontamination and dismantling of power plant equipment and facilities, buildings and structure demolition, and managing the resulting waste and other materials that need to be taken into consideration, due to their effects on health and safety of the operating personnel, public and the environment. The decommissioning activities have expanded in the last years all over the world because many nuclear installations have been exhausting their lifetime. Careful planning and management are essential to ensure that decommissioning is fulfilled in a safe and cost-effective manner. A right evaluation of the radioactivity is very important affecting directly the starting point of the decommissioning process. This can be the reason for unwanted delays between stages.

The characterization of the radioactive inventory in decommissioning wastes is described in TRS 267 [1] as a front-end task required to define the operational decommissioning plan and estimate costs and radiological risks associated with the plan. Once the decommissioning process is under way, regulatory, safety and waste disposal considerations require that the radioactive waste should be monitored and characterized. The objective of this characterization is to ensure that the waste will be handled and disposed of in a safe and economic manner. The methods and equipment used to characterize the radioactive waste resulted from decommissioning vary considerably, depending upon the type and complexity of the facility and the radionuclide mix from the plant.

The work detailed in this chapter explores the specific gamma-ray spectrometry phenomena in different work conditions, relating the analysis, development and implementation in the radioactive waste management of specific investigation methods for gamma-ray spectrometry measurements that will produce reasonable measurement uncertainties [2] with lower cost and relatively short duration of data acquisition. The applicability and functionality of gamma-ray spectrometry methods to radiological characterization and free release of radioactive waste materials are presented, using experimental methods that are mostly combined with theoretical and simulation procedures using Monte Carlo computer codes.

2. Efficiency transfer in gamma-ray spectrometry

Because more and more nuclear installations reach the end of their life, the dismantling and decommissioning processes of them became a key topic in the nuclear industry. The radiological characterization of the systems, structures, equipment, components and the environment represents a basic phase in the decommissioning process because allow the definition of the decommissioning strategy. This task is very important because it provides the basis for the correct classification of various types of waste, which in turn affects the decommissioning solution and the associated costs. The measurement method should be reliable and efficient. In addition, it should be flexible, able to provide proper results for the diversity of samples assessed with different compositions and densities, different shapes and possibly non-uniform activity distribution. The appropriate efficiency calibration in the deprived conditions is a challenging task.

The experimental calibration of germanium detectors used in gamma-ray spectrometry [3] is difficult to achieve particularly for the geometry measurement that cannot be estimated as a point source. Therefore, when different samples with varies composition and densities are measured in various geometries, a large number of standards need to be measured to carry out the detection efficiency according to a specific sample matrix and geometry. The situation is more difficult in the case when the samples are measured with high efficiency detectors and the sample is placed close to detector, because in this case most radionuclides will give rise to important coincidence summing effects [4]. Consequently, the detection efficiency for a given energy depends not only on energy and experimental setup, but also on the radionuclide. The knowledge of the detection efficiency, which varies strongly with the source to detector distance, due to the geometry and absorption factors, is essential for operating these systems. Therefore, a comprehensive experimental calibration would require the measurement of a big number of standards, one for each geometry and matrix of interest, containing certified activities for each radionuclide that is present in the real samples. A better solution for determining the detection efficiency is the application of specific methods of calculation. In the gamma-ray spectrometry field, except the simulations performed for the calculation of the detection efficiencies, Monte Carlo simulation codes can also be used to evaluate the transfer factors [5]. Based on its relative sensitivity to the uncertainties of the detector parameters and of the calculation model, the method of efficiency transfer [6, 7], based on Monte Carlo simulation or on semi-empirical methods [6, 8, 9], is more and more relevant to evaluate the efficiency whenever direct experimental calibration is not accessible [10].

The applicability of the ETNA (Efficiency Transfer for Nuclide Activity) software to compute the efficiency transfer factors for various counting geometries used in routine laboratory measurements was examined. Thus, ETNA results were compared with experimental results (corrected for coincidence summing effects) [10, 11]. The detection efficiencies were calculated for NaI(Tl) and HPGe detectors. An approach using the experimental efficiency measured with point sources combined with theoretical procedures was applied for obtaining the peak efficiency $\varepsilon(E)$ for disk sources measured with NaI(Tl) detector. Using the detection efficiencies for a reference point source geometry located at 10 cm distance from the high purity germanium (HPGe) detector, the applicability of the efficiency transfer method was checked once more.

2.1. The efficiency calibration of the detectors using experimental measurements

For the efficiency evaluation of the disk sources, the measurements were made with an Ortec gamma-ray spectrometry system consisting of a ScintiPack Photomultiplier Base with Preamplifier and High Voltage Supply type 296 and a DigiDART Digital Portable Multichannel Analyzer and lead collimator. The NaI(Tl) detector specifications are as follows: the diameter of the end cap of the detector is 3 × 3 inches, the crystal diameter is 8 cm, and the energy resolution is 70.62 keV at 1332 keV (^{60}Co). The recommended operating bias is +1000 V.

The second Ortec gamma-ray spectrometry system used in this study for the examination of the applicability of the efficiency transfer method consisted of a high purity germanium detector, model GMX50P4, transplantable in Pop Top technology, with dimensions: 6.46 cm diameter, 7.5 cm length, 0.05 cm beryllium absorber layer and a Digital Portable Multichannel Analyzer type DigiDART. The main performance specifications of the HPGe warranted by the producer are presented in **Table 1**.

Resolution (FWHM) at 1.33 MeV, ^{60}Co	**2.2 keV**
Peak-to-Compton ratio, ^{60}Co	58:1
Relative efficiency at 1.33 MeV, ^{60}Co	50%
Peak shape (FWTM/FWHM), ^{60}Co	2.0
Resolution (FWHM) at 5.9 keV, ^{55}Fe	800 eV
Recommended operating bias, negative	3300 V

Table 1. HPGe performance specifications.

In the first step, certified standard point sources were used to evaluate the detector experimental efficiencies as a function of gamma-ray energies [3], for the NaI(Tl) detector.

The sources were measured in horizontal plane, at radial distances r = 0, 1, 2, 3 and 4 cm from the detector axis and at 0.8 cm from the face of the NaI(Tl) detector. A lead collimator was used in the measurements. Five sets of data were obtained for all the important gamma line involved in the study. From the graphic representation (**Figure 1**), it can be seen that the experimental efficiencies $\varepsilon(E)$ for the NaI(Tl) detector do not present a smooth variation with the energy E.

In the case of the HPGe detector, the experimental detection efficiencies were evaluated for the detector-point sources distances of 2, 5, 10, 15 and 20 cm. The counting dead time of the measurements was in general controlled to be less than 7% and consequently corrected during the counting. The amplifier time constant was fixed to 12 μs. Cylindrical sources (**Table 2**) were also measured at 0, 1, 2 cm from the face of the HPGe detector. The counting dead time for these sources was less than 3%.

Radionuclide	**H (cm)**	**D (cm)**	**ρ (g/cm^3)**	**Λ (Bq)**	**u (%) (1σ)**
^{134}Cs	3.2	7.4	1.0	1916	2.5
^{137}Cs	3.3	7.4	1.4	1190	3.5

Table 2. Cylindrical sources.

^{134}Cs and ^{137}Cs radioactive sources were used to test the applicability of ETNA software for volume sources. Water and soil matrix have been chosen because they are most common in gamma-ray spectrometry laboratory.

The directly measured efficiency calibration curves obtained for the HPGe detector are represented in **Figure 1**. Was observed that the experimental efficiencies values $\varepsilon(E)$ for the HPGe detector do not present a smooth variation with the energy, E.

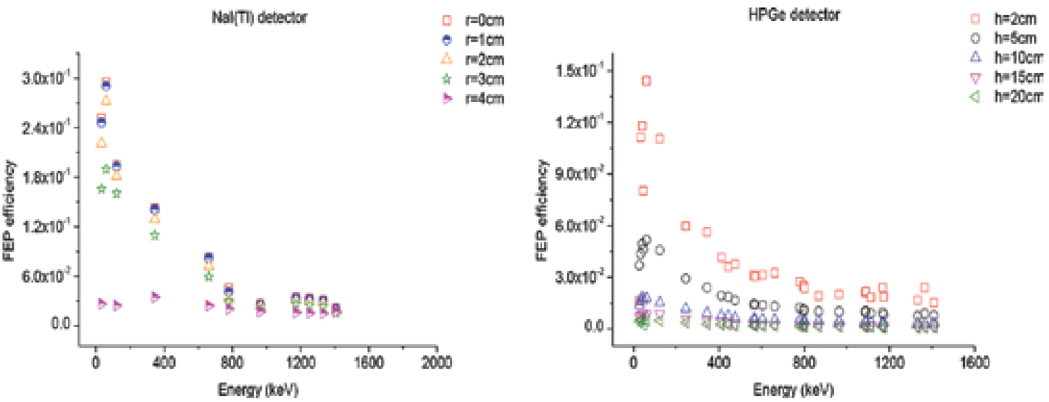

Figure 1. The experimental values of the detection efficiencies for point sources measured with the NaI(Tl) and HPGe detectors.

The uncertainties (1σ) of the experimental efficiencies values were estimated using ISO standard [12] using uncertainties of the activities from the certificates and the uncertainties of the counting results. The values were up to 11% for r= 0, 1, 2, 3 and 4 cm distances from the NaI(Tl) symmetry axis and up to 3% for h = 2, 5 and 10 cm and up to 8% for h = 15 and 20 cm source-to-detector distances in the case of the HPGe detector.

2.2. Coincidence summing corrections

The origin of the efficiency data deviation from smooth curves as a function of energy is due to the presence of significant coincidence summing effects in the case of ^{152}Eu, ^{134}Cs and ^{60}Co sources [10, 11]. To remove the effects of coincidence summing, specific corrections were evaluated and applied to experimental efficiencies for the purpose to obtain useful efficiency curve. To evaluate the coincidence summing effects, it represents a difficult task, mainly when the nuclides present complex decay schemes. To obtain the correct efficiencies values for the ^{152}Eu energy lines, the peak and total efficiencies are required for the energies of supplementary photons emitted by ^{152}Eu nuclide. For instance, in the case of the peak with energy E = 121.78 keV, only coincidence losses are feasible. The process is produced when any photon from the 71 photons list is emitted instantaneously with the photon with E = 121.78 keV and together interacts with the detector. These photons span an energy range from χ-ray to E = 1647 keV, and therefore, the total efficiency for the energy in this range is needed. For the peak with E = 1408.01 keV, 21 moistures of various photons are possible and can contribute to sum peak effects. To evaluate the coincidence summing effects for the E = 1408.01 keV, the peak efficiency for all these photons is required.

A method available to correct these effects is the Monte Carlo method. A dedicated software called GESPECOR [6] has been applied, in order to evaluate the coincidence summing corrections. This is user-friendly Monte Carlo software useful for the computation of the efficiency [3], of matrix effects [13] and of coincidence summing corrections [4] in gamma-ray spectrometry with HPGe detectors.

Because GESPECOR is dedicated to germanium detectors, the code cannot be directly applied for NaI(Tl) detector. Therefore, in the case of NaI(Tl) detector, the coincidence summing correction factors have been evaluated using an iterative procedure. Both the decay scheme data evaluated by GESPECOR and the experimental values of the peak and of the total efficiencies for the point source measurements were needed. The procedure followed in the first iteration is represented in **Figure 2**.

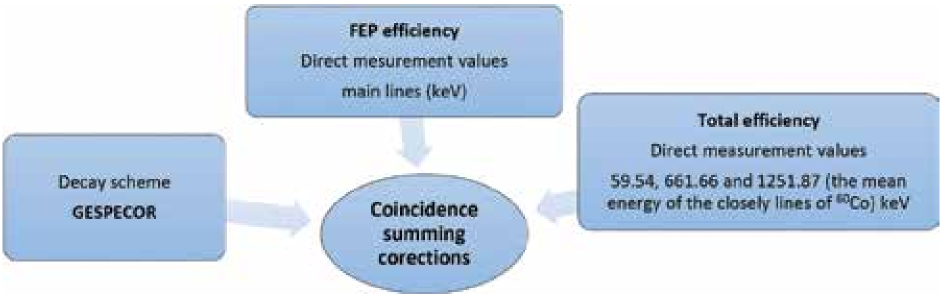

Figure 2. Procedure for coincidence summing correction factors evaluation

Taking into account that the ratio between the peak and total efficiency is a smooth function of energy, a first estimate of the total efficiency as a function of energy was obtained (**Figure 3**). This was possible even if only few directly measured total efficiency data were available.

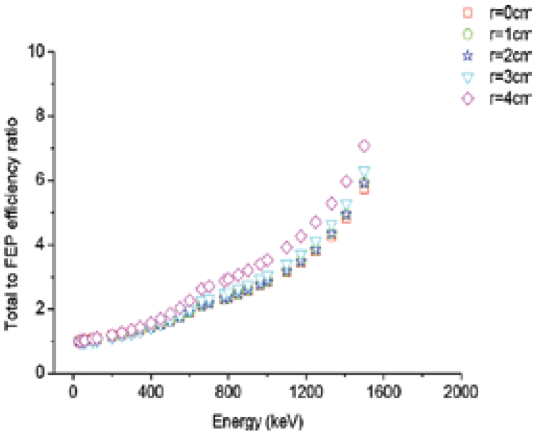

Figure 3. The experimental ratio of total to peak efficiency versus the energy for the NaI(Tl) detector.

The obtained values of the peak and total efficiencies were used to calculate the coincidence summing correction factors in the first iteration. The correction factors were subsequently used to obtain improved values of the peak efficiencies for the NaI(Tl) detector (second iteration). The peak and total efficiencies values resulted in the second iteration obtained using the similar procedure followed in the first interation procedure used to evaluate the coincidence summing correction factors in the second iteration. Was observed that it was not necessary to proceed in a higher order iterations. The final values obtained for the peak efficiencies of the NaI(Tl) detector were achieved from the measured values of the peak efficiencies and the coincidence summing correction factors in the second iteration. In **Figure 4** are represented the detection efficiencies for point sources measured in horizontal plane at 0.8 cm from the end face of the detector, corrected for the effects of coincidence summing for NaI(Tl) detector, only for *r* = 0, 2, 4 cm.

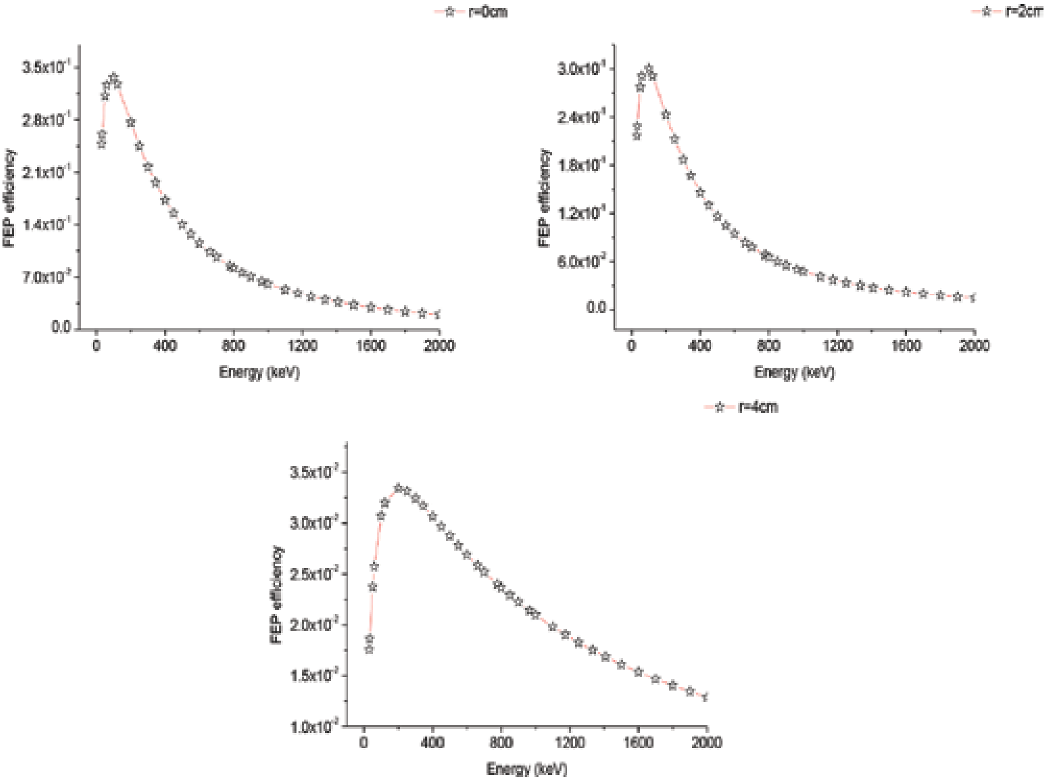

Figure 4. The detection efficiency corrected for the effects of coincidence summing for NaI(Tl) detector.

In the case of HPGe detector, the coincidence summing effects are presented in the case of ^{152}Eu, ^{134}Cs and ^{60}Co sources. Specific coincidence summing corrections were applied to the experimental efficiencies in order to obtain a generally useful efficiency curves for the HPGe detector. The values included in the HPGe detector manufacturer's data were used in computation as input detector data. The computed correction factors were subsequently used to obtain improved values of the peak efficiencies. In the case of cylindrical sources, the corrections were necessary only for ^{134}Cs gel matrix. The detection efficiency curves (corrected for the effects of coincidence summing) in function of energy for the five source-to-HPGe detector distances obtained for the peak efficiency for point sources are represented in **Figure 5** only for h = 2, 10, 20 cm.

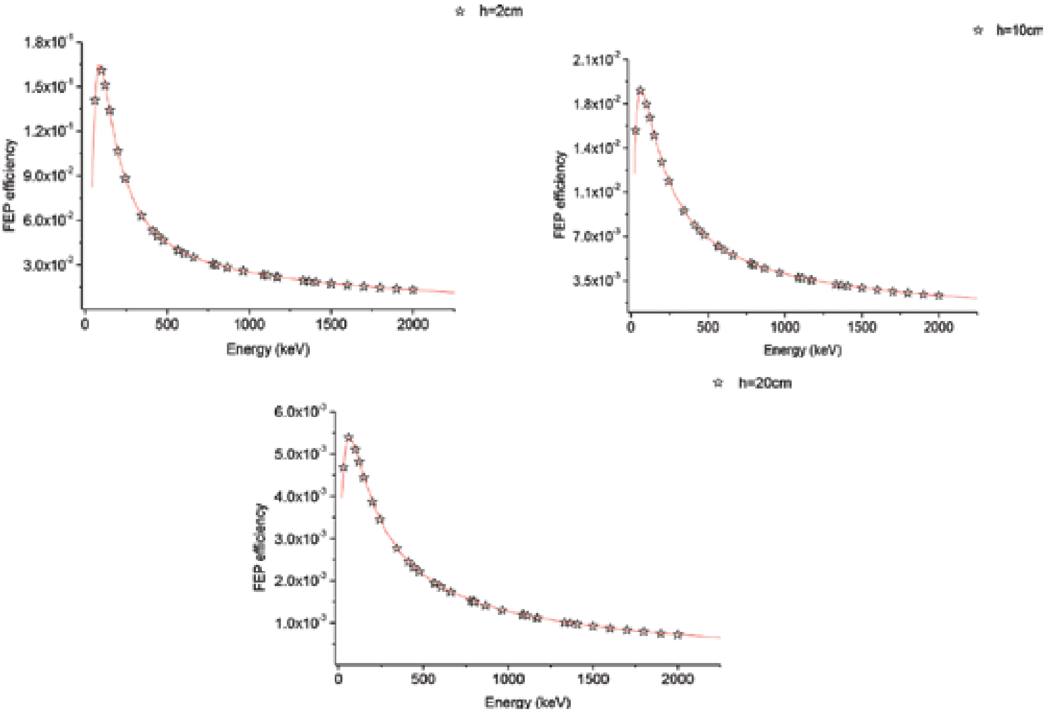

Figure 5. The detection efficiency corrected for the effects of coincidence summing for HPGe detector.

The efficiencies for the point sources obtained in this way for the reference measurement geometry (10 cm source-to-HPGe detector distance) could be used to evaluate the efficiency for other measurement geometries by the efficiency transfer method.

The uncertainties (1 σ) of the corrected efficiencies for point sources were up to 3% for NaI(Tl) detector and up to 3.5% for $\boldsymbol{h}$ = 2, 5 and 10 cm and 8.5% for $\boldsymbol{h}$ = 15 and 20 cm for HPGe detector. The uncertainties of the corrected efficiencies for cylindrical sources include additional uncertainties of the matrix effects; the resulting values were up to 8% (1σ).

2.3. The efficiency transfer

The gamma-ray spectrometry method is a relative method, necessitating standard radioactive sources for the efficiency calibration. When the standard source and the sample are the same, the next relation is applied for the computation of the activity of the sample:

$$\Lambda_p(E) = \Lambda_e(E)\frac{R_p(E)}{R_e(E)} \tag{1}$$

where $\Lambda_p(E)$ and $R_p(E)$ are the activity and the count rate for the sample, and $\Lambda_e(E)$ and $R_e(E)$ are the activity and the count rate for the standard source corresponding to the peak with energy E.

In practice, it is difficult to use standard sources for all samples geometries. Accordingly, for this purpose, the efficiency transfer method can be used. Starting from the experimental efficiency for a reference point source, the efficiency for the sample can be evaluated using a mathematical model or simulation software.

Formally, the efficiency transfer method is based on the next equation [5]:

$$\varepsilon_{(calc)} = T\left(\frac{calc}{ref}\right)\varepsilon_{(ref)} \tag{2}$$

where $T\left(\frac{calc}{ref}\right)$ is the transfer factor.

The transfer factors can be calculated with the Monte Carlo [6] method or with more simplified procedures [14, 15] using the relationship between the simulated efficiency for measurement geometry and the efficiency for the reference geometry. The benefit of this method is that the results are less affected by the uncertainties of detector parameters, which represent a more important uncertainty source in the direct simulation of the efficiencies. Undoubtedly, an improper value will be considered for the detector radius, and this will strongly affect the values of the efficiencies calculated by simulation or evaluation by analytical computation, while the transfer factor is slightly sensitive to this incorrect value, because a wrong value will simultaneously affect both the efficiency calculated for the reference geometry and that for the geometry of interest and their ratio will be practically unchanged. The sensitivity of the efficiency to details of the input data and to the computation model was clearly revealed by Vidmar in 2008 [16]. Clearly, the efficiency transfer method offers better results in the case when the measurements of interest are similar to the reference measurements.

The National Laboratory Henri Becquerel (LNHB) from Saclay, France, developed in the early 2000s a software named ETNA (Efficiency Transfer for Nuclide Activity), dedicated for the calculation of the detector efficiency under measurement conditions different from those of calibration, and for the correction of the coincidence summing effects. The application of the ETNA software makes possible to greatly increase the accuracy of the results of quantitative analysis by gamma-ray spectrometry and avoid time-consuming measurement sequences [15].

The ETNA software was applied for the evaluation of the efficiencies for various geometries based on the efficiencies values for the reference measurement geometry.

2.3.1. Computation of the efficiency for disk sources for the NaI(Tl) detector

ETNA software was used in this section to achieve the efficiency transfer from a point source geometry to disk sources geometries for the NaI(Tl) detector. Due to lack of calibration certificates for standard disk sources, the efficiency calibration was calculated based on point sources measured with the NaI(Tl) detector.

Assuming symmetry of the cylindrical detector, for the determination of the experimental efficiencies in view of surface contamination measurement, the next relations were used:

$$N = \int_{(S)} \varepsilon(r)\Lambda_S(r,\varphi)dS \tag{3}$$

$$\approx N = \int_0^R \int_0^{2\pi} \varepsilon(r)\Lambda_S(r,\varphi)rdrd\varphi \tag{4}$$

$$\approx N = \int_0^R \varepsilon(r)rdr\int_0^{2\pi} \Lambda_S(r,\varphi)d\varphi \tag{5}$$

$$\approx N = 2\pi\int_0^R \varepsilon(r)\overline{\Lambda_S(r)}rdr \tag{6}$$

where N is the peak count rate; $\varepsilon(r)$ is the efficiency of a point source situated at distance r from the symmetry axis of the detector; $\Lambda_S(r, \phi)$ is the surface activity of the source in the point of (r, ϕ) coordinates; $\overline{\Lambda_S(r)} = \frac{1}{2\pi}\int_0^{2\pi} \Lambda_S(r, \phi)d\phi$.

Considering that the surface activity is uniformly distributed, result that:

$$N = 2\pi\Lambda_S\int_0^R \varepsilon(r)rdr \tag{7}$$

$$N = \Lambda_S I(R) = \pi R^2 \varepsilon \Lambda_S \tag{8}$$

$$\text{or } \varepsilon = \frac{1}{\pi R^2} I(R) \tag{9}$$

$$\text{were: } \quad I(R) = 2\pi\int_0^R \varepsilon(r)rdr \tag{10}$$

Then, the following result is obtained:

$$\varepsilon = \frac{2}{R^2}\int_0^R \varepsilon(r)\,rdr \tag{11}$$

Using Eq. (11), the detection efficiency for the disk sources with radius of r = 1, 2, 3 and 4 cm for the NaI(Tl) detector was calculated. The values of the efficiencies $\varepsilon(r)$ were taken from the measured efficiency curves, corrected for coincidence summing effects.

Using the ETNA software, the detection efficiencies for disk sources were calculated for the same type of detector and the same measuring geometry. The reference measurement is represented by a point source located at r = 0 cm (on the symmetry axis of the detector); thus, the reference efficiency is ε_0. In **Figure 6**, the efficiency calibration curves, evaluated with the ETNA software, are represented for the disk sources with radius of r = 1, 2, 3 and 4 cm; and a comparison between the results obtained applying Eq. (11) and those evaluated using ETNA software for efficiencies detection for a disk source with r = 4 cm.

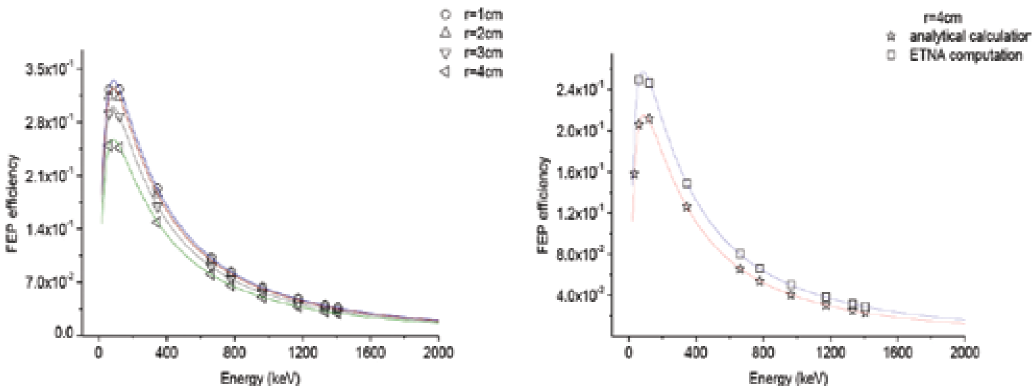

Figure 6. The efficiency calibration curves and ETNA vs. analytical calculation for the NaI(Tl) detector.

The values obtained with the analytical procedure are in accordance with the values resulted using ETNA software. The differences can arrive from the method used or from the input data. Should be mentioned that ETNA software calculates efficiencies for geometries in with the center of the source is placed only on the detector axis; different radial distances than that cannot be included.

2.3.2. The ETNA computation for the HPGe detector

The transfer of the efficiency from the reference point source geometry, $\boldsymbol{h}$ = 10 cm, to other point source geometries (distances from the detector end cap equal to 2, 5, 15 and 20 cm) and the computation of the efficiency for cylindrical samples with different matrices was done using ETNA software for the HPGe detector.

Using the fitted efficiency data for the reference measurement as input, the description of the reference source, the description of the source for which the efficiencies are required, the source-detector distance, the detector-absorber distance, ETNA software was applied for the computation of the efficiency for the other measurement geometries for the HPGe detector. The experimental efficiency curves were compared with the prediction of the ETNA software. Excepting the case of the smallest distance from the source to the detector, the discrepancies between ETNA and the experimental results were generally below 3%. In the case of the measurement at 2 cm distance from the detector, the discrepancies were higher being sensitive to the detector geometrical data. This is because the detector specifications established by the manufacturer of the detector were used without any optimization. Furthermore, the uncertainty of the distance between the crystal and the end cap (the manufacturer value) has a contribution in the uncertainty of the transfer factor, because of the change in the solid angle [10].

The HPGe detector efficiency transfer method has also been used for the efficiencies evaluation for the specific cylindrical sources. For this purpose, the matrix was considered water equivalent for the matrix with ρ = 1.0 g/cm^3 and soil composition for the matrix with ρ = 1.4 g/cm^3.

The default attenuation coefficients foreseen by ETNA code were used for the matrices involved in the study.

In the case of the soil matrix, containing ^{137}Cs, the ratio between the ETNA software values and the experimental values of the efficiency was 1.038 for $\boldsymbol{h}$ = 0 cm and 0.966 for $\boldsymbol{h}$ = 2 cm. The higher discrepancies in the case of ^{134}Cs results (gel matrix) in comparison with the results for ^{137}Cs (soil matrix) can be attributed to the uncertainty of coincidence summing effects and of the matrix effects.

3. Simulation of gamma-ray spectra using Geant 3.21 Monte Carlo code for sources distributed in 220l volume

Application area of the radiation transport modeling through Monte Carlo method is extremely large, from the nuclear reactor design to parameters calculation of complex detection systems, from the simulation and the interpretation of various experiments to the calculation of the dose coefficients. Nowadays, this area is expanding, both by tackling new problems in modeling and by the inclusion of some details, previously neglected, of the respective phenomena [17]. What characterizes the Monte Carlo method is the remarkable fidelity with which it can describe physical phenomena, without approximations [18, 19]. Theoretically, the accuracy of results is limited only by the accuracy of the nuclear data (the effective cross section of interaction) used, and no other method is competitive with the Monte Carlo method in this regard. Accordingly, the Monte Carlo method is often used as a reference method; the simplified calculation procedures, faster, based on some approximations are tested in relation to this method, and even nuclear data can be validated by interpretation of the Monte Carlo complex experiments [18, 19].

In the Monte Carlo method, a problem of radiation transport is solved by simulating the evolution of a large number of radiations and the analysis of their fate. The evolution (the history) of each radiation starts with its emission continues with the undisturbed propagation through the environment between the successive interactions and by changing its parameters (possibly even its disappearance) in the points where the interactions takes place. In the case of photon transport at keV–MeV energy range, complex effects are important, such as Compton photoelectric and electron–positron pairs generation effects. Following the Compton effect, the incident photon energy is transferred to the recoil electron and to the scattered photon. In the photoelectric effect, the photon is absorbed, an electron is emitted, and the atom remains in an excited state. In the pair production effect, the photon energy is consumed to produce a pair of electron–positron particles. Thus, except for the Compton effect, the history of each photon ends at the interaction point. However, in terms of energy dissipation in substance, the primary interaction of the photon is only the starting point. The resulted electrons give their energy causing ionization and excitation, emitting new photons (secondary radiation), and the atoms will relax from excited states, emitting new photons and possibly Auger electrons; the positron will annihilate producing annihilation photons that interact further. Obviously, if more details of the secondary radiation will be included, the computing time will increase, and the computation program becomes more complex with more branched. At every interaction, the evolution of the resulting products and then of the successive generations of secondary radiations should be evaluated. Which details are relevant and which are not depends on the problem to be solved for achieving an optimal compromise between modeling finesse, the required accuracy and the programming effort and the necessary computing time. For incident photons with energy up to a few MeV, characteristic X-rays, the bremsstrahlung radiation (emitted by electrons resulting from interactions) have energies much lower than the primary photon energy. Consequently, in many problems, X-rays can be considered locally absorbed.

The development of the Monte Carlo methods and the improvement of computational technologies have led to the development of several Monte Carlo simulation programs for simulating radiation transport. Simulation codes used are GEANT 3 [20], GEANT 4 [21], MCNP [22], GESPECOR [6], FLUKA [23], ETRAN [24], EGS [25–27], PENELOPE [28], etc.

In this section, the application of Monte Carlo simulation to the study and examination of the response function characterization of two gamma-ray spectrometry systems used for measuring large sources was reported. For this purpose, GEANT 3.21 code was applied for the spectra simulation expected to be obtained for 50–2000 keV energy range for volume sources measured with both systems. Although the prevalent application of Monte Carlo simulation for efficiency calibration of HPGe detectors for the measurements of small volume samples up to several dm^3, extensive realistic computations by Monte Carlo methods have not been carried out until now for the measurement of big volume samples like 220l waste drums.

3.1. Experimental configuration

The first system used is an ISOCART from Ortec (Geom1) and has a p-type detector with a relative efficiency of 25%. The second system used is a WS1100 Segmented Gamma Scanner from Canberra (Geom2) and has a p-type detector with a relative efficiency of 44.4%. The characteristics and dimensions of the detectors are presented in **Figure 7**.

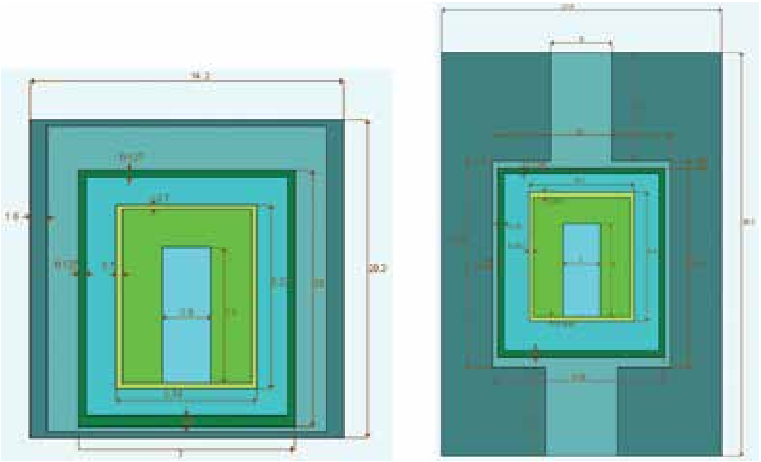

Figure 7. ISOCART (left) and Segmented Gamma Scanner WS1100 (right) gamma-ray spectrometry systems.

The volume source considered in simulation was a 2201 radioactive waste drum typically used for conditioning of radioactive waste in Romania. Several studies were reported using this kind of sample [29–32]. The source matrix was considered to be concrete with standard composition, and the axis of the detector was perpendicular on the axis of the cylinder. The distance from the center of the coordinate system associated to the detector to the center of the cylinder was 50 cm for both geometries.

3.2. Monte Carlo simulations

GEANT 3.21 [20] is a method of detector description and simulation tools, whit characteristics presented in **Figure 8**.

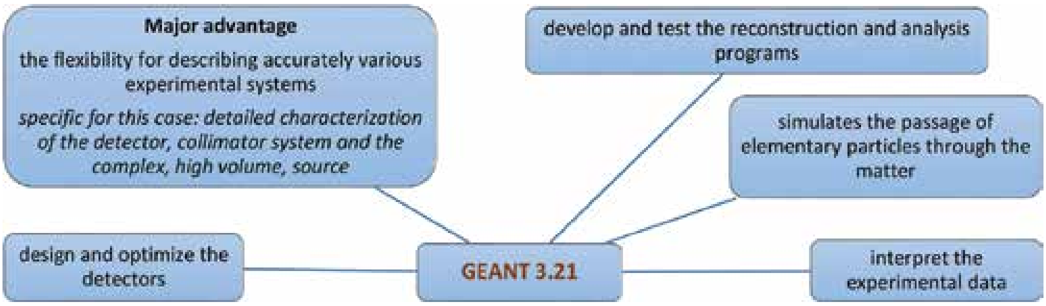

Figure 8. GEANT 3.21 characteristics.

In essence, the utilization of the Monte Carlo simulation method for the detection efficiencies evaluation for large samples such as waste drum is nearly the same as in the situation of small samples. Considering the practical aspects, it appears a large difference regarding the calculation time. In the case of big samples, in which the majority of emission points are located far away from the detector, the fraction from the number of emitted photons that contributes to the detector signal is very small. Consequently, the number of photons that should be followed until a statistically significant number of signals will be reached should be very large, resulting in a long computation time.

In the experiment presented in this section, 4.32E+10 photons were simulated. All the details of the source, measurement geometry and detector were implemented in the GEANT 3.21 code. To explain the simulation process, **Figure 9** was created.

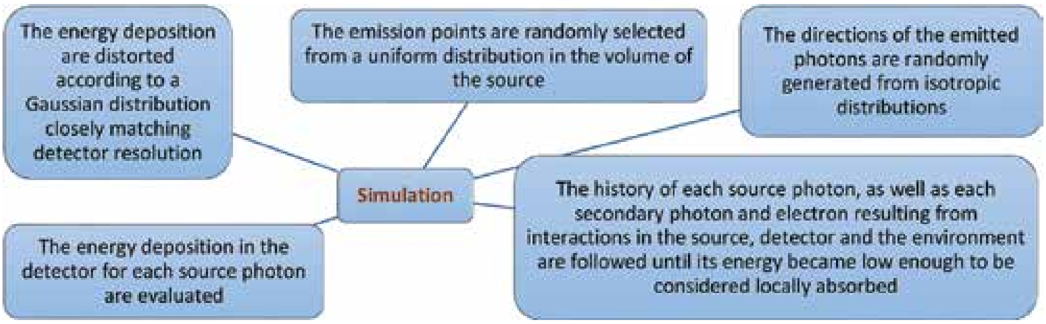

Figure 9. Simulation process.

The simulations were done for the main gamma-ray photons (12 energies) emitted by ^{152}Eu. In the case of Geom1, 1.5E+09 photons were followed for each energy, totalizing 1.8E+10 photons for all energies. In the case of Geom2, 2.1E+09 photons were simulated for each energy, representing 2.52E+10 photons in total for all energies. Individual spectra were recorded in separate files, and in the end, all spectra were combined with weights according to the emission probability of each gamma-ray [33]. The resulting spectra are presented in **Figure 10**.

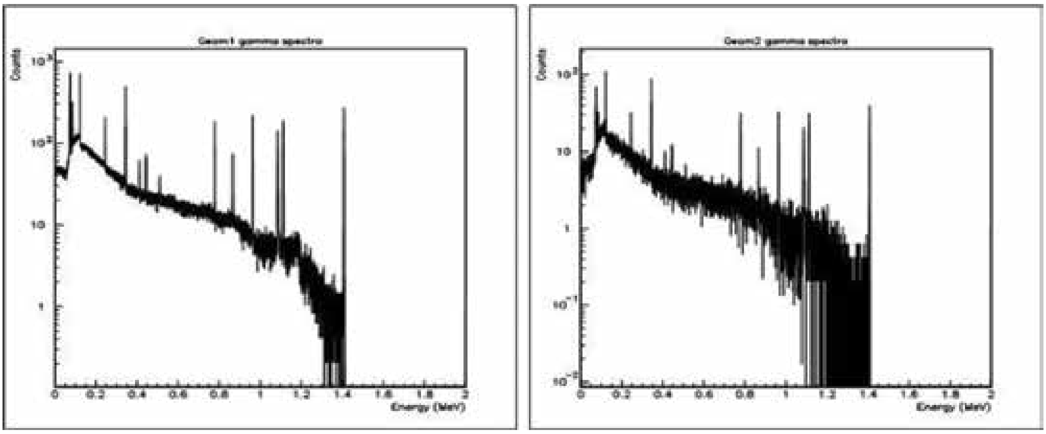

Figure 10. The final spectrum for Geom1 and Geom2 geometries.

3.3. The detection efficiency evaluation

The detector intrinsic efficiency commonly is conditioned mainly by the material of the detector, the radiation energy and the physical thickness of the detector in the direction of the incident radiation [34]. A small dependence on source-detector distance is present due to the average path length of the radiation through the detector will amend somewhat with this area. The counting efficiencies can be classified by the nature of the events recorded. If all phenomena from the detector will be recorded, then the total efficiency will be of interest. Therefore, all interactions, no matter if the energies are small, are considered to be recorded. The peak efficiency presumes that only those interactions that deposit the full energy of the incident radiation are recorded. If the total area under the peak is integrated, then the number of full energy events can be achieved. In **Figure 11**, it represents the FEP and total peak efficiencies obtained from the simulated spectra, for Geom1 and Geom2 geometries. The fact that the efficiency in Geom2 is smaller than in Geom1 even if the second detector has a higher intrinsic efficiency is due to the smaller collimator acceptance in the case of Geom2.

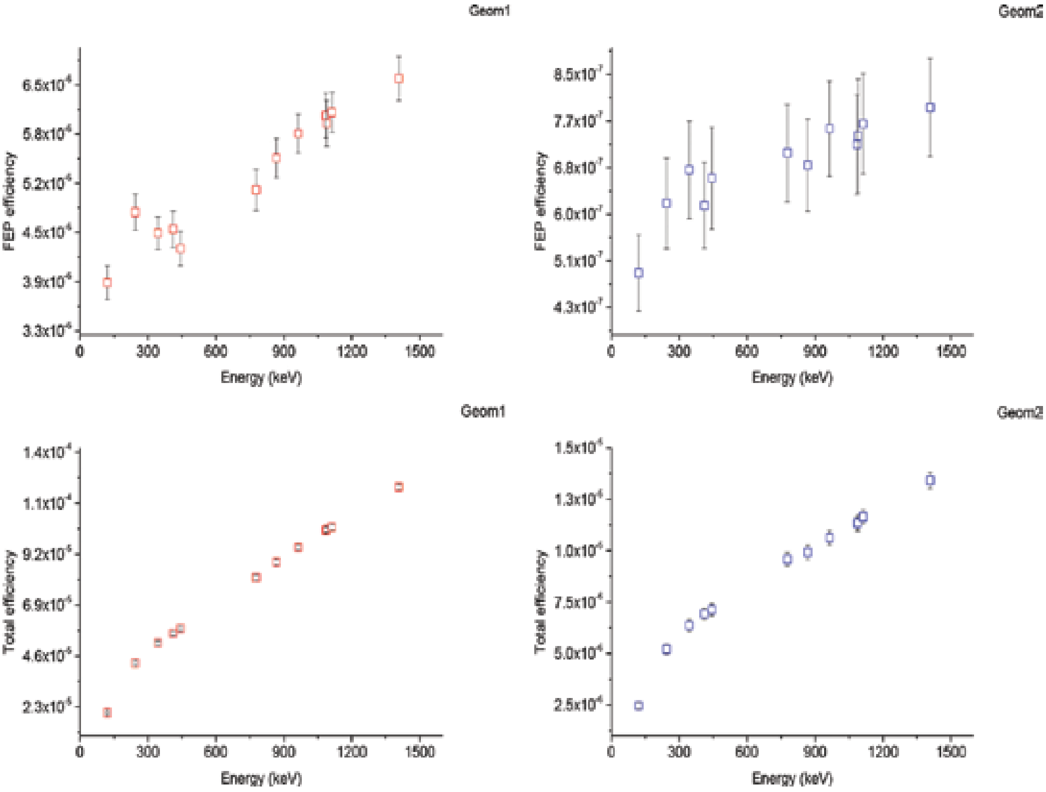

Figure 11. The peak efficiencies and total efficiencies simulated with GEANT 3.21 for Geom1 and Geom2.

4. Summary and conclusions

This chapter explores the specific gamma-ray spectrometry phenomena in their deepness in different work conditions. Thus, the studies, simulations and experimental results were carried out and were presented in an integrated view in the sections of the chapter.

The utility of numerical method as it is ETNA software to compute the efficiency transfer factors for divers measurement geometries used in routine laboratory measurements was tested for NaI(Tl) and HPGe detector. Starting from a reference efficiency measured for a point source, peak efficiencies were evaluated for point sources placed at several detector-source distances, moreover for disc sources or for volume sources with different compositions and densities. This was done specifically for each detector involved in the study. The methodology shows that the efficiency transfer factors are accurately computed using ETNA software. The obtained results are valuable and can be used without restriction if all the details of the detectors and measurements are accurately known.

An important contribution in the development of gamma-ray spectrometry methods was made with the examination realized for the response function characterization of the two gamma-ray spectrometry systems: ISOCART from Ortec and WS1100 Segmented Gamma Scanner from Canberra. These systems are used especially for the measurement and characterization of radioactive waste. Based on GEANT 3.21 toolkit, a simulation program was developed to simulate the spectra expected to be obtained by the two systems, for volume sources, and for the 50–2000 keV energy range. Many spectra (hundreds) were simulated and then combined to obtain the spectrum expected in real measurements.

Considering the national regulations, the radioactivity and the nuclide composition of the waste must be identified prior to their transfer outside the site of their burial or placement in storage areas. The most important step on the characterization process is the establishment of the radionuclide content, most often achieved through non-destructive measurements (NDA). The radiological characterization of radioactive waste should ensure their correct classification and a reasonable use of interim storage and final disposal. The radioactivity overestimation leads to a reduction in waste storage capacity, and the underestimation creates problems in terms of safety. The release from regulatory control will reduce the volume of storage waste and enable their beneficial use.

Future studies are required to develop calibration techniques and evaluation of measurement for parallelepiped shape containers with radioactive waste using gamma spectrometric measurement systems. The counting geometry of parallelepiped container is completely different from the counting geometry of a small cylindrical radioactive source, and consequently, the efficiency calibration is more difficult to be estimated. Knowing the efficiency calibration, which varies greatly with the source-detector distance, the geometry and the absorption factors, is essential for the assay of radioactive waste. Because it is almost impossible to estimate the efficiency calibration curve based on the experimental measurement, simulation programs based on the Monte Carlo codes need to be developed. The evaluation of response function of HPGe detectors for parallelepiped counting geometry needs to be done.

Acknowledgements

I want to express my appreciation to Prof. Univ. Dr. Octavian Sima from University of Bucharest and Dr. Doru Stanga, Head of the Radiological Characterization Laboratory from Horia Hulubei National Institute for R&D in Physics and Nuclear Engineering for their constant support which they have given to me over the years. Each of them represents a rigorous scientific model for me which I hope will be reflected in my work. Also, I want to show my gratitude to Dr. Radu Deju, Head of the Reactor Decommissioning Department and Dr. Mitica Dragusin, Nuclear Safety Director from Horia Hulubei National Institute for R&D in Physics and Nuclear Engineering for their confidence and work appreciation.

Author details

Daniela Gurau

Address all correspondence to: daniela.gurau@ymail.com

Horia Hulubei National Institute for R&D in Physics and Nuclear Engineering, Magurele-Bucharest, Romania

References

[1] IAEA. Methodology and technology of decommissioning. 1986; TRS No. 267.

[2] Sima O, Lepy MC. Application of GUM Supplement 1 to uncertainty of Monte Carlo computed efficiency in gamma-ray spectrometry. Appl. Radiation. Isot. 2016; 109:493–499.

[3] Debertin K, Helmer RG. Gamma and X-ray spectrometry with semiconductor detectors. North-Holland, Amsterdam. 1988.

[4] Sima O, Arnold D. Accurate computation of coincidence summing corrections in low level gamma-ray spectrometry. Appl. Rad. Isot. 2000; 53:51–56.

[5] Sima O, Arnold D. Transfer of the efficiency calibration of germanium gamma-ray detectors using the GESPECOR software. Appl. Rad. Isot. 2002; 56:71–75.

[6] Sima O, Arnold D, Dovlete C. GESPECOR-A versatile tool in gamma-ray spectrometry. J. Radioanal. Nucl. Chem. 2001; 248:359–364.

[7] Bruggeman M, Verheyen L, Vidmar T, Liu B. Assessing sample attenuation parameters for use in low-energy efficiency transfer in gamma-ray spectrometry. Appl. Radiation. Isot. 2016; 109:547–550.

[8] Moens L, De Donder J, Lin Xi-lei, De Corte F, De Wispelaere A, Simonits A, Hoste J. Calculation of the absolute peak efficiency of gamma-ray detectors for different counting geometries. Nucl. Instr. Meth. Phys. Res. 1981; 187:451–472.

[9] Lépy MC, Altzitzoglou T, Arnold D, Bronson F, Capote Noye R, Décombaz M, De Corte F, Edelmaier R, Herrera Peraza E, Klemola S, Korun M, Kralik M, Neder H, Plagnard J, Pommé S, de Sanoit J, Sima O, Ugletveit F, Van Velzen L, Vidmar T. Intercomparison of efficiency transfer software for gamma-ray spectrometry. Appl. Radiat. Isot. 2001; 55:493–503.

[10] Radu D, Stanga D, Sima O. ETNA software used for efficiency transfer from a point source to other geometries. Appl. Radiat. Isot. 2009; 67:1686–1690.

[11] Radu D, Stanga D, Sima O. Transfer of detector efficiency calibration from a point source to other geometries using ETNA software. Rom. Rep. Phys. 2010; 62:57–64.

[12] ISO. Guide to expression of uncertainty in measurements. Geneva, Switzerland. 1993 (corrected and reprinted 1995).

[13] Sima O, Dovlete C. Matrix effects in the activity measurement of environmental samples—implementation of specific corrections in a gamma-ray spectrometry analysis program. Appl. Radiat. Isot. 1997; 48:59–69.

[14] Piton F, Lépy MC, Bé MM, Plagnard J. Efficiency transfer and coincidence summing corrections for gamma-ray spectrometry. Appl. Radiat. Isot. 2000; 52:791–795.

[15] Lépy MC, Bé MM, Piton F. ETNA (Efficiency Transfer for Nuclide activity measurement): software for efficiency transfer and coincidence summing corrections in gamma-ray spectrometry. Note Technique LNHB 01/09/A. 2004.

[16] Vidmar T, Aubineau-Laniece I, Anagnostakis MJ, Arnold D, Brettner-Messler R, Budjas D, Capogni M, Dias MS, De Geer LE, Fazio A, Gasparro J, Hult M, Hurtado S, Jurado Vargas M, Laubenstein M, Lee KB, Lee YN, Lepy MC, Maringer FJ, Medina Peyres V, Mille M, Moralles M, Nour S, Plenteda R, Rubio Montero MP, Sima O, Tomei C, Vidmar G. An intercomparison of Monte Carlo codes used in gamma-ray spectrometry. Appl. Radiat. Isot. 2008; 66:764–769.

[17] Choi Y, Lee KB, Kim KJ, Han J, Yi ES. Development of an optimized Compton suppression gamma-ray spectrometry system using Monte Carlo simulation. Appl. Radiat. Isot. (Forthcoming). doi:10.1016/j.aprasido.2015.12.058.

[18] Jacoboni C, Lugli P, editors. The Monte Carlo method for semiconductor device simulation. Computational Microelectronics ed. Springer-Verlag Wien New York. 1989. ISSN: 0179-0307.

[19] Geant group, editor. Physics Reference Manual, Version: Geant4 10.2 (4 December 2015). 2015. http://geant4.web.cern.ch/geant4.

[20] Brun R, Bruyant F, Maire M, McPherson AC, Zanarini P. GEANT3. Geneva: CERN Data Handling Division. 1987; DDD/EE/84-1.

[21] Agostinelli S, Allison J, Amako K, Apostolakis J, Araujo H, Arce P, Asai M, Axen D, Banerjee S, Barrand G, Behner FL, Bellagamba J, Boudreau L Broglia Brunengo A, Burkhardt H, Chauvie S, Chuma J, Chytracek R, Cooperman G, Cosmo G, Degtyarenko P, Dell'Acqua A, Depaola G, Dietrich D, Enami R, Feliciello A, Ferguson C, Fesefeldt H, Folger G, Foppiano F, Forti A, Garelli S, Giani S, Giannitrapani R, Gibin D, Gómez Cadenas JJ, Gonzálezq G, Gracia Abril G, Greeniaus G, Greiner W, Grichine V, Grossheim A, Guatelli S, Gumplinger P, Hamatsu R, Hashimoto K, Hasui H, Heikkinen A, Howard A, Ivanchenko V, Johnson A, Jones FW, Kallenbach J, Kanaya N, Kawabata M, Kawabata Y, Kawaguti M, Kelner S, Kent P, Kimura A, Kodama T, Kokoulin R, Kossov M, Kurashige H, Lamanna E, Lampén T, Lara V, Lefebure V, Lei F, Liendl M, Lockman W, Longo F, Magni S, Maire M, Medernach E, Minamimoto K, Mora de Freitas P, Morita Y, Murakami K, Nagamatu M, Nartallo R, Nieminen P, Nishimura T, Ohtsubo K, Okamura M, O'Neale S, Oohata Y, Paech K, Perl J, Pfeiffer A, Pia MG, Ranjard F, Rybin A, Sadilov S, Di Salvo E, Santin G, Sasaki T, Savvas N, Sawada Y, Scherer S, Sei S, Sirotenko V, Smith D, Starkov N, Stoecker H, Sulkimo J, Takahata M, Tanaka S, Tcherniaev E, Safai Tehrani E, Tropeano M, Truscott P, Uno H, Urban L, Urban P, Verderi M, Walkden A, Wander W, Weber H, Wellisch JP, Wenaus T, Williams DC, Wright D, Yamada T, Yoshida H, Zschiesche D. GEANT4-a simulation toolkit. Nucl. Instr. Meth. Phys. Res. A. 2003; 506:250–303.

[22] Briestmeister JF. MCNP—A general Monte Carlo N-particle transport code. Los Alamos National Laboratory, Report LA-13709-M. 2000.

[23] Fassò A, Ferrari A, Roesler S, Sala PR, Ballarini F, Ottolenghi A, Battistoni G, Cerutti F, Gadioli E, Garzelli MV, Empl A, Ranft J. The physics models of FLUKA: status and recent development. eConf C0303241, MOMT005. 2003.

[24] Berger MJ, Seltzer SM. EFTRAN-Monte Carlo code system for electron and photon transport through extended media. RISC computer code package CCC-107. Oak Ridge National Laboratory, Oak Ridge, TN. 1973.

[25] Nelson WR, Hirayama H, Rogers DWO. The EGS4 Code System, Report SLAC-265. Stanford Linear Accelerator Center, Stanford, CA. 1985.

[26] Hirayama H, Namito Y, Bielajew AF, Wilderman SJ, Nelson WR. The EGS5 code system, Report SLAC-R-730. Stanford Linear Accelerator Center, Stanford, CA. 2006.

[27] Kawrakow I, Rogers DWO. The EGSnrc Code System: Monte Carlo Simulation of Electron and Photon Transport. NRCC Report PIRS-701. 2006.

[28] Baro J, Sempau J, Fernandez-Varea JM, Salvat F. PENELOPE, an algorithm for Monte Carlo simulation of the penetration and energy loss of electrons and positrons in matter. Nucl. Instr. Meth. Phys. Res. B. 1995; 100:31–46.

[29] Dinescu L, Vata I, Cazan IL, Macrin R, Caragheorgheopol G, Rotarescu G. On the efficiency calibration of a drum waste assay system. Nucl. Instr. Meth. Phys. Res. A. 2002; 487:661–666.

[30] Haralambie M, Dinescu L, Sima O. New data concerning the efficiency calibration of a drum waste assay system. Part I: Experimental calibration. Rom. Rep. Phys. 2004; 56:711–720.

[31] Toma M, Sima O, Olteanu C. Experimental and simulated studies for the calibration of a radioactive waste assay system. Nucl. Instr. Meth. Phys. Res. A. 2007; 580:391–395.

[32] Sima O, Cazan IL, Dinescu L, Arnold D. Efficiency calibration of high volume samples using the GESPECOR software. Appl. Radiation. Isot. 2004; 61(2–3):123–127.

[33] NUCLÉDE-LARA (web applet). Gamma and alpha spectrometry on-line library [Internet]. 2008. Available from: http://laraweb.free.fr/.

[34] Knoll GF. Radiation Detection and Measurement. 4th Edition. John Wiley & Sons. 2010.

Section 3

Fusion Technology

Chapter 7

Tungsten-Based Composites for Nuclear Fusion Applications

Owais A. Waseem and Ho Jin Ryu

Additional information is available at the end of the chapter

http://dx.doi.org/10.5772/62434

Abstract

This chapter provides a comprehensive knowledge about the potential role of tungsten-based composites in fusion reactors and the research work which has been done in this very important area of nuclear materials. The characteristics of tungsten, which make it the most potential candidate for plasma-facing applications, have been presented along with the shortcomings in pure tungsten. The research work that has been done so far in the field of tungsten-based composites to overcome the problems with pure tungsten has been included. The fabrication, characterization, types of reinforcements and the classes of composites have been reviewed. The behavior of tungsten-based composites under various kinds of loads (i.e. mechanical and thermal) and environments (radiations and oxidizing etc.) has been summarized.

Keywords: tungsten-based composites, nuclear fusion, plasma-facing materials, metal matrix composites, oxide dispersion

1. Introduction

Engineering materials for nuclear applications must be able to withstand extremely harsh service conditions. Among the various areas of nuclear engineering, the fusion reactor system presents a great challenge for materials engineering. The fusion environment, i.e., with high temperatures and high neutron and particle flux, steps up the degradation and alters the mechanical and thermal behavior of the fusion reactor materials, jeopardizing the dimensional stability and integrity of the materials [1]. The selection of proper materials for certain applications has always been somewhat difficult, and the fusion environment, involving high temperatures and likely radiation damage, makes this task more difficult [1].

As a result of extensive research, tungsten (W) has emerged as a highly useful plasma-facing material (PFM) [1–3]. Its high melting point, high thermal conductivity, low coefficient of thermal expansion, high sputtering threshold energy, low tritium retention and low neutron activation make W a potential candidate for fusion applications [4–6]. Previously, applications of W were rare and were limited to experimental purposes only in tokamaks due to the formation of high-Z dust, which originates from materials eroding on the surfaces of the plasma-facing components. This dust has detrimental effects on the plasma parameters [7], but research has revealed the feasibility of plasma operations with W [1, 8]. The plasma impurity problem associated with W may be eliminated by ensuring that the energy of the plasma particles remains lower than the sputtering threshold (~700 eV for tritium) [9]. In fusion applications, an increase in the future utilization of W is foreseen [9, 10], as it is considered as a first wall [11] and a divertor surface [1] material for future fusion reactors, as illustrated in **Figure 1**.

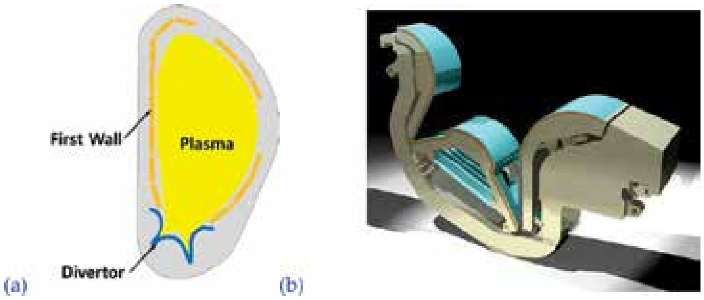

Figure 1. (a) A schematic cross-section of tokamak and (b) a solid model illustration of divertor (commons.wikimedia.com).

As compared to other high-temperature applications, which require good physical and mechanical properties such as high thermal conductivity, good thermal shock resistance and high-temperature strength, toughness and stiffness [12], fusion reactors impose very complex requirements on plasma-facing materials (PFMs) [1]. While PFMs are assumed to be able to sustain high mechanical, thermal and magnetic loads for prolonged periods of time [8], irradiation effects are particularly important in plasma-facing components [13]. Transmutation and ballistic damage, which alter the composition and microstructure of materials due to the interaction between the materials and the high-energy neutron flux (~14 MeV), reduce the mechanical properties of PFMs. The interaction of neutron flux with materials forms dislocation loops and clusters of transmutation products from non-equilibrium phases [14].

The energetic ions and neutral atoms in the service environments of fusion reactors cause sputtering erosion in plasma-facing components [1], which is a major concern associated with these materials [8]. The free atoms can be ionized and form contaminants. These contaminants can then be deposited at various locations on the chamber wall. The erosion and re-deposition create new layers which can shorten the service lifetime of the fusion reactor by enhancing tritium retention and morphology variations [8].

Appropriate mechanical, thermal and physical properties are commonly required in plasma-facing components [15]. The hydrogen isotope retention of the materials is also one of the essential considerations when selecting appropriate materials [9]. In the future, the challenges associated with PFMs are expected to increase due to the continuous increase in the thermal loads of upcoming fusion reactors. For example, PFMs may experience very high amounts of localized energy in a very short period of time during transient conditions. Plasma disruption, vertical displacement events (VDEs) and the edge-localized mode (ELM) cause these high localized thermal loads [16], and the inner and outer plates of the divertor may experience loads of ~7–40 MJ/m^2 and ~4–25 MJ/m^2 due to plasma disruption. Considering VDEs, the energy deposition on the outer wall blanket modules may increase to ~20–30 MJ/m^2 in ~0.1/0.3 μs. The ELM, if it is controlled, may impose loads of 0.5 MJ/m^2 and 0.3 MJ/m^2 on the inner and outer plates, respectively, of the divertor, whereas the ELM if uncontrolled may be more severe as it can impart corresponding loads of 10 MJ/m^2 and 6 MJ/m^2 on the inner and outer plates of the divertor within ~0.25 to 0.5 μs [17].

2. Properties of W for fusion applications

2.1. Advantages of W and drawbacks of using pure W in fusion applications

In order to be considered as a potential candidate for plasma-facing and high-temperature applications, more specifically for the divertor and the first wall in a fusion power reactor, a material must fulfill all of the requirements of plasma-facing applications noted in the above section. W has unique characteristics, which have increased its value relative to other materials. The properties which confer this valuable status in nuclear engineering include its refractoriness, high melting point, high thermal conductivity, low thermal expansion coefficient, good chemical stability, high heat resistance, high sputtering threshold energy, low sputtering rate, low erosion rate at edge plasma temperatures of less than 40–50 eV, low deuterium/tritium retention rate, low tritium permeability, high moduli of elasticity, good thermal shock resistance, lack of hydride formation and adequate corrosion resistance [12, 15, 18–30]. The use of W is associated with other advantages as well. For instance, under neutron irradiation, the thermal conductivity of W does not decrease sharply [12]. Moreover, it is not greatly affected by high activation [19]. Taken together, these properties increased the usefulness of W in plasma-facing and high-temperature applications.

However, W has a number of shortcomings as well, which need to be addressed. The behavior of W is undoubtedly advantageous for fusion applications, but the few drawbacks of W create areas for further research to make W more reliable. Inherently, W possesses a high ductile-to-brittle transition temperature (DBTT), low ductility and poor fracture toughness, low machinability and fabricability, low-temperature brittleness, radiation-induced brittleness, and a relatively low recrystallization temperature compared to its operation temperature [5, 15, 21, 26, 29]. The use of W above its recrystallization temperature interminably can be unsafe because its mechanical properties decrease in such an environment [19, 21]. W is also associated with high embrittlement due to irradiation at low temperatures [4, 22, 24], and the DBTT of W increases with an increase in the radiation level [29]. Low-temperature brittleness imposes restrictions on the application of tungsten as a structural material [25, 27, 28].

The development of a melt layer due to an intense thermal transient condition stimulates the generation of highly activated dust particles. Due to the interaction with high-energy ions, W can undergo additional erosion [1]. W shares a common disadvantage with other high-Z materials, i.e., very low acceptable impurity concentrations in the plasma, thus requiring almost perfectly controlled plasma [1]. The recombination rate coefficient for H_2 is very high in W, and the high hydrogen content results in bubbles and blisters. Keeping W at an elevated temperature will increase the blisters and the inventory problem [9]. He bubbles are also observed when W samples are exposed to He plasma [31–33].

Due to its high hardness, high brittleness, and poor machinability, the manufacturing of W parts is very costly and time-consuming [20]. The joining of W to a Cu-based (CuCrZr) heat sink is troublesome, owing to the large difference in the CTEs of these two materials [18]. Considering all of these shortcomings, it can be said that further enhancements of the properties of W are essential prior to its commercial use [4, 18].

2.2. Recent trends to enhance the performance of W

Pure W shows favorable behavior for applications to high-temperature and plasma-facing applications. Regarding the aforementioned limitations, research is in progress to improve W and make it useful in future fusion reactors [4]. Currently, research in the field of plasma-facing materials focuses on determination of the impacts of ion irradiation on the properties of W [4]; improvements of its mechanical properties [1], such as its ductility [19] and fracture toughness [15]; methods to mitigate its brittleness [26]; and clarifications of the activation of this material [2].

Various options are being utilized for modifications and improvements of these properties. Some of these techniques involve (i) W-based composites [19], (ii) nanocrystalline W-based materials [1, 5, 34], (iii) W–X (X=Ta, Re, Mo, V, Ti, etc.) alloys created by powder metallurgy [15, 35–39], (iv) the dispersion of ductile fibers in W by mechanical synthesis [25], (v) the dispersion of ceramic particles of transition metals [13], (vi) the addition of rare-earth oxide particles into W [26], (vii) effective energy dissipation caused by controlled cracking and friction at fiber/matrix interfaces [28], and the utilization of functionally graded materials (FGMs) as an efficient solution to the joining problem of W to copper-based heat sinks [34], (viii) the creation of laminated hybrid composites [18], (ix) the post-processing of W to obtain full densification [21], and (x) the addition of a sintering activator to obtain high density levels [21].

All of the abovementioned methods and techniques have some influence on the properties of W. For instance, equal-channel angular pressing (ECAP) reduces the brittleness and improves the toughness and strength of ultrafine (0.9 μm) equiaxed grains of W [21], as ECAP ultra-fine-grained W exhibits much smaller cracks as compared to coarse-grained W around dents produced by microhardness tests even at 250°C [30]. Plasma spraying offers high adhesion and stability of thick W coatings on EUROFER steel [1]. Among all of these options, W-based composites are of great importance due to their diverse range of useful properties.

3. Development of W-based composites for nuclear applications

Conventional alloys of W exhibit brittle behavior [40]; therefore, the development of W-based composite materials is considered to be advantageous for incorporating W with desirable properties [40]. A number of additives [36, 41–47] have been examined for the production of W composites with enhanced high-temperature mechanical properties [48–50] and good irradiation resistance [51–53].

3.1. Types of W-based composites

The research focusing on incorporating W with enhanced high-temperature properties and irradiation resistance via composite materials is multidimensional. Various types of W-based composites, including dispersion-strengthened, particle-reinforced, fiber-reinforced, and laminated composites, as illustrated in **Figure 2**, are being developed and investigated.

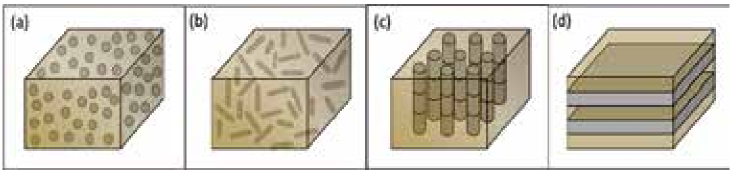

Figure 2. (a) ODS and/or ceramic particles reinforced composites, (b) whisker reinforced composites, (c) fiber reinforced composites and (d) laminated/3D composites.

3.1.1. Oxide-dispersion-strengthened (ODS) alloys

The dispersion of oxides increases the creep strength, which is an important property for high-temperature structural materials [27, 28]. Therefore, ODS W composites have caught the attention of researchers due to their improved high-temperature mechanical properties. Extensive research work is in progress to develop ODS-W composites with optimized high-temperature and plasma-facing properties. An important aspect of the R&D work to realize ODS W composites is to explore materials which may maintain a suitable microstructure after irradiation without grain growth or recrystallization [1].

Y_2O_3/W ODS composites have been investigated by many scientists [5]. When a Y_2O_3/W ODS composite was produced by powder metallurgy, it revealed lower brittleness between 400 and 1000°C, but a Charpy test at 500–1000°C revealed a reduced ability to absorb energy at 500–1000°C [19]. Itoh et al. and Kim et al. also investigated Y_2O_3/W ODS composites, finding enhanced densification in the Y_2O_3/W ODS composite due to the addition of yttria [10]. Grain refinement, which increases the strength of the material, was also observed from 18.8 to 3.7

μm, in ODS-W [23]. Liu et al. and Zhou et al. also reported improved mechanical properties and grain refinement due to the addition of 1wt% Y_2O_3 to W [5]. The grain refinement of Y_2O_3/W by adding Ti has also been reported [54].

The characteristics of Pr_2O_3/W composites were investigated by doping via a wet chemical method. Pr_2O_3 increased the tensile strength of the composite. The wet chemical method, which differs from conventional solid-state synthesis approaches such as mechanical alloying, produces a combined powder using liquid phases. The wet chemical method produces the powder with relatively fine grains and no residual stress [26].

Another important additive which has captured the attention of many researchers is La_2O_3 [55–58]. The addition of 1% La_2O_3 in W can enhance its machinability and recrystallization temperature [55]. 1wt%La_2O_3 W also shows refined grains and improved mechanical properties when prepared either by mechanical alloying (MA) and spark plasma sintering (SPS) or microwave sintering [5]. The behavior of La_2O_3-doped W has also been investigated by producing this composite via a hydrothermal-hydrogen reduction process [57].

Given the findings of research conducted thus far, ODS W composites are expected to show good high-temperature mechanical properties and resistance to irradiation [19]. Therefore, ODS W composites may serve in parts of fusion reactors, such as in a gas-cooled divertor, where pure W is joined with a La_2O_3/W composite [1].

3.1.2. Ceramic particle-reinforced composites

Like oxides, carbides are also drawing much attention as a candidate dopant to produce dispersion-strengthened W composites [5]. Many types of carbide are being investigated, including TiC, TaC [20], WC [23], ZrC [59] and SiC [11].

WC/W composites, when sintered at 1800°C after an addition of 5 and 10%vol WC, are converted into 8.9vol%W_2C/W and 17.8vol%W_2C/W by the $aW+bWC \rightarrow (a-b)W+bW_2C$ reaction. The material may retain a high-temperature W_2C phase if cooled at a high cooling rate (~150°C/min), but conventional sintering, in which the cooling rate is low, also resulted in W_2C, indicating that the decomposition of the W_2C phase may be challenging. Grain refinement and densification were observed as a result of an addition of WC [23].

The lower neutron activation of SiC [11] has granted the SiC/W composite a unique place among other high-temperature PFMs. SiC/W exhibits a good combination of thermal, mechanical and physical properties. SiC/W composites when fabricated by hot pressing or spark plasma sintering between 626 and 1926°C have reaction phases of WSi_2, WC, W_5Si_3 and W_2C [12]. These reaction phases can cause the material to fail; therefore, W-SiC requires additional attention [11]. The formation of reaction phases in W-SiC can be avoided with plasma spraying at a high temperature (5000–12,000°C) and at high velocities (200–700 m s^{-1}), as was done by Kang and Fahim, who prepared 50wt% and 12wt%SiC/W composites without reaction phases. The porosity of their composite was increased due to the oxidation of W and the decomposition of SiC [11]. The oxidation of tungsten along with structural imperfections have significant effects on the thermal and mechanical properties of W-SiC composites, as observed when a 12wt%W-SiC composite was prepared using a gas-tunnel-type plasma spray; the composite was fully dense and showed a gradual decrease in its hardness due to the formation of WO_3 [12].

2wt%TaC/W and 8wt%TaC/W samples were developed via powder injection molding. The powder mixtures, with a required proportion, were dried and mixed with a 50vol% polyolefine-based binder to produce feedstock for injection molding. The green compacts of W-TaC composites, produced by injection molding, were sintered in an H_2 atmosphere after removing the binder, the impurities and the residual stress by debinding. High agglomeration of TaC particles and brittleness in the resultant composites were observed [20]. In addition to powder injection molding, attempts to produce TaC/W composites with enhanced properties using SPS, hot rolling followed by annealing [60] and mechanical alloying with subsequent hot isostatic pressing have been used [61].

Due to its high melting point and comparable mechanical and thermal properties with W, ZrC is also a dopant of interest in the effort to develop a W-based composite having good high-temperature properties. In the search for a suitable W-based composite, 35vol%ZrC/W was produced by reaction sintering via the heating ZrO_2 and WC together up to a temperature of 2100°C with subsequent evaluation of physical and mechanical properties [62]. A sol–gel method followed by precipitation, drying, hydrogen reduction, and sintering was also utilized to develop more than 99% dense ZrC/W composites. The improvement in the high-temperature thermophysical and mechanical properties upon an addition of ZrC was also observed by producing 30vol%ZrC-W via hot pressing under a vacuum at 2000°C [63]. While fabricating ZrC/W, close control over the dimensions and process parameters is required to establish uniform effects of the process parameter on the feed materials. ZrC/W composites containing 20vol%ZrC and fabricated by hot pressing, when subjected to laboratory investigations, reveal ZrC_xO_y in addition to (Zr, W)C in the core of sample which resulted in inhomogeneous structure and properties [64].

Another important W-based composite, which can improve strength, microstructural stability, and irradiation resistance and can solve the embrittlement problem of W, is the TiC/W composite. The TiC/W composite, when prepared by the wet chemical method and spark plasma sintering at 1800°C, showed a relative density of 99.0% and improved thermal stability at elevated temperatures. The grains and grain boundaries both showed the presence of TiC particles, and the sample showed a mixture of inter- and transgranular fracturing [65]. In contrast, the 0.1wt%TiC/W composite produced by a different synthesis technique, i.e., wet chemical processing with polyvinylpyrrolidone (PVP) as a dispersion agent and SPS, showed the well-dispersed presence of TiC particles inside the grains only. The bending strength of the composite with PVP was 562.24 MPa, whereas without PVP it was 486.67 MPa [66]. Another approach to avoid the agglomeration of TiC particles and to obtain good phase stability, protection of the core from the environment, and good physical and chemical properties is the synthesis of core-shell structured TiC/W powders, by immersion of TiC in aqueous solution of hydrofluoric acid and ammonium fluoride followed by cleaning, deionizing, drying and then a reduction step [67]. The ongoing research to explore TiC/W composites has led to the production of 0–40%TiC/W composites via milling in ethanol, with the milled powder hot pressed at 20 MPa and 2000°C in a vacuum. The increasing amount of TiC increases the modulus of elasticity, hardness, and coefficient of thermal expansion of the TiC/W but decreases thermal conductivity. Indifferently, toughness and flexural strength increases with TiC up to 20% then again decreases [68]. The addition of 0.1wt%TiC to W produces a composite having a recrystallization temperature of 1500°C [69] but 0.1wt%TiC and 1.1wt%TiC/W don't affect deuterium retention capabilities of W [69, 70].

3.1.3. Fiber- or whisker-reinforced composites

Fibers play a very effective role in the enhancement of the mechanical properties of materials by transmitting and bearing loads while stretching. By absorbing energy, fibers prolong or deflect the paths of cracks as they propagate while also improving the strength and toughness of fiber-based composites [24]. By frictional sliding and debonding of the fiber/matrix interface, fibers control cracking and enhance the load-bearing capacity of composite materials. As fibers suppress cracks, a greater load is required to pull out the fibers, and when the load is increased further, the metal cracks propagate again, but in a controlled manner [27, 28]. In several industrial applications, the toughness of composites was significantly improved by the addition of fibers [27].

The effects of carbon fibers (C_f) on W were studied by adding 0.5wt% and 2wt% C_f with an average diameter of ~7–8 μm to W powders with a grain size of 1.2μm, with 1%TiC also added to the composite. All samples showed relative density levels exceeding 97%, and the density of the TiC/W with 0.5wt%C_f sample was 98.36% [24]. A mechanical load moves dislocations and concentrates stress, also rupturing TiC particles or dislocating/detaching TiC from W to nucleate. Micropores then grow, coalesce and fracture. However, these phenomena are rarely observed in TiC/W with 2wt%C_f composites [24].

W wires, which are ductile and usually have a tensile strength which exceeds 2.7 GPa, can be added to the W matrix to produce W_f/W composites. The W fibers can withstand a fusion environment until they lose their toughness and become brittle. The effectiveness of W_f with regard to the properties of W_f/W composites depend upon the volume fraction of the fibers [27]. Intermediate fracture energy of W_f/W interface is needed to obtain maximum toughness in fiber-reinforced composites. The interface should be able to debond such that it can deflect cracks, and it should be strong enough to absorb energy and transfer a load. Interface coating is suggested to achieve this requirement of the interface in a W_f/W composite [27, 28]. The effects of such interface coatings of carbon and ZrO_x-based materials on shear strength, debonding strength and fracture energy have already been studied [27, 28].

A Ta (fiber/powder)-W composite was also effectively developed by hot isostatic pressing. Pulse-plasma sintering can also be used, as it imparts a high density to a composite. Ta shows high affinity for O_2, and a Ta-Ta_2O_5 eutectic mixture forms in the composite [15].

W/Cu composites, which are typically developed by infiltration, can scarcely achieve full density owing to the differences in their thermal expansion coefficients and their poor solubility. In order to increase the density of W/Cu composites, high temperatures can be used to improve the wettability. A W_f-reinforced W/Cu composite was prepared for use as an intermediate layer between a CuCrZr heat sink and plasma-facing W in a fusion reactor [18].

3.1.4. Laminated or 3D composites

In addition to their other properties, plasma-facing materials require good toughness in order to be successfully utilized as structural materials in fusion plants. Cold working can shift the DBTT to a lower value; in an extreme case, it may be −120°C. W foils produced by cold working processes such as rolling and forging can exhibit fracture toughness levels of 70 MPa $m^{1/2}$ and can sustain 1000 bar of pressure during burst tests at room temperature [71]. Laminated W composites consisting of multiple layers of W foils can be used as a structural material, as they demonstrate ductile behavior because W foils are ductile at room temperature [72, 73]. The behavior of a W-foil laminated composite under a mechanical load revealed that this material has the potential to serve in fusion reactors as a structural material [73].

W laminates, which were produced by assembling several layers of W foils together, when subjected to Charpy impact test, absorbed 2 J, 5 J and 10 J of energy at room temperature, at 100°C, and at 300°C, respectively. The laminates, which were developed from the recrystallized foils at 1800°C for 1 hour, showed an increase in DBTT to 500°C as compared to a recrystallized W plate [74, 75].

The properties of W laminates depend upon the types of interlayers, the joining methods and materials, and the microstructure of the foil and interface. The brazing of foils with a silver-copper filler material does not affect the microstructure; this method can be used to develop a sharp interface between the foil and the filler. This type of laminate is best in terms of low-temperature toughness [72]. Copper is also used to join the interlayers of tungsten foils, but it slightly alters the microstructure and produces a sharp interface. Laminates that utilize Ti for brazing show large grains and a diffusion zone between the Ti and the W. Zr, if used for brazing, reacts with W excessively and produce small bands of W [72].

A laminated W composite was synthesized using ultrafine W foils. Diffusion bonding between the W laminates and the Ti interlayer was used. The changes in the mechanical properties during annealing at 1000°C for 10 to 1000 hours were examined, with the results demonstrating the inappropriateness of this material in structural applications at 1000°C [76].

Laminated W pipes find structural applications in fusion reactors, where they serve to carry He coolant and bear impingements. For this and other similar applications of laminated W, composites with low DBTTs are required [77]. Laminated composites with a copper foil interlayer were developed by rolling and brazing. As compared to pure W, the laminated W-Cu composite showed extraordinary behavior when subjected to impact and burst tests. In the burst tests, this material did not explode up to 1000 bar [77]. In addition to copper, palladium, titanium, zirconium, vanadium and other materials have also been used to create interlayers, and the choice of the interlayer material and the interface properties significantly affect the overall behavior of the resulting laminated composites [77].

In fusion reactors, W-based composites employed in a He-cooled divertor are joined to other structural materials. A W/Cu laminated composite can be joined to steel by brazing [77]. A laminated, functionally graded W/Cu composite with layers of a W/Cu composite materials with varying compositions was also investigated for its possible application in a plasma-facing environment [34].

In order to meet the requirements of high-temperature strength and reasonable ductility at low temperatures for plasma-facing applications, bonded layers of high-strength and high-ductility materials in the form of hybrid composites were analyzed. W/Cu and W/AgCu laminates were studied, and their low melting points and low strength levels diverted the attention of researchers towards V due to its sufficient high-temperature strength, good irradiation resistance, and much higher melting point, exceeding 1300°C. A hybrid W/V composite was produced by the diffusion bonding of thin layers of W and V at 700°C under a compressive stress of 97 MPa with a dwell time of 4 hours under a vacuum. A continuous increase in the hardness from the V (2 GPa) to the W side (8.5 GPa) was observed. The W/V hybrid composite also showed increased toughness. The layered structure of a hybrid composite was found to be highly resistant to crack propagation [78]. A W/V laminated composite with significant high-temperature creep resistance and good fracture toughness at low temperatures was produced. As compared to pure W and pure V, the laminated W/V composite shows a wide operating temperature window [79].

3.2. Fabrication methods of W-based composites

A number of techniques are used to fabricate W-based composites, such as (i) mechanical milling and alloying [26], (ii) conventional sintering [19], (iii) hot pressing (HP) and hot isostatic pressing (HIP) [21], (iv) spark plasma sintering (SPS) [26], (v) plasma pressure compaction (PPC) [23], (vi) microwave sintering [23], (vii) resistance sintering under ultrahigh pressure (RSUHP) [33], (viii) rolling [14], (ix) powder injection molding [20], (x) hot forging [19], (xi) combustion synthesis with centrifugal infiltration [18], (xii) polymer infiltration and pyrolysis (PIP) [11], and (xiii) a wet chemical process. The selection of any one technique depends on the type of composite, and it has great influence on the density, microstructure and other properties of the resultant composites [21].

Due to the sufficiently high melting point of W, mechanical milling is preferred for the fabrication of metallic W. It is a high-energy procedure which produces a uniform, homogeneous and controlled microstructure by repeated welding, fracturing and rewelding [80]. Ultrafine-grained (UFG) tungsten, which exhibits improved ductility, is also produced by mechanical milling [73].

To create nanosized ODS W powders, mechanical milling and mechanical alloying are commonly used [26]. Wang et al. found that the mechanical milling improved the sinterability of nano W powder when used prior to consolidation by pressureless sintering [23], HIP, and the SPS of PPS [15]. Improvements in the density as a result of milling have also been observed [15]. In addition to the advantages of mechanical milling and mechanical alloying, as noted earlier in this section, there are some disadvantages as well. During milling, dopant/additive particles tend to agglomerate due to high surface energy, and some contamination is also possible due to wear of the milling media and equipment. To avoid these detrimental effects of mechanical milling and alloying, milling is sometimes replaced by wet chemical processes, which develop composites with high purity and homogeneity levels [26]. After milling of the powder, conventional sintering (CS) is used to generate dense and refined microstructures in W-based composites [21, 26]. In the HP and SPS approaches, the samples are compressed during the sintering step. As a result, these techniques require a low sintering temperature and a short dwell time as compared to those used in CS. The short sintering time and optimum temperature help to prevent grain growth [21]. However, plasma/microwave sintering, as well as HIP, cannot be used for mass production because these techniques lack the ability to fabricate relatively large components [5].

SPS, being less time consuming and less prone to grain growth [15], and porosity [26], has numerous applications. In addition to particle-reinforced tungsten composites, fiber-reinforced composites such as TiC/W with (0.5–2)wt%C_f [24] and tantalum fiber/powder-nano-structured W composites can be consolidated by SPS [15].

Microwave sintering may also be used to sinter W-composites. Jain et al. utilized microwave sintering followed by HIP to sinter submicron W powder. After sintering, the density was 91.3%, which was raised to 98.5% after HIP [23].

Another technique, known as gas-tunnel-type plasma spraying (GTPS), has also been used to develop several W-based composites, such as W/SiC [12]. In order to fabricate functionally graded W/Cu composites, resistance sintering at ultrahigh pressure levels (RSUHP) has been utilized. The synthesis of laminated W/Cu composites having six layers of W/Cu with different volume ratios has been reported in studies which use RSUHP [33].

To produce bulk components of laminated W, rolling is used, as this process can result in a nano-structured microstructure as well [14]. The powder injection molding (PIM) process for joining W and materials doped with W was used to eliminate any further need for brazing or welding [20]. In order to produce small composite pellets, injection molding is used. Injection molding, which produces green pellets, is followed by debinding to remove impurities and residual stress [20].

A 2%Y_2O_3/W composite, when produced by pressing and then sintering at 2000°C followed by hot forging [4, 19], results in a relative density of 99.3% and a grain size of 1–2 μm. The pressing, sintering, and hot forging process were also utilized to produce pure W or 2%Y_2O_3/W composites. A composite with a density exceeding 99% was obtained because yttria particles strengthened the grain boundaries and reduced the porosity [22].

A novel method, termed combustion synthesis with centrifugal infiltration, has been proposed to produce W-fiber-reinforced W/Cu composites. In this combustion synthesis, Cu melt produced through a thermite reaction at 2000°C was infiltrated into W powder and a fiber bed by gravity. The high temperature causes the sintering of W particles and binds the W fibers [18].

Polymer infiltration and pyrolysis (PIP) is used to fabricate other important high-temperature plasma-facing candidate materials, e.g., W–Si–C. The pyrolysis of raw powders followed by infiltration and a heat treatment are carried out to obtain composite materials with W, W_2C, and W_5Si_3 phases. PIP is a low-temperature process which requires an additional heat treatment to promote densification and crystallinity [11].

The wet chemical process is utilized to produce composite powder of high purity and homogeneity levels [26]. The development of TiC/W ultrafine powder via chemical reduction has also been reported. In the chemical process, tungsten hexachloride serves as the raw material, ethyl alcohol as a solvent, lactic acid as a complexing agent, hydrazine hydrate as a reducing agent, 2,2-dipyridyl as a stabilizer, and ammonia water as a pH controller. The reduction process is carried out in an H_2 atmosphere to avoid oxidation; after the reduction step, SPS is carried out to produce a bulk composite [13]. The preparation of ODS-W composites by another wet chemical process, i.e., the reaction of a W precursor with praseodymium salt in water at room temperature, has also been reported [26]. This method produced highly homogeneous Pr_2O_3/W which was consolidated by SPS. The microstructure of the ODS-W composite showed dispersed oxide particles both in the interior of the ultrafine grains and at the grain boundaries [26].

In practical applications, composites are joined with other materials in high-temperature and plasma environments. Electron beam welding, diffusion welding and vacuum electron beam welding are commonly used joining techniques for W-based composites. The properties of the joint may not be as good as those of composite materials depending on the filler metals used or on the presence of pores and/or cracks [81].

A good number of techniques are available for the development of W-based composites, with more developments, customized and novel methods yet to be developed. Some advantages and disadvantages are associated with each technique. Each technique imparts characteristic effects on any particular W-based composite. In order to develop any one composite, multiple techniques can be used, such as powder metallurgy in conjunction with infiltration. In addition, plasma spray and cold spray techniques have been utilized to fabricate tungsten-based composites [81].

4. Performance of W-based composites in a fusion reactor environment

4.1. Mechanical behavior

Researchers are in search of W-composites which can withstand high-temperature and plasma environments without losing their mechanical integrity. This section summarizes the mechanical behavior of several W composites reported in various publications.

The DBTT of pure W lies between 120 and 250°C. Many approaches to reducing the DBTT in this case, such as alloying or/and doping, to produce W-based composites are being considered [14]. A reduction in the brittleness of W is observed by producing bulk materials with W laminates, brazed using copper brazing. This technique produces W composites with DBTTs of less than 500°C [14].

W-based composites produced by doping with La_2O_3 and TiC show brittle failure up to 350°C. This brittleness is sustained up to 500°C when Y_2O_3 and TaC are used as additives [20]. The addition of 1wt% TiC in the W matrix results in stronger materials, but no change in the DBTT is observed [20]. However, Kurishita et al. observed decreases in the DBTT by preparing 0.25–0.8wt%TiC/W via mechanical alloying and hot isostatic pressing [5].

The DBTT of 2% Y_2O_3/W is between 400 and 1000°C, better than certain other composites. In 2%Y/W produced by mechanical alloying in an Ar atmosphere and HIP, yttrium was transformed into yttria, and the resulting composites showed DBTTs between 1000 and 1200°C. The ductile behavior of 2% Y_2O_3/W at temperatures higher than 400°C is due to the plastic deformation of the grains [19].

W-yttria composites undergo a ductile-to-brittle transition between 500 and 600°C, as it absorbs more energy when the temperature is increased in this range. However, the low values of the absorbed energy result in poor ductility of this composite, even at an elevated temperature [19]. An analysis of 2% Y_2O_3/W composite samples after irradiation at 300 and 700°C reveals the formation of voids. The material showed improved stiffness, a reduction in its ductility, and improved mechanical properties [4].

An analysis of the fracture surface of 1wt%TiC/W revealed transgranular fractures in less porous areas and a highly dense composite material. Pure W fractures via the intergranular mode due to its weak grain boundaries, indicating that the addition of TiC strengthens the grain boundaries. The average grain size was 3 μm, lower than the grain size of pure W, which is 10 μm [13].

The powder metallurgical route was adopted to produce a 2% Y_2O_3/W composite. This material exhibited improved hardness up to 4.9 GPa, which is higher than that of pure W (i.e., 4.5 GPa [22]) produced by an identical method. It is important to note here that another researcher reported that the hardness of 2%Y_2O_3/W was identical to that of pure W, i.e., 4.78 GPa [4]. A separate publication reported an increase in the hardness of 2%Y_2O_3/W to 4.9 GPa when it was produced by the same method [22]. However, the hardness of a 2%Y_2O_3/W composite was found to be lower than those of 2%Y/W and 1%Y_2O_3/W when developed by mechanical alloying [19]. The improved density and grain-stabilizing ability of yttria allow this material to enhance the mechanical properties of materials [22]. The hardening capacity of a W-yttria composite depends on the temperature, as the storage of dislocations during permanent deformation decreases with an increase in the temperature. The hardening capacity of W-yttria decreases from 0.658 to 0.32 when the temperature increases from 673 to 1273 K [19]. A hardness test of irradiated samples of 2%Y_2O_3/W was performed; considering a depth of the irradiation damage of 3 μm, the load during the hardness test was kept low (from 1 to 2 N). The irradiation effect on the hardness of the samples at 300 and 700°C was identical [4].

In an effort to improve the hardness, other composites, such as WC/W, TiC/W, and Ta/W, were also produced and analyzed. The addition of WC in W produced a composite with an increased hardness level, and the hardness values follow the WC, i.e., the hardness increases with an increase in the WC content, due to the high hardness of WC [23]. The hardness of TiC/W (471 Hv), developed by chemical reduction, was also found to be greater than that of pure W [13]. Similar behavior was noted by Kurishita et al. when they prepared 0.25–0.8wt%TiC/W through mechanical alloying and HIP [5]. Pr_2O_3 also contributes to the production of W composites with improved hardness. 1wt% Pr_2O_3/W synthesized by a wet chemical process and SPS shows Hv equal to 377.2, higher than that of pure W [26]. A Cu layer was bound with Cu/W via a novel method consisting of combustion synthesis and infiltration. The hardness of the Cu/W and the Cu layer was 75 HRB and 21 HRB, respectively [81].

W-Si-C composites produced by pyrolysis at 1800°C exhibit a flexural strength level of approximately 400 MPa. When such a composite is heat-treated at 1700°C, the flexural strength is reduced to ~350 MPa. The hardness and indentation modulus of post-heat-treated W-Si-C were found to be 7.8 GPa and 250 GPa, respectively [11]. The fractural strength is a function of the porosity/density; thus, to develop high-strength W composites, researchers have focused on low porosity and high density [21].

Yttria particles produce W-based composites with improved high-temperature strength. The Young's modulus of 2%Y_2O_3/W was found to be 400 GPa, which is higher than those of pure W, 2%Y/W and 1%Y_2O_3/W [19, 4, 22]. Larger yttria particles and a low porosity level resulted in improved mechanical behavior [22]. However, the Young's modulus of a W-based composite was found to decrease when a composite with 1wt%TiC was prepared by chemical reduction [13]. The strength may also be improved by producing W composites with 1wt %Pr_2O_3 [26] and 0.25–0.8wt% TiC [5]. Moreover, W_f-reinforced Cu/W composites prepared via combustion synthesis followed by centrifugal infiltration show a 12.7% improvement in the bending strength due the well-bonded W, Cu powder and W fibers [18].

The conventional sintering of W-based composites containing V, Ti, Nb, Ta, Fe, and Ni caused hydrogen embrittlement because the dissolution of H_2 dissolves into the composite due to the negative formation energy of the vacancy-hydrogen complexes. Hence, conventional sintering in a hydrogen environment is not recommended [21].

4.2. Thermal properties

Fine-grained W-based composites produced by doping with rare-earth oxides such as Y_2O_3 and La_2O_3 and carbides such as TiC and ZrC were subjected to transient heat flux tests. It was observed that a high heat flux of 200 MW/m^2 can be sustained by these materials, which is nearly 100% higher than conventionally sintered pure W. This promising behavior may be the result of the processing route, i.e., a sol–gel method, heterogeneous precipitation, spray drying, hydrogen reduction and ordinary sintering in sequence [5].

However, oxide- and carbide-doped W composite samples, when subjected to a thermal shock, showed cracks. However, pure W sintered at 2400°C withstands thermal shocks well [20].

The responses of W composites consisting of 20%-80% porous W and infiltrated by Cu, Al or Si and then exposed to a high-temperature environment have been thoroughly studied. These composites exhibit good strength, conductivity and good melt layer stability at high temperatures. In contrast with pure W, some W-based composites can withstand plasma edge temperatures in excess of 200 eV [82].

The thermal conductivity of TiC/W composites and pure W produced by chemical reduction followed by SPS at 1800°C decreases when the temperature is increased from ambient to 827°C. However, the conductivity remains above 120 W/m-K at RT [13]. The effect of the temperature on the thermal conductivity of ODS-W composites prepared by adding 1wt% Pr_2O_3 was examined, and the behavior of pure W was compared with that of pure W. The conductivity of both materials decreased when the temperature was increased from 25 to 800°C, but the conductivity of these materials exceeds 150 W/m-K at room temperature [26].

4.3. Oxidation resistance

In fusion reactors, W-based materials will be exposed to high-temperature and plasma environments; therefore, their high-temperature oxidation resistance is of great concern in the case of loss of vacuum accident. Attempts to develop W-based composites with enhanced high-temperature oxidative ablation resistance have been made by incorporating ZrN_p into a W matrix. 10–30% ZrN_p/W samples, when tested using an oxyacetylene torch, showed enhanced oxidative ablation resistance. The rate of ablation was found to decrease with an increase in the ZrN_p content. The microstructure of the ablated samples lacked a uniform protective film due to the insufficient amount of ZrN_p [83]. Improved oxidative ablation resistance and a reduction in the ablation rate were also found by adding HfC to W up to 30%. A protective layer of HfO_2 was found on post-ablated samples [84].

An analysis of the ablation properties of W-based composites suggests that composites with high oxidative ablation resistance can be developed by the incorporation of a W matrix with secondary phase particles having low thermal conductivity, a high melting point, and good oxidation resistance [84].

4.4. Behavior of composites in radiation and plasma environments

Pure W also faces transmutation damage, and in DEMO full-power operations, W may be transformed into W-3.8at%Re-1.4at%Os. These chemical variations alter the mechanical properties of pure W [14]. At the end of the lifetime of the blanket, 5–8 at% of W may be transmuted; moreover, transmutation below 1% has no significant effect on the physical properties of W alloys [2]. The transmutation of W is mainly a function of the neutron's spectrum and fluence [2]. Neutrons in a fusion environment may be absorbed by W with a consequent release of alpha and beta particles and the production of impurities such as Re, Ta, and Os. The change in the chemistry of the material degrades its mechanical (and other) properties [2].

ODS-W composites when prepared by adding Y_2O_3 also show irradiation hardening when subjected to 24 and 2 MeV Fe and He ions, respectively, up to a damage level of 5 dpa at 300 and 700°C. Irradiation resulted in radiation loops in W and voids in Y_2O_3 particles, which caused the hardness to increase [4]. No voids or cracking were found on the grain boundaries, demonstrating the capability of the grain boundaries of Y_2O_3/W composites to accommodate heavy ions [4]. In another study in which a W-yttria composite produced by a powder metallurgical method was subjected to 24 and 2 MeV Fe and He ions, similar changes in the microstructure and hardness were observed [22].

An improvement in the ion irradiation damage resistance of W by doping with TiC was observed by Kurishita et al. In their study, mechanical alloying and HIP were used to produce 0.25–0.8wt%TiC/W composites. He ions at 500°C were used to irradiate TiC/W. The irradiation vacancy defect density was only 1/3 to 1/4 of the density of commercially pure W [5].

The interaction between plasma-facing materials, such as W and its composites, and a single hydrogen beam, a single helium beam and an electron beam results in a rough surface and a fine scale. This modification of the surface can affect the mechanical properties along with the thermal conductivity and tritium retention capabilities of the material [22]. The sputtering threshold energy may be increased from 2.5 KeV to more than 10 KeV by applying an alkali monolayer onto a W composite surface. Alkali metals having a higher mass are more useful for reducing sputter-induced erosion [82].

4.5. Hydrogen retention

The addition of 0.1wt%TiC to W does not cause significant differences in the deuterium retention behavior [69]. The deuterium retention behavior of a 1.1wt.%TiC/W composite was also investigated by exposing 1.1%TiC/W composite samples to D_2 gas at 527–690°C and 100 kPa or by irradiating the 1.1%TiC/W composite via 38 eV/D ions at 527°C. Thermal desorption spectroscopy revealed slightly higher deuterium retention in 1.1%TiC/W as compared to pure W after exposure to D_2 gas. However, it was significantly higher after D ion irradiation [61]. The deuterium retention properties of TiC/W when examined by irradiating TiC/W composite samples with 200 eV/D ions at fluence levels ranging from 1×10^{22} to 1×10^{24} D/m^2 at a temperature of 37°C or with 38 eV/D ions at fluence levels ranging from 6×10^{22} to 6×10^{24} D/m^2 at temperatures of 27 and 327°C were examined. At 37 and 27°C, no significant differences in the deuterium retention of TiC/W and pure W were observed. However, at 327°C, deuterium retention was higher in TiC/W than in pure W [70].

5. Conclusion

In order to understand the feasibility of W-based composites for nuclear fusion applications, the fabrication processes, properties and performances of W-based composites in the forms of oxide dispersion strengthened alloys, ceramic particle reinforced composites, fiber- or whisker-reinforced composites, and laminated 3D composites were reviewed. Many advantages in mechanical properties, oxidation resistances, and radiation resistances were identified while more attention should be given to enhancing further thermal properties and hydrogen retention resistance. To address the materials challenges in the development of plasma-facing materials like first wall or divertor in fusion reactors, the selection of the reinforcement phase and the structures of W-based composites should be optimized through the wide range of performance evaluation calculations and experiments.

Author details

Owais A. Waseem and Ho Jin Ryu*

*Address all correspondence to: hojinryu@kaist.ac.kr

Department of Nuclear and Quantum Engineering, Korea Advanced Institute of Science and Technology, Daejeon, Republic of Korea

References

[1] Bolt H, Barabash V, Krauss W, Linke J, Neu R, Suzuki S, et al. Materials for the plasma-facing components of fusion reactors. J Nucl Mater. 2004; 329-333:66–73. DOI:10.1016/j.jnucmat.2004.04.005

[2] Desecures M, El-Guebaly L, Druyts F, Van Iseghem P, Massaut V, Van Oost G. Study of radioactive inventory generated from W-based components in ITER and PPCS fusion designs. Fusion Eng Des. 2013; 88(9–10):2674–8. DOI: 10.1016/j.fusengdes.2013.02.042

[3] Anderl R A, Pawelko RJ, Hankins MR, Longhurst GR, Neiser R a. Hydrogen permeation properties of plasma-sprayed tungsten. J Nucl Mater. 1994; 212-215:1416–20. DOI: 10.1016/0022-3115(94)91061-8

[4] Battabyal M, Spätig P, Baluc N. Effect of ion-irradiation on the microstructure and microhardness of the W-2Y_2O_3 composite materials fabricated by sintering and hot forging. Fusion Eng Des. 2013; 88(9–10):1668–72. DOI: 10.1016/j.fusengdes.2013.03.060

[5] Fan J, Han Y, Li P, Sun Z, Zhou Q. Micro/nano composited tungsten material and its high thermal loading behavior. J Nucl Mater. 2014; 455(1–3):717–23. DOI: 10.1016/j.jnucmat.2014.09.037

[6] Zhang J, Luo L-M, Zhu X-Y, Chen H-Y, Chen J-L, Zan X, et al. Effect of doped Lu_2O_3 on the microstructures and properties of tungsten alloy prepared by spark plasma sintering. J Nucl Mater. 2015; 456:316–20. DOI: 10.1016/j.jnucmat.2014.09.068

[7] Zakharov A, Begrambekova S, Grunin a. Plasma Influence on Tungsten Powder. Phys Procedia. 2015; 71(February):99–104. DOI: 10.1016/j.phpro.2015.08.321

[8] Alves LC, Alves E, Barradas NP, Dias M, Mateus R, Carvalho P, et al. Surface composition and morphology changes of JET tiles under plasma interactions. Fusion Eng Des. 2011; 86(9–11):2557–60. DOI: 10.1016/j.fusengdes.2011.03.093

[9] Causey R a. Hydrogen isotope retention and recycling in fusion reactor plasma-facing components. J Nucl Mater. 2002; 300(2–3):91–117. DOI: 10.1016/S0022-3115(01)00732-2

[10] Armstrong DEJ, Yi X, Marquis E A, Roberts SG. Hardening of self ion implanted tungsten and tungsten 5-wt% rhenium. J Nucl Mater. 2013; 432(1–3):428–36. DOI: 10.1016/j.jnucmat.2012.07.044

[11] Ivekovič A, Galatanu A, Novak S. Low-activation W–Si–C composites for fusion application. Fusion Eng Des. 2015; 100:638–45. DOI: 10.1016/j.fusengdes.2015.08.013

[12] Fahim NF. Thermal conductivity of plasma-sprayed W/SiC composite for high-temperature energy applications. Surf Coatings Technol. 2008; 202(9):1696–703. DOI: 10.1016/j.surfcoat.2007.07.027

[13] Ding X-Y, Luo L-M, Chen H-Y, Luo G-N, Zhu X-Y, Zan X, et al. Fabrication of W–1wt. % TiC composites by spark plasma sintering. Fusion Eng Des. 2015; 92:29–34. DOI: 10.1016/j.fusengdes.2015.01.003

[14] Armstrong DEJ, Britton TB. Effect of dislocation density on improved radiation hardening resistance of nano-structured tungsten–rhenium. Mater Sci Eng A. 2014; 611:388–93. DOI: 10.1016/j.msea.2014.06.013

[15] Dias M, Guerreiro F, Correia JB, Galatanu A, Rosiński M, Monge M A, et al. Consolidation of W–Ta composites: Hot isostatic pressing and spark and pulse plasma sintering. Fusion Eng Des. 2015; 99:1950–5. DOI: 10.1016/j.fusengdes.2015.06.178

[16] Li M, Werner E, You J-H. Influence of heat flux loading patterns on the surface cracking features of tungsten armor under ELM-like thermal shocks. J Nucl Mater. 2015; 457:256–65. DOI: 10.1016/j.jnucmat.2014.11.026

[17] Raffray AR, Nygren R, Whyte DG, Abdel-Khalik S, Doerner R, Escourbiac F, et al. High heat flux components-Readiness to proceed from near term fusion systems to power plants. Fusion Eng Des. 2010; 85(1):93–108. DOI: 10.1016/j.fusengdes.2009.08.002

[18] He G, Xu K, Guo S, Qian X, Yang Z, Liu G, et al. Preparation of tungsten fiber reinforced-tungsten/copper composite for plasma facing component. J Nucl Mater. 2014; 455(1–3): 225–8. DOI: 10.1016/j.jnucmat.2014.05.026

[19] Battabyal M, Schäublin R, Spätig P, Walter M, Rieth M, Baluc N. Microstructure and mechanical properties of a W–2wt.%Y_2O_3 composite produced by sintering and hot forging. J Nucl Mater. 2013; 442(1–3):S225–8. DOI: 10.1016/j.jnucmat.2013.01.301

[20] Antusch S, Armstrong DEJ, Britton T Ben, Commin L, Gibson JSK-L, Greuner H, et al. Mechanical and microstructural investigations of tungsten and doped tungsten materials produced via powder injection molding. Nucl Mater Energy. 2015; 3-4:22–31. DOI: 10.1016/j.nme.2015.04.002

[21] Arshad K, Wang J, Yuan Y, Zhang Y, Zhou Z-J, Lu G-H. Development of tungsten-based materials by different sintering techniques. Int J Refract Met Hard Mater. 2015; 50:253–7. DOI: 10.1016/j.ijrmhm.2015.02.004

[22] Battabyal M, Spätig P, Murty BS, Baluc N. Investigation of microstructure and micro-hardness of pure W and W-2Y2O3 materials before and after ion-irradiation. Int J Refract Met Hard Mater. 2014; 46:168–72. DOI: 10.1016/j.ijrmhm.2014.06.004

[23] Chanthapan S, Kulkarni a, Singh J, Haines C, Kapoor D. Sintering of tungsten powder with and without tungsten carbide additive by field assisted sintering technology. Int J Refract Met Hard Mater. 2012; 31:114–20. DOI: 10.1016/j.ijrmhm.2011.09.014

[24] Chen H, Luo L, Tan X, Luo G, Li P, Zan X, et al. Microstructure and properties of W-TiC/Cf composites prepared by spark plasma sintering. Recent Adv Struct Integr Anal - Proc Int Congr. 2014; 463–6. DOI: 10.1533/9780081002254.463

[25] Dias M, Mateus R, Catarino N, Franco N, Nunes D, Correia JB, et al. Synergistic helium and deuterium blistering in tungsten–tantalum composites. J Nucl Mater. 2013; 442(1–3):69–74. DOI: 10.1016/j.jnucmat.2013.08.010

[26] Ding X-Y, Luo L-M, Lu Z-L, Luo G-N, Zhu X-Y, Cheng J-G, et al. Chemically produced tungsten–praseodymium oxide composite sintered by spark plasma sintering. J Nucl Mater. 2014; 454(1–3):200–6. DOI: 10.1016/j.jnucmat.2014.07.048

[27] Du J, Höschen T, Rasinski M, Wurster S, Grosinger W, You JH. Feasibility study of a tungsten wire-reinforced tungsten matrix composite with ZrOx interfacial coatings. Compos Sci Technol. 2010; 70:1482–9. DOI: 10.1016/j.compscitech.2010.04.028

[28] Du J, Höschen T, Rasinski M, You J-H. Shear debonding behavior of a carbon-coated interface in a tungsten fiber-reinforced tungsten matrix composite. J Nucl Mater. 2011; 417(1–3):472–6. DOI: 10.1016/j.jnucmat.2010.12.254

[29] Kalinin GM. High-Z plasma-facing and related materials. 1995; 181(1991):1193–8.

[30] Sakoi Y, Miyamoto M, Ono K, Sakamoto M. Helium irradiation effects on deuterium retention in tungsten. J Nucl Mater. 2013; 442(1–3):S715–8. DOI:10.1016/j.jnucmat.2012.10.003

[31] Mateus R, Dias M, Lopes J, Rocha J, Catarino N, Franco N, et al. Effects of helium and deuterium irradiation on SPS sintered W–Ta composites at different temperatures. J Nucl Mater. 2013; 442(1–3):S251–5. DOI: 10.1016/j.jnucmat.2013.02.068

[32] Nishijima D, Sugimoto T, Iwakiri H, Ye MY, Ohno N, Yoshida N, et al. Characteristic changes of deuterium retention on tungsten surfaces due to low-energy helium plasma pre-exposure. J Nucl Mater. 2005; 337-339:927–31. DOI: 10.1016/j.jnucmat.2004.10.011

[33] Ge CC, Zhou ZJ, Song SX, Du J, Zhong ZH. Progress of research on plasma facing materials in University of Science and Technology Beijing. J Nucl Mater. 2007; 363–365(1–3):1211–5. DOI: 10.1016/j.jnucmat.2007.01.173

[34] Mateus R, Dias M, Lopes J, Rocha J, Catarino N, Duarte P, et al. Blistering of W–Ta composites at different irradiation energies. J Nucl Mater. 2013; 438:S1032–5. DOI: 10.1016/j.jnucmat.2013.01.225

[35] Ivanov EY, Suryanarayana C, Bryskin BD. Synthesis of a nanocrystalline W-25 wt.% Re alloy by mechanical alloying. Mater Sci Eng A. 1998; 251(1–2):255–61. DOI: 10.1016/S0921-5093(98)00620-0

[36] Ohser-Wiedemann R, Martin U, Müller A, Schreiber G. Spark plasma sintering of Mo–W powders prepared by mechanical alloying. J Alloys Compd. 2013; 560:27–32. DOI: doi:10.1016/j.jallcom.2013.01.142

[37] Arshad K, Zhao M-Y, Yuan Y, Zhang Y, Zhao Z-H, Wang B, et al. Effects of vanadium concentration on the densification, microstructures and mechanical properties of

tungsten vanadium alloys. J Nucl Mater. 2014; 455(1–3):96–100. DOI: 10.1016/j.jnucmat.2014.04.019

[38] Chen C-L, Zeng Y. Synthesis and characteristics of W-Ti alloy dispersed with Y2Ti2O7 oxides. Int J Refract Met Hard Mater. 2015; 56:104–109. DOI: 10.1016/j.ijrmhm.2015.12.008

[39] Zhang Y, Ganeev A V, Wang JT, Liu JQ, Alexandrov I V. Observations on the ductile-to-brittle transition in ultrafine-grained tungsten of commercial purity. Mater Sci Eng A. 2009; 503(1–2):37–40. DOI: 10.1016/j.msea.2008.07.074

[40] Son S, Park K, Katoh Y, Kohyama A. Interfacial reactions and mechanical properties of W–SiC in-situ joints for plasma facing components. J Nucl Mater. 2004; 329–333:1549–52. DOI: 10.1016/j.jnucmat.2004.04.285

[41] Kim Y, Lee KH, Kim E-P, Cheong D-I, Hong SH. Fabrication of high temperature oxides dispersion strengthened tungsten composites by spark plasma sintering process. Int J Refract Met Hard Mater. 2009; 27(5):842–6. DOI: 10.1016/j.ijrmhm.2009.03.003

[42] Kumar S, Kumar A, Sampath K, Bhanu Prasad V V, Chaudhary JC, Gupta AK, et al. Fabrication and erosion studies of C–SiC composite Jet Vanes in solid rocket motor exhaust. J Eur Ceram Soc. 2011; 31(13):2425–31. DOI: 10.1016/j.jeurceramsoc.2011.06.007

[43] Kang HK. Microstructures of high volume SiC reinforced tungsten composites produced by plasma spray. Scr Mater. 2004; 51(11):1051–5. DOI: 10.1016/j.scriptamat.2004.08.008

[44] Baud L, Jaussaud C, Madar R, Bernard C, Chen JS, Nicolet MA. Interfacial reactions of W thin film on single-crystal (001) β-SiC. Mater Sci Eng B. 1995; 29(1–3):126–30. DOI: 10.1016/0921-5107(94)04017-X

[45] Khripunov BI, Koidan VS, Ryazanov AI, Gureev VM, Kornienko S. N, Latushkin ST, et al. Study of tungsten as a plasma-facing material for a fusion reactor. Phys Procedia. 2015; 71(February):63–7. DOI: 10.1016/j.phpro.2015.08.313

[46] German RM, Bose A, Mani SS. Sintering time and atmosphere influences on the microstructure and mechanical properties of tungsten heavy alloys. Metall Trans A. 1992; 23(1):211–9. DOI: 10.1007/BF02660866

[47] López-Ruiz P, Koch F, Ordás N, Lindig S, García-Rosales C. Manufacturing of self-passivating W-Cr-Si alloys by mechanical alloying and HIP. Fusion Eng Des. 2011; 86(9–11):1719–23. DOI: 10.1016/j.fusengdes.2011.03.107

[48] Steel HFT. Microstructure and mechanical properties of WC-SiC composites. J Iron Steel Res Int. 2011; 18(12):45–8,64. DOI: 10.1016/S1006-706X(12)60008-9

[49] Seng WF, Barnes PA. Calculations of tungsten silicide and carbide formation on SiC using the Gibbs free energy. Mater Sci Eng B. 2000; 72:13–8. DOI: 10.1016/S0921-5107(00)00457-8

[50] Hashemi M, Mirdamadi S, Rezaie HR. Effect of SiC nanoparticles on microstructure and wear behavior of Cu-Ni-W nanocrystalline coating. Electrochim Acta. 2014; 138:224–31. DOI: 10.1016/j.electacta.2014.06.084

[51] Park DY, Oh YJ, Kwon YS, Lim ST, Park SJ. Development of non-eroding rocket nozzle throat for ultra-high temperature environment. Int J Refract Met Hard Mater. 2014; 42:205–14. DOI: 10.1016/j.ijrmhm.2013.09.007

[52] Day AP. Powder Metal. National Physical Laboratory,Teddington, Middlesex, UK. 1998.

[53] Snead LL, Nozawa T, Katoh Y, Byun T-S, Kondo S, Petti DA. Handbook of SiC properties for fuel performance modeling. J Nucl Mater. 2007; 371(1–3):329–77. DOI: 10.1016/j.jnucmat.2007.05.016

[54] Zhou Z, Tan J, Qu D, Pintsuk G, Rödig M, Linke J. Basic characterization of oxide dispersion strengthened fine-grained tungsten based materials fabricated by mechanical alloying and spark plasma sintering. J Nucl Mater. 2012; 431(1–3):202–5. DOI: 10.1016/j.jnucmat.2011.11.039

[55] Shen Y, Xu Z, Cui K, Yu J. Microstructure of a commercial W-1% La2O3 alloy. J Nucl Mater. 2014; 455(1–3):234–41. DOI: 10.1016/j.jnucmat.2014.06.004

[56] Xu L, Yan Q, Xia M, Zhu L. Preparation of La2O3 doped ultra-fine W powders by hydrothermal-hydrogen reduction process. Int J Refract Met Hard Mater. 2013; 36:238–42. DOI: 10.1016/j.ijrmhm.2012.09.005

[57] Yan QZ, Zhang XF, Zhou ZJ, Shen WP, Zhang YC, Wang SM, et al. Status of R&D on plasma facing materials in China. J Nucl Mater. 2013; 442(1–3 SUPPL.1):S190–7. DOI: 10.1016/j.jnucmat.2012.11.046

[58] Guseva MI, Vasiliev VI, Gureev VM, Danelyan LS, Khirpunov BI, Korshunov SN, et al. Peculiarity of deuterium ions interaction with tungsten surface in the condition imitating combination of normal operation with plasma disruption in ITER. J Nucl Mater. 2001; 290-293:1069–73. DOI: 10.1016/S0022-3115(00)00471-2

[59] Yaghobizadeh O, Baharvandi H, Alizadeh A. Investigation of effect of acrylate gel maker parameters on properties of WC preforms for the production of W–ZrC composite. Int J Refract Met Hard Mater. 2014; 45:130–6. DOI: 10.1016/j.ijrmhm.2014.04.007

[60] Miao S, Xie ZM, Yang XD, Liu R, Gao R, Zhang T, et al. Effect of hot rolling and annealing on the mechanical properties and thermal conductivity of W-0.5wt.% TaC alloys. Int J Refract Met Hard Mater. 2016; 56:8–17. DOI: 10.1016/j.ijrmhm.2015.12.004

[61] Zibrov M, Mayer M, Gao L, Elgeti S, Kurishita H, Gasparyan Y, et al. Deuterium retention in TiC and TaC doped tungsten at high temperatures. J Nucl Mater. 2015; 463:1045–8. DOI: 10.1016/j.jnucmat.2014.11.112

[62] Zhang SC, Hilmas GE, Fahrenholtz WG. Zirconium carbide-tungsten cermets prepared by in situ reaction sintering. J Am Ceram Soc. 2007; 90(6):1930–3. DOI: 10.1111/j.1551-2916.2007.01642.x

[63] Song G-M, Wang Y-J, Zhou Y. The mechanical and thermophysical properties of ZrC/W composites at elevated temperature. Mater Sci Eng A. 2002; 334(1–2):223–32. DOI: 10.1016/S0921-5093(01)01802-0

[64] Zhang TQ, Wang YJ, Zhou Y, Song GM. Effect of temperature gradient in the disk during sintering on microstructure and mechanical properties of ZrCp/W composite. Int J Refract Metals Hard Mater. 2009;27(1):126–9. DOI: 10.1016/j.ijrmhm.2008.05.005

[65] Luo L-M, Tan X-Y, Chen H-Y, Luo G-N, Zhu X-Y, Cheng J-G, et al. Preparation and characteristics of W–1wt.% TiC alloy via a novel chemical method and spark plasma sintering. Powder Technol. 2015; 273:8–12. DOI: 10.1016/j.powtec.2014.12.033

[66] Lang S, Yan Q, Wang Y, Zhang X, Sun N, Deng L, et al. Preparation and microstructure characterization of W-0.1wt.%TiC alloy via chemical method. Int J Refract Met Hard Mater. 2015; DOI: 10.1016/j.ijrmhm.2015.11.005

[67] Ding X-Y, Luo L-M, Huang L-M, Luo G-N, Zhu X-Y, Cheng J-G, et al. Preparation of TiC/W core–shell structured powders by one-step activation and chemical reduction process. J Alloys Compd. 2015; 619:704–8. DOI: 10.1016/j.jallcom.2014.08.242

[68] Song G-M, Wang Y-J, Zhou Y. Thermomechanical properties of TiC particle-reinforced tungsten composites for high temperature applications. Int J Refract Met Hard Mater. 2003; 21(1–2):1–12. DOI: 10.1016/S0263-4368(02)00105-1

[69] Liu X, Chen J, Lian Y, Wu J, Xu Z, Zhang N, et al. Vacuum hot-pressed beryllium and TiC dispersion strengthened tungsten alloy developments for ITER and future fusion reactors. J Nucl Mater. 2013; 442(1–3):S309–12. DOI: 10.1016/j.jnucmat.2013.04.088

[70] Zibrov M, Mayer M, Markina E, Sugiyama K, Betzenbichler M, Kurishita H, et al. Deuterium retention in TiC and TaC doped tungsten under low-energy ion irradiation. Phys Scr. 2014; T159:014050. DOI: 10.1016/j.jnucmat.2014.11.112

[71] Reiser J, Rieth M, Möslang A, Greuner H, Armstrong DEJ, Denk T, et al. Tungsten (W) laminate pipes for innovative high temperature energy conversion systems. Adv Eng Mater. 2014; n/a – n/a. DOI: 10.1002/adem.201400204

[72] Reiser J, Rieth M, Möslang A, Dafferner B, Hoffmann J, Mrotzek T, et al. Tungsten foil laminate for structural divertor applications - Joining of tungsten foils. J Nucl Mater. 2013; 436(1–3):47–55. DOI: 10.1016/j.jnucmat.2013.01.295

[73] Reiser J, Rieth M, Möslang A, Dafferner B, Hoffmann J, Mrotzek T, et al. Tungsten foil laminate for structural divertor applications—Joining of tungsten foils. J Nucl Mater. 2013; 436(1–3):47–55. DOI: 10.1016/j.jnucmat.2013.01.295

[74] Reiser J, Rieth M, Dafferner B. Tungsten foil laminate for structural divertor applications—Basics and outlook. J Nucl Mater. 2012; 423(1–3):1–8. DOI: 10.1016/j.jnucmat.2012.01.010

[75] Wurster S, Baluc N, Battabyal M, Crosby T, Du J, García-Rosales C, et al. Recent progress in R&D on tungsten alloys for divertor structural and plasma facing materials. J Nucl Mater. 2013; 442(1–3 SUPPL.1):181–9. DOI: 10.1016/j.jnucmat.2013.02.074

[76] Reiser J, Franke P, Weingärtner T, Hoffmann J, Hoffmann A, Rieth M. Tungsten laminates made of ultrafine-grained (UFG) tungsten foil—Ageing of tungsten–titanium (W–Ti) laminates. Int J Refract Met Hard Mater. 2015; 51:264–74. DOI: 10.1016/j.ijrmhm.2015.04.032

[77] Bott R. Nuclear fusion programme, Annual report of the association of Karlsruhe Institute of Technology/EURATOM, Karlsruhe Institute of Technology (KIT) Scientific Publishing, Karlsruhe, Germany. 2014; (1):1–5.

[78] Basuki WW, Norajitra P, Spatafora L, Aktaa J. Fabrication of tungsten-vanadium hybrid material with sufficient toughness for high-temperature applications by diffusion bonding. 2014. DOI: 10.1007/s13398-014-0173-7.2

[79] Hohe J, Gumbsch P. On the potential of tungsten-vanadium composites for high temperature application with wide-range thermal operation window. J Nucl Mater. 2010; 400(3):218–31. DOI: 10.1016/j.jnucmat.2010.03.007

[80] El-Eskandarany MS. The history and necessity of mechanical alloying. Mechanical Alloying. Elsevier Inc.; Norwich, NewYork. 2015, 13–47 p. DOI: 10.1016/B978-1-4557-7752-5.00002-4

[81] He G, Zhao P, Guo S, Chen Y, Liu G, Li J. In suit synthesis and bonding of Cu to W–Cu composite by combustion synthesis and centrifugal infiltration. J Alloys Compd. 2013; 579:71–4. DOI: 10.1016/j.jallcom.2013.04.210

[82] Dewald AB, Brooks JN, Krauss AR, Gruen DM. A sputtering / redeposition analysis of alkali-based composites for limiter / divertor applications. 1987; 147:373–4.

[83] Umer MA, Lee D, Ryu HJ, Hong SH. High temperature ablation resistance of ZrNp reinforced W matrix composites. Int J Refract Met Hard Mater. 2014; 42:17–22. DOI: 10.1016/j.ijrmhm.2013.10.001

[84] Lee D, Umer MA, Ryu HJ, Hong SH. Elevated temperature ablation resistance of HfC particle-reinforced tungsten composites. Int J Refract Met Hard Mater. 2014;43:89–93. DOI: 10.1016/j.ijrmhm.2013.11.009

Edited by Rehab O. Abdel Rahman
and Hosam El-Din Mostafa Saleh

Assessing and improving nuclear material performance is a crucial subject for the sustainability of the nuclear energy and radioactive isotope supplies. This book aims to present research efforts used to identify nuclear materials performances in different areas. The contributions of esteemed international experts have covered important research aspects in fission and fusion technologies and naturally occurring radioactive materials management. The authors introduced current and anticipated trends toward better performances and mitigating challenges for commercial application of innovative technologies, biological remediation of mine effluents, nuclear fuel performance in power and research fission reactors, gamma ray spectrometer calibration, and recent advances in understanding the performance of tungsten composite in fusion reactor environment.

ISBN 978-953-51-6658-0
9 789535 166580

Photo by 3dalia / CanStock

IntechOpen